ATTRIBUTION OF SNOW MELT ONSET AND LINKAGES ACROSS THE NORTHERN HEMISPHERE CRYOSPHERE

By

JOHN MIODUSZEWSKI

A dissertation submitted to the

Graduate School-New Brunswick

Rutgers, The State University of New Jersey

In partial fulfillment of the requirements

For the degree of

Doctor of Philosophy

Graduate Program in Geography

Written under the direction of

Dr. David A. Robinson

And approved by

_____

_____

_____

_____

New Brunswick, New Jersey
May, 2015

ABSTRACT OF THE DISSERTATION

Attribution of snow melt onset and its linkages with variability in the Arctic cryosphere

by JOHN MIODUSZEWSKI

Dissertation Director:

Dr. David A. Robinson

In the region of Earth most sensitive to climate change, spring snowmelt serves as a measurable indicator of climate change and plays a strong role in the feedbacks that amplify Arctic warming. These feedbacks are strongest over sea ice and the Greenland ice sheet (GrIS) as these surfaces continue to melt through the summer and potentially impact one another. The first component of this study characterizes the snow melt season and attributes melt onset both at a hemispheric scale and regionally in northern Canada. Analysis is then expanded to the melt onset date (MOD) on sea ice and the GrIS where

covariability is addressed extending into the summer melt season. MOD and sea ice concentration (SIC) data are obtained from passive microwave satellite datasets, while NASA's Modern-Era Retrospective Analysis for Research and Applications (MERRA) provides energy balance and meteorological fields with primarily meltwater production used as output from a regional climate model (Modèle Atmosphérique Régional, MAR) for the period 1979 - 2013.

Across much of the Northern Hemisphere, energy advection plays a larger role in melt onset in regions where snow begins melting in March and April, while shortwave fluxes have a greater influence where the MOD occurs in May and June. As the MOD arrives earlier, this implies that there is a potential shift in snow melt drivers toward those involved in advective processes. Comparable results are found in the regional study, where melt is controlled more by advective energy where melt onset begins sooner, compared to higher levels of radiative energy further north. Analysis of the remainder of the Arctic finds strong covariability among Greenland meltwater production, 500 hPa geopotential heights, and SIC, particularly in Baffin Bay, Fram Strait, and Beaufort Sea early in the summer. Most of this covariance is likely due to simultaneous influence of the atmospheric circulation anomalies, though there may be a local influence from Baffin Bay to the GrIS. Height anomalies from Greenland to Beaufort Sea favor the largest anomalies in meltwater production, and positive height anomalies in this configuration have shown the greatest increase in frequency of any pattern in the study period.

Acknowledgements

I sincerely thank all the people who helped make this work possible. I gratefully thank Dr. David Robinson, my PhD committee chair, for his time and insight in guiding this project, for patience and encouragement, and for helping me develop professionally. Thank you to Dr. Åsa Rennermalm, who served as a de facto second committee chair in her devoted time and effort, and contributed immensely with her enthusiasm and encouragement. Many research obstacles were cleverly avoided and overcome in countless conversations with her. Thanks also to the other members of my committee, Drs. Tom Mote and Jennifer Francis for their helpful comments and insight on this work as it progressed. I would like to thank Tom Estilow for years of help in obtaining and regridding different datasets from the Global Snow Lab. I thank the faculty and staff of the Rutgers University Geography Department for their help and service throughout my time here, and particularly Johnny Nunez, who helped me take advantage of computing resources and options I was otherwise unaware of. Nelun Fernando deserves special thanks for her initial mentorship and friendship early on. She went far beyond these mentoring duties and helped me through coursework, data acquisition, statistical problems, and got me through Matlab's learning curve. I also thank Imtiaz Rangwala for his extensive assistance in NCL. The scope and direction of this research has been shaped by useful conversations with Debjani Ghatak, Weihan Chan, Gina Henderson, Chris Derksen, Elena Maksimovich, Libo Wang, Julienne Stroeve, Vena Chu, and Samiah Moustafa. In addition, the importance cannot be understated of friends and fellow doctoral students around the university who have provided a network of support in

graduate school life. Last, I want to acknowledge the support of my family along the way. The support and encouragement from my fiancée and best friend, Susan Coiner-Collier, has been invaluable. I am also deeply grateful for the support of my parents, who have instilled in me a desire to learn and improve myself, and have always been encouraging and accommodating in the pursuit of my interests and goals.

This research has been supported financially by a School of Arts and Sciences Excellence Fellowship, NASA NESSF grant NNX13AO44H, NASA MeASUREs grant NN-H-06-ZD-A001, a CUAHSI Pathfinder travel award, and the graduate school of New Brunswick which largely supported my final semester.

Table of Contents

List of Tables

List of Figures

Chapter 1: Introduction

1.1 **Background**

The Arctic is undergoing a period of rapid change brought about by increasing temperatures (ACIA 2005; Lemke et al. 2007; AMAP 2011). Accelerating warming since the 19th century has occurred in an abrupt reversal of an Arctic-wide cooling trend extending at least 2000 years before present (Kaufman et al. 2009). The enhanced warming near the surface relative to above the Arctic boundary layer suggests that much of this warming is related to cryospheric feedbacks due to summer sea ice loss and spring snow disappearance, resulting in enhanced near-surface warming (Serreze et al. 2009; Kumar et al. 2010; Chung and Raisanen 2011). Enhanced poleward heat advection likely plays a lesser role based on weaker trends in mid-tropospheric warming (Graversen et al. 2008; Screen and Simmonds 2010). It is primarily due to the feedbacks involved in near-surface warming that temperature increases in the Arctic have been amplified relative to the rest of the earth. (Serreze and Francis 2006).

Accelerating warming has caused substantial changes to the Arctic environment. Changes in these ecosystems are primarily driven by sea ice loss and warmer temperatures that are shifting species range and habitats northward and higher in elevation (Moore and Huntington 2008). Wildfire frequency has increased and is predicted to continue to do so as a result of warmer and drier summer conditions, as well as due to shifts in vegetation type (Flannigan et al. 2009). Some of the associated changes in vegetation have strong impacts on surface climate feedbacks. It is likely that

continued vegetation changes will generate net positive feedbacks in warming that will continue to amplify Arctic warming (Pearson et al. 2013).

Accompanying Arctic warming is an increase in storminess and precipitation, particularly over the Arctic Ocean. While precipitation trends are difficult to gauge due to its high variability and limited observational network, the best estimates of trends from in situ data indicate a 5% increase in the 1951 – 2009 period (Walsh et al. 2012) and have been linked to anthropogenic forcing (Min et al. 2008). In future simulations, global climate models project an increase of Arctic precipitation under all scenarios (Overland et al. 2011). Much of this occurs as a result of decreased sea level pressure (SLP), which has exhibited a significant trend downward regionally and toward stronger cyclones in all simulations of the Community Climate System Model (CCSM4; Vavrus et al. 2012). The strong correlation among variables such as temperature, precipitation, SLP, cloud cover, and sea ice concentration suggests that their close coupling represents a fingerprint of Arctic climate change.

At its winter maximum, snow covers nearly half of northern hemisphere's land surface from 45×10^6 km^2 in January to just 2×10^6 km^2 in August (Lemke et al. 2007) (**Fig. 1**). Its large seasonal variability and distinctive physical properties make snow cover an important component of the cryosphere and the Earth's climate system. For example, the spring snow melt season is an important element of hydrologic and ecological systems, and serves as a reservoir when it melts in the spring (Nijssen et al. 2001; Yang et al. 2003; Barnett et al. 2005). In addition, variations in snow cover extent have been shown to have a significant effect on surface energy and mass exchanges over Arctic land

(Serreze et al. 2000; Serreze et al. 2003; Yang et al. 2003). Finally, its variations serve as a control of climate changes over its coverage area, influencing atmospheric conditions regionally (Groisman et al. 1994, Frei and Robinson 1999, Robinson and Frei 2000).

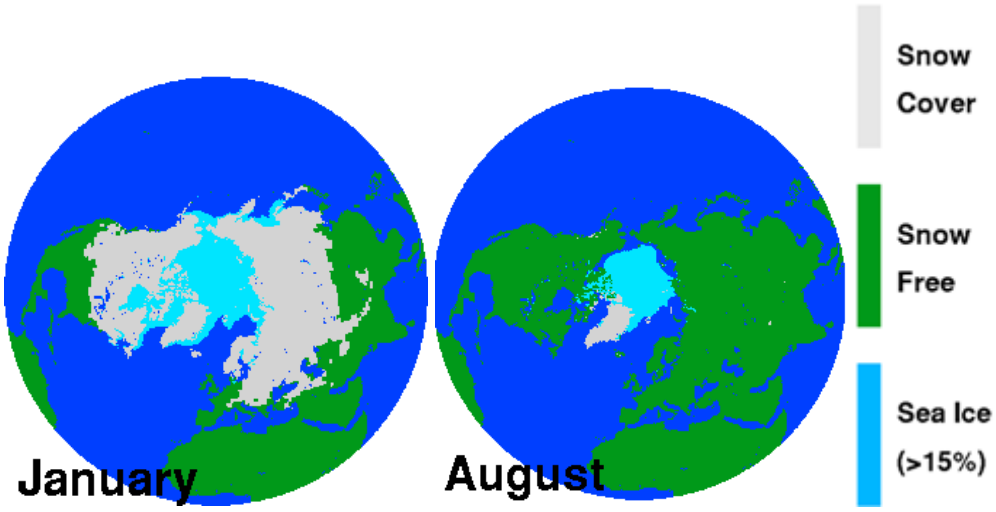

Fig. 1) 1966 – 2010 average snow extent in January and August. Figure modified from Armstrong and Brodzik, NSIDC.

The largest and most consistent change in snow cover is its earlier spring disappearance. As the Arctic warms, terrestrial spring snow melt has occurred an average of two to four weeks earlier than it did in the late 1970's (Foster et al. 2008; Tedesco et al. 2009, Takala et al. 2009, Wang et al. 2013). Northern Hemisphere snow cover across the entire spring season has shown similar earlier melt trends responding to warmer temperatures and changes in atmospheric circulation (Dye 2002; Brown 2000; Dery and Brown 2007), with less pronounced trends over North America than Eurasia (Dyer and Mote 2006; Brown and Robinson 2011; Brown et al. 2010, Derksen and Brown 2012) which is also consistent with earlier snow melt onset (Wang et al. 2013). The most important variables controlling snow melt are radiative fluxes, energy advection,

turbulent heat fluxes, and the temperature departures that synthesize these (Groisman et al. 1994; Zhang et al. 1997; Aizen et al. 2000; Ohmura 2001). But it is unclear whether warmer temperatures primarily drive increased melt, or whether warmer temperatures are a consequence of the earlier melt. It is also uncertain what causes these temperature departures, and temperature departures are not always responsible for earlier melt. Therefore, understanding drivers of snow melt is critical for assessing current trends in snow cover and predicting future responses to Arctic and global change.

Elsewhere in the Arctic, the Greenland Ice Sheet (GrIS) mass balance is experiencing an annual net loss with accelerating negative trends being driven by increased surface melt (Mote 2007; Fettweis et al. 2011). This melt extent has also increased in coverage recently, reaching further into the accumulation zone as major warming events have become more common (Mernild et al. 2011; Hall et al. 2013). Melt from the GrIS has contributed about 5 mm to sea level rise in the most recent decade (van den Broeke et al. 2009) and is predicted to be the dominant contributor to sea level rise along with Antarctica by the end of the century (Rignot et al. 2011). Containing about 2.85×10^6 km^3 of ice, Greenland's importance is primarily its contribution to sea level rise, though it has also served as a sensitive indicator of broader global climate change. The ability to better attribute variability in surface melt would improve surface mass balance models and ultimately lead to improved understanding of this component of the Arctic climate system.

Concurrent with GrIS mass loss, Arctic sea ice is declining in coverage in all seasons, and has also exhibited accelerating losses recently (Stroeve et al. 2012; Cavalieri

and Parkinson 2012). The summer ice-free season is now up to three months longer where ice loss has been greatest (Stammerjohn et al. 2012), with autumn freeze-up occurring later primarily because the warmer ocean requires longer to cool (Laxon et al. 2003). Ice thickness has also been decreasing as multi-year ice melts and is replaced by young ice vulnerable to summer melt. Sea ice ranges from its peak of over 14 million km^2 in March to under 5 million km^2 in September (Fig. 1.2), with the greatest variability and change in the marginal ice zone. Simulations of future sea ice extent indicate greater losses are expected in summer than winter, likely evolving into an ice-free Arctic in September within the next few decades (Wang and Overland 2010; Overland and Wang 2013). Such ice losses will have even greater impacts on Arctic meteorology, hydrology, and ecology, most notably through changes in atmospheric humidity, cloud cover, precipitation, and ocean temperature and salinity.

These important components of the Arctic cryosphere have therefore become a leading indicator of climate change globally, and the future evolution of the climate system depends on their interaction with the atmosphere, ocean, and each other. Developing a better understanding of these interactions requires a comprehensive, process-based approach that incorporates a large part of this system. This research project takes this approach to identify these physical processes and develop linkages among the components of the climate system to address these research questions.

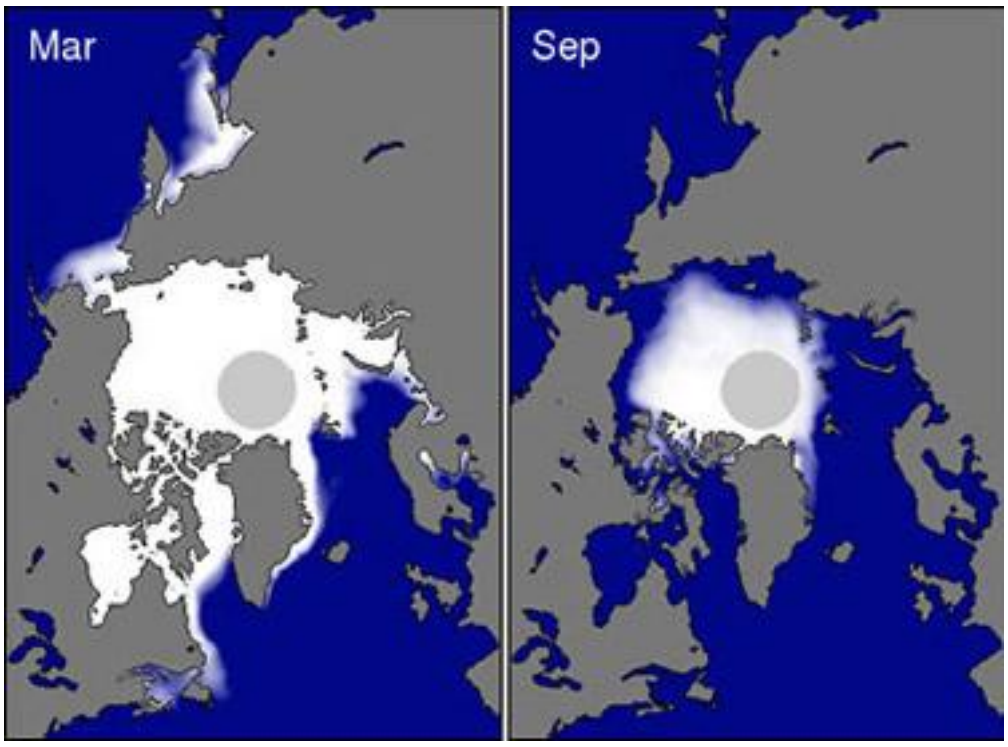

Fig. 1.2) 1979-2010 average March and September Arctic sea ice concentration. Figure modified from NSIDC website.

1.2 Data and Methodological Considerations

The melt onset date (MOD) is the focus of this research for multiple reasons. First, it is important in the climate system due to its ability to initiate feedbacks primarily by immediately reducing the surface albedo. Second, it is easier to detect than some other comparable measures of Arctic change. The change from ice to liquid in the surface and near-surface of the snowpack can be detected relatively easily by passive microwave sensors, with a record extending to 1979. Snow cover disappearance, a comparable measure of snowcover changes over land, is more difficult to measure and somewhat arbitrary to define due to uneven melting patterns and difficulty of observation beneath

the forest and shrub canopy in many parts of the world. The ability to accurately detect the MOD facilitates easier analysis of its changes over more than three decades, and allows for an analysis of its effects on subsequent climate processes. Finally, a comprehensive energy balance approach lends itself well to attributing snow melt onset due to the abrupt changes in the energy balance terms after this date.

This work focuses on snow melt onset, its trends and attribution, and its relationship with other components of the climate system. The scope and nature of these questions necessitates a comprehensive analysis that allows for easy comparison of multiple scales of data over a long time period, with the understanding that the components and processes of the Arctic climate system are often part of a highly related system of cause and effect. Consequently, data used here are primarily atmospheric reanalysis, regional climate model output, and remote sensing observations at a spatial and temporal resolution high enough to resolve important small-scale variability, but small enough to remain manageable in analysis. Addressing these questions that involve multiple fields of large and high-dimensional datasets is best suited for data mining and statistical analyses. These methods include singular value decomposition (SVD), principal component analysis (PCA), self organizing maps (SOM), simple and partial correlations, trend analysis, composites of the atmospheric geopotential height field, and inter-seasonal and extreme year analysis. Inputs into these analyses are comprised of a comprehensive list of atmospheric and hydrologic variables chosen based on their ability to provide multiple lines of evidence to support each of the conclusions.

1.3 Dissertation Organization

A near-hemispheric overview of terrestrial snow melt onset is first done to attribute earlier trends and variability in the MOD across much of northern hemisphere land using a comprehensive set of energy balance terms ranging from surface temperature, atmospheric energy advection, and cloud fraction. This large-scale analysis of terrestrial snow melt uses data from the satellite era, 1979-2012, which also allows trend analysis in this date and its energy balance to be undertaken. Much of the analysis is broken down in scale into regions to facilitate analysis and compare easily among locations with different physical characteristics. An attribution analysis is further performed using principal component regression, correlations between component loadings and mean surface atmospheric pressure, and a more detailed analysis of the influence of cloud cover and energy advection on the MOD.

Next, analysis focuses on part of northern Canada west of Hudson Bay. This study region was chosen for its relatively flat and homogeneous land cover and its late average MOD. A range of near-surface energy and atmospheric variables in northern Canada are analyzed at the beginning of the melt season. Emphasis is placed on the date of melt onset in three distinct sub regions to isolate the primary regional differences. This is followed by a comparison of energy balance terms to evaluate the importance of each term relative to each other, and how they differ regionally. Attribution of melt is examined primarily with analysis of extreme early and late melt years, synoptic pattern composites, and separation of the contribution between radiative and synoptic influences on the MOD using variable thresholds.

Finally, Chapter 4 shifts analysis of melt onset beyond terrestrial snow to the

remainder of the Arctic, including the onset of snow melt on sea ice and on the Greenland ice sheet. This focuses less on attribution than potential linkages among these two fields as well as the atmospheric circulation during the spring and summer months. This is because the MOD over sea ice and the GrIS is found to be less important to these systems than the subsequent summer melt season and their interactions. Different types of statistical methods that facilitate analysis of multiple covarying spatio-temporal datasets are employed for this purpose, identifying how and where these relationships appear most strongly. The analysis also explores the important question of to what extent sea ice variability and loss near Greenland can influence surface melt on the ice sheet and therefore the ice sheet surface mass balance.

References

ACIA. 2005. Arctic climate impact assessment. 1042 pp. Cambridge: Cambridge University Press.

AMAP, 2011. Snow, water, ice and permafrost in the Arctic (SWIPA). Arctic Monitoring and Assessment Programme (AMAP), Oslo.

Aizen, E. M., V. B. Aizen, J. M. Melack, and A. N. Krenke, 2000: Heat exchange during snow ablation in plains and mountains of Eurasia. *J. Geophys. Res.*, 105, 27,013-27,022.

Barnett, T. P., J. C. Adam, and D. P. Lettenmaier, 2005: Potential impacts of a warming climate on water availability in snow-dominated regions. *Nature*, **438**, 303–309, doi:10.1038/nature04141.

van den Broeke, M., and Coauthors, 2009: Partitioning recent Greenland mass loss. *Science*, **326**, 984–986, doi:10.1126/science.1178176.

Brown, R., C. Derksen, and L. Wang, 2010: A multi-data set analysis of variability and change in Arctic spring snow cover extent, 1967–2008. *J. Geophys. Res.*, **115**, D16111, doi:10.1029/2010JD013975.

Brown, R. D., 2000: Northern Hemisphere Snow Cover Variability and Change, 1915 – 97. *J. Clim.*, **13**, 2339–2355.

Brown, R. D., and D. A. Robinson, 2011: Northern Hemisphere spring snow cover variability and change over 1922–2010 including an assessment of uncertainty. *Cryosph.*, **5**, 219–229, doi:10.5194/tc-5-219-2011.

Cavalieri, D. J., and C. L. Parkinson, 2012: Arctic sea ice variability and trends, 1979–2010. *Cryosph.*, **6**, 881–889, doi:10.5194/tc-6-881-2012.

Chung, C. E., and P. Räisänen, 2011: Origin of the Arctic warming in climate models. *Geophys. Res. Lett.*, **38**, n/a–n/a, doi:10.1029/2011GL049816.

Day, J. J., J. L. Bamber, and P. J. Valdes, 2013: The Greenland Ice Sheet's surface mass balance in a seasonally sea ice-free Arctic. *J. Geophys. Res. Earth Surf.*, **118**, 1533–1544, doi:10.1002/jgrf.20112. http://doi.wiley.com/10.1002/jgrf.20112.

Derksen, C., and R. Brown, 2012: Spring snow cover extent reductions in the 2008–2012 period exceeding climate model projections. *Geophys. Res. Lett.*, **39**, L19504, doi:10.1029/2012GL053387.

Déry, S. J., and R. D. Brown, 2007: Recent Northern Hemisphere snow cover extent trends and implications for the snow-albedo feedback. *Geophys. Res. Lett.*, **34**, L22504, doi:10.1029/2007GL031474.

Dye, D. G., 2002: Variability and trends in the annual snow-cover cycle in Northern Hemisphere land areas. *Hydrol. Process.*, **16**, 3065–3077.

Dyer, J. L., and T. L. Mote, 2006: Spatial variability and trends in observed snow depth over North America. *Geophys. Res. Lett.*, **33**, L16503, doi:10.1029/2006GL027258.

Fettweis, X., M. Tedesco, M. van den Broeke, and J. Ettema, 2011: Melting trends over the Greenland ice sheet (1958–2009) from spaceborne microwave data and regional climate models. *Cryosph.*, **5**, 359–375, doi:10.5194/tc-5-359-2011.

Flannigan, M., Stocks, B., Turetsky, M. and Wotton, M. (2009), Impacts of climate change on fire activity and fire management in the circumboreal forest. Global Change Biology, **15**, 549–560. doi:10.1111/j.1365-2486.2008.01660.x

Foster, J. L., D. A. Robinson, D. K. Hall, and T. W. Estilow, 2008: Spring snow melt timing and changes over Arctic lands. *Polar Geography*, **31**, 145–157.

Frei, A., and D. Robinson, 1999: Northern Hemisphere snow extent: Regional variability 1972–1994. *Int. J. Climatol.*, **19**, 1535–1560.

Graversen, R. G., T. Mauritsen, M. Tjernström, E. Källén, and G. Svensson, 2008: Vertical structure of recent Arctic warming. *Nature*, **451**, 53–56, doi:10.1038/nature06502.

Groisman, P. Y., T. R. Karl, and R. W. Knight, 1994: Observed impact of snow cover on the heat balance and the rise of continental spring temperatures. *Science*, **263**, 198–200.

Hall, D. K., J. C. Comiso, N. E. DiGirolamo, C. a. Shuman, J. E. Box, and L. S. Koenig, 2013: Variability in the surface temperature and melt extent of the Greenland ice sheet from MODIS. *Geophys. Res. Lett.*, **40**, 2114–2120, doi:10.1002/grl.50240.

Kaufman, D. S., and Coauthors, 2009: Recent warming reverses long-term arctic cooling. *Science*, **325**, 1236–1239, doi:10.1126/science.1173983.

Koenig, S. J., R. M. Deconto, and D. Pollard, 2014: Impact of reduced Arctic sea ice on Greenland ice sheet. *Geophys. Res. Lett.*, **41**, 3934–3943, doi:10.1002/2014GL059770.A.

Kumar, A., and Coauthors, 2010: Contribution of sea ice loss to Arctic amplification. *Geophys. Res. Lett.*, **37**, L21701, doi:10.1029/2010GL045022.

Laxon, S. W., and Coauthors, 2013: CryoSat-2 estimates of Arctic sea ice thickness and volume. *Geophys. Res. Lett.*, **40**, 732–737, doi:10.1002/grl.50193.

Lemke, P., and Coauthors, 2007: Observations: Changes in snow, ice and frozen ground. Climate Change 2007: The Physical Science Basis, S. Solomon et al., Eds., Cambridge University Press, 337–383.

Mernild, S. H., T. L. Mote, and G. E. Liston, 2011: Greenland ice sheet surface melt extent and trends: 1960–2010. *J. Glaciol.*, **57**, 621–628, doi:10.3189/002214311797409712.

Min, S.-K., X. Zhang, and F. Zwiers, 2008: Human-induced Arctic moistening. *Science*, **320**, 518–520, doi:10.1126/science.1153468.

Moore, S. E., and H. P. Huntington, 2008: Arctic marine mammals and climate change: impacts and resilience. *Ecol. Appl.*, **18**, 157–165.

Mote, T. L., 2007: Greenland surface melt trends 1973-2007: Evidence of a large increase in 2007. *Geophys. Res. Lett.*, **34**. doi: 10.1029/2007GL031976.

Nijssen, B., G. O'Donnell, A. Hamlet, and D. Lettenmaier, 2001: Hydrologic sensitivity of global rivers to climate change. *Clim. Change*, 50, 143–175.

Ohmura, A., 2001: Physical Basis for the Temperature-Based Melt-Index Method. *J. Appl. Meteorol.*, **40**, 753–761.

Overland, J. E., and M. Wang, 2010: Large-scale atmospheric circulation changes are associated with the recent loss of Arctic sea ice. *Tellus A*, **62**, 1–9, doi:10.1111/j.1600-0870.2009.00421.x.

Overland, J. E., M. Wang, N. a. Bond, J. E. Walsh, V. M. Kattsov, and W. L. Chapman, 2011: Considerations in the Selection of Global Climate Models for Regional Climate Projections: The Arctic as a Case Study*. *J. Clim.*, **24**, 1583–1597, doi:10.1175/2010JCLI3462.1.

Pearson, R. G., S. J. Phillips, M. M. Loranty, P. S. a. Beck, T. Damoulas, S. J. Knight, and S. J. Goetz, 2013: Shifts in Arctic vegetation and associated feedbacks under climate change. *Nat. Clim. Chang.*, **3**, 673–677, doi:10.1038/nclimate1858.

Rignot, E., I. Velicogna, M. R. van den Broeke, a. Monaghan, and J. Lenaerts, 2011: Acceleration of the contribution of the Greenland and Antarctic ice sheets to sea level rise. *Geophys. Res. Lett.*, **38**, 1–5, doi:10.1029/2011GL046583.

Rinke, A., W. Maslowski, K. Dethloff, and J. Clement, 2006: Influence of sea ice on the atmosphere: A study with an Arctic atmospheric regional climate model. *J. Geophys. Res.*, **111**, D16103, doi:10.1029/2005JD006957.

Robinson, D., and A. Frei, 2000: Seasonal variability of Northern Hemisphere snow extent using visible satellite data. *Prof. Geogr.*, **52**, 307–315.

Screen, J. a, and I. Simmonds, 2010: The central role of diminishing sea ice in recent Arctic temperature amplification. *Nature*, **464**, 1334–1337, doi:10.1038/nature09051.

Serreze, M. C., and Coauthors, 2000: Observational Evidence of Recent Change in the Northern High-Latitude Environment. *Clim. Change*, **46**, 159-207.

Serreze, M. C., and Coauthors, 2003: A record minimum arctic sea ice extent and area in 2002. *Geophys. Res. Lett.*, **30**, 1110, doi:10.1029/2002GL016406.

Serreze, M. C., A. P. Barrett, J. C. Stroeve, D. N. Kindig, and M. M. Holland, 2009: The emergence of surface-based Arctic amplification. *Cryosph.*, **3**, 11–19.

Stammerjohn, S., R. Massom, D. Rind, and D. Martinson, 2012: Regions of rapid sea ice change: An inter-hemispheric seasonal comparison. *Geophys. Res. Lett.*, **39**, L06501, doi:10.1029/2012GL050874.

Stroeve, J. C., M. C. Serreze, M. M. Holland, J. E. Kay, J. Malanik, and A. P. Barrett, 2012: The Arctic's rapidly shrinking sea ice cover: a research synthesis. *Clim. Change*, **110**, 1005–1027, doi:10.1007/s10584-011-0101-1.

Takala, M., J. Pulliainen, S. Member, S. J. Metsämäki, and J. T. Koskinen, 2009: Detection of Snowmelt Using Spaceborne Microwave Radiometer Data in Eurasia From 1979 to 2007. *IEEE Trans. Geosci. Remote Sens.*, **47**, 2996–3007.

Tedesco, M., M. Brodzik, R. Armstrong, M. Savoie, and J. Ramage, 2009: Pan arctic terrestrial snowmelt trends (1979–2008) from spaceborne passive microwave data and correlation with the Arctic Oscillation. *Geophys. Res. Lett.*, **36**, doi:10.1029/2009GL039672.

Vavrus, S. J., M. M. Holland, A. Jahn, D. a. Bailey, and B. a. Blazey, 2012: Twenty-First-Century Arctic Climate Change in CCSM4. *J. Clim.*, **25**, 2696–2710, doi:10.1175/JCLI-D-11-00220.1.

Walsh, J. E., J. E. Overland, P. Y. Groisman, and B. Rudolf, 2012: Ongoing Climate Change in the Arctic. *Ambio*, **40**, 6–16, doi:10.1007/s13280-011-0211-z.

Wang, M., and J. E. Overland, 2012: A sea ice free summer Arctic within 30 years: An update from CMIP5 models. *Geophys. Res. Lett.*, **39**, L18501, doi:10.1029/2012GL052868

Wang, L., C. Derksen, R. Brown, and T. Markus, 2013: Recent changes in pan-Arctic melt onset from satellite passive microwave measurements. *Geophys. Res. Lett.*, **40**, 522-528, doi:10.1002/grl.50098.

Yang, D., Y. Zhao, R. Armstrong, D. Robinson, and M.-J. Brodzik, 2007: Streamflow response to seasonal snow cover mass changes over large Siberian watersheds. *J. Geophys. Res.*, **112**, F02S22, doi:10.1029/2006JF000518.

Zhang, T., S. A. Bowling, and K. Stamnes, 1997: Impact of the atmosphere on surface radiative fluxes and snowmelt in the Arctic and Subarctic. *J. Geophys. Res.*, **9**, 2110-2123, doi:10.1029/96JD02548.

Chapter 2: Controls on Spatial and Temporal Variability in Northern Hemisphere Terrestrial Snow Melt Timing, 1979-2012

2.1 Introduction

The Arctic climate system has undergone rapid changes in the late 20th and 21st centuries (Lemke et al. 2007). Increased global temperatures are associated with accelerating losses in sea ice, glacial mass balance, permafrost, and snow cover extent and duration (Serreze et al. 2009; Liston and Hiemstra 2011; Camill 2005; Comiso et al. 2008; Johannessen et al. 2004, Post et al. 2009). Amplified warming in the Arctic relative to lower latitudes has occurred primarily as a result of feedbacks in the cryosphere, particularly the reduction in albedo associated with spring snow loss (Serreze and Francis 2006; Dery and Brown 2007). This amplified warming also potentially influences mid-latitude weather patterns (Francis and Vavrus 2012; Tang et al. 2014). Snow cover is a major component of the cryosphere and the Earth's climate system, playing a central role in some of these feedbacks. However, despite the importance of terrestrial snow cover, spatiotemporal variability in spring snow melt drivers is poorly understood.

As the Arctic warms, terrestrial spring snow melt (particularly snow disappearance) has occurred an average of two to four weeks earlier than it did in the late 1970's (Foster et al. 2008; Tedesco et al. 2009, Takala et al. 2009, Wang et al. 2013), although attributing these changes has been a challenge (Rupp et al. 2013). June snow cover extent has declined the most rapidly during this period, faster than the trend in

September sea ice loss (Derksen and Brown 2012) and by nearly 50% since 1967 (Brown et al. 2010). Northern Hemisphere snow cover across the entire spring season has shown similar earlier melt trends responding to warmer temperatures and changes in atmospheric circulation (Dye 2002; Brown 2000; Dery and Brown 2007; Wang et al. 2013), with less pronounced trends over North America than Eurasia (Dyer and Mote 2006; Brown and Robinson 2011; Wang et al. 2013; Ye et al. 2015). The regional and monthly differences in these trends suggest that melt drivers may exhibit considerable variability, requiring attribution that adequately resolves these differences.

It is well understood that the most important variables controlling snow melt are radiative fluxes, energy advection, turbulent heat fluxes, and the temperature departures that synthesize these (Groisman et al. 1994; Zhang et al. 1997; Aizen et al. 2000; Ohmura 2001; Kapsch et al. 2013; Mioduszewski et al. 2014). Furthermore, the time period in which snow can begin melting is generally controlled by insolation, whereas inter-annual variation in this date can mostly be attributed to variability in downwelling longwave (LW) radiation, which is largely a function of cloud cover variations and heat and moisture transport changing the mean atmospheric thickness (Zhang et al. 2001; Sedlar and Devasthale 2012; Kapsch et al. 2013; Kapsch et al. 2014). Regionally, radiative fluxes have been found to play a larger role in melt energy at high latitudes, with advective energy and resultant sensible heat fluxes contributing more to melt at lower latitudes and earlier in the season (Ohmura 2001; Leathers and Robinson 1997; Zhang et al. 1996, 1997; Semmens et al. 2013). Turbulent fluxes can be important in the lower latitudes by enhancing or counteracting radiative fluxes (Male and Granger 1981), but have not been found to be significant drivers of snow melt on a large scale (Liston and

Heimstra 2011; Shi et al. 2013).

Synoptic conditions that generate the patterns that control energy advection have been studied on a regional and hemispheric scale (Aizen et al. 2000; Bamzai 2003; Vicente-Serrano et al. 2006; Ueda et al. 2003; Tedesco et al. 2009; Shi et al. 2011; Shi et al. 2013; Ye et al. 2015). There has been some success correlating winter snow conditions and subsequent melt season timing with teleconnections such as the Arctic Oscillation and Pacific North American pattern, with up to 50% of the variance in these conditions explained in some regions (Tedesco et al. 2009; Bamzai 2003; Brown and Goodison 1996). Spring snow conditions also correlate with geopotential heights and modes of atmospheric circulation (Vicente-Serrano et al. 2006; Stone et al. 2002; Bao et al. 2011), but correlation strengths again depend on the region as well as methodological considerations such as time lags and spatial and temporal averaging. For example, using monthly averages not only removes some of the signal, but introduces mixed environmental conditions by incorporating both snow-covered (melting and frozen) and snow-free surfaces into the analysis, particularly one that covers many melt seasons.

A detailed analysis of energy balance terms is another method in understanding the snow melt process. While synoptic conditions generally control these terms, atmospheric teleconnections are only a metric for certain modes of regional circulation, which are then manifested through the surface energy balance. Small- and point-scale studies of snow melt attribution often have the advantage of utilizing energy balance data at a high temporal resolution in detailed analysis (e.g. Sicart et al. 2006; Stone et al. 2002; Pomeroy et al. 2003; Marsh et al. 2010; Gleason et al. 2013), but can be difficult to

generalize beyond the unique geography of the study location and are often limited to one melt season. Larger scale energy balance studies have had some success attributing spring snow melt while operating within a different set of constraints. Iijima et al. (2007) concluded that the advection of heat and moisture played the greatest role in eastern Siberian snow ablation, while Ueda et al. (2003) found that early snow melt years on the East European Plain are associated with anomalous low-level warm air advection.

Here, we use atmospheric reanalysis data to assess trends in the melt onset date (MOD) and its drivers, and to attribute MOD variability in distinctive regions. Regions of homogeneous snow melt are identified using principal component analysis (PCA) and much of the analysis proceeds using these regions. Thirty four year trends in MOD and melt forcing variables are obtained using the Mann Kendall trend test and Sen's slope to assess regional MOD and its drivers. An attribution analysis is further performed using principal component regression, correlations between component loadings and mean surface atmospheric pressure, and a more detailed analysis of the influence of cloud cover and energy advection on MOD. Maintaining the focus on the surface energy balance allows for a unique and improved understanding of what type of forcing is necessary to initiate the snow melt season, while combining these multi-scaled approaches over a relatively long time period places results in the context of the observed hemispheric changes in snow melt onset.

2.2 Study Area

The study area includes all land between 55º N and 75º N, hereafter Northern Hemisphere. The study area is divided into two regions for display purposes: the North

Eurasian region is denoted E and is bounded by 40° E – 180° E, while the North American region is denoted N and bounded by 170° W – 60° W. Snow cover characteristics across this large area tend to be almost exclusively tundra and taiga as defined by Sturm et al. (1995). All of the Arctic coast, particularly Canada north and west of Hudson Bay, is characterized by bare or shrubby tundra, which transitions into generally taiga of varying canopy height and density in the remainder of this area (e.g. Bicheron et al. 2008). This area is further divided into subregions of homogeneous snow melt onset for analysis, the methodology of which is described in section 2.3 (Fig. 2.1).

2.3 MERRA Data

Near-surface energy balance and atmospheric variables, hereafter forcing variables, were obtained from the National Aeronautics and Space Administration Modern Era Retrospective-Analysis for Research and Applications (MERRA) products (Bosilovich et al. 2011; Cullather and Bosilovich 2011, 2012; Rienecker et al. 2011). MERRA is run on a 1/2° latitude by 2/3° longitude global grid with 72 hybrid-sigma vertical levels to produce analyses at 6-h intervals covering the modern satellite era from 1979 to present. Data were obtained for a 122-day period from March 1 – June 30 capturing the melt season from 1979 – 2012. The earliest mean MOD is in mid-late March, so there are a few grid cells during the earliest melt years when the MOD is earlier, but the effect of this on the analysis is insignificant.

Different MERRA variables were used for different analyses depending on what was most appropriate, and include: Net and incoming shortwave (SW) and longwave (LW) radiation, LW and SW cloud radiative effect (CRE), sensible heat fluxes (positive

fluxes moving from the snow surface to the atmosphere), 2 m daily mean and maximum temperature, diurnal temperature range, 850 hPa temperature and specific humidity, and 1000-500 hPa thicknesses. Energy convergence is also included, and is defined in terms of the remaining energy balance terms as

$$-\nabla \cdot \tilde{F}A \equiv Rtop + Fsfc - \frac{\partial AE}{\partial t}$$

where R_{top} is the downward radiative flux at the top of the atmosphere, F_{sfc} is the net surface energy flux (positive upwards), and A_E is the total energy in the atmospheric column. Energy convergence is obtained using a combination of MERRA moist static energy fields following Cullather and Bosilovich (2012, Appendix). It should be noted that there is redundancy in EC, which is primarily the convergence of moist static energy into the atmospheric column, and as such includes water vapor and is a strong mechanism for influencing downwelling LW radiation. EC was chosen over other alternatives such as sensible heat advection or u- and v-component transport based on ease of computation and to apply a comprehensive analysis of all the components of this term, even with redundancy. This type of integrative approach is more aligned with this type of large-scale analysis, whereas it would be important for a case study to resolve EC into its components moreso than done here.

All of these variables were aggregated from hourly to daily, though daily temperatures were derived from hourly 2 m temperature data. Statistical significance of trends at $\alpha = 0.05$ in forcing variables as well as the date of melt onset were analyzed using a Mann-Kendall trend test (Mann 1945, Kendall 1975), with the associated Sen's Slope applied to the data to obtain a change over the 34-year period (Helsel and Hirsch

2002)

MERRA has been evaluated extensively since its release (Cullather and Bosilovich 2012; Reichle et al. 2011; Robertson et al. 2011; Kennedy et al. 2011; Zib et al. 2012), but is subject to many of the limitations of other reanalysis systems. Because most of the data assimilated into MERRA are from remote sensing products, calibration issues across different platforms in the last 35 years potentially introduce some bias into the outputs. These tend to be strongest over lower latitudes and over the ocean (Bosilovich et al. 2011; Robertson et al. 2011), with the greatest influence in the Arctic likely being negative biases in water vapor and downward LW radiation (Bosilovich et al. 2011; Kennedy et al. 2011). However, many of MERRA's energy balance and advective terms used in this study have demonstrated some of the lowest biases among reanalysis products in comparison and validation studies (Cullather and Bosilovich 2011; Zib et al. 2012; Lindsay et al. 2014).

2.4 Melt Onset Data

The annual melt onset date (MOD) data was obtained from Wang et al (2013; updated to 2012). Here, we briefly introduce the satellite data and the melt detection algorithm. Satellite-borne microwave sensors are effective tools for examining changes in snow melt dynamics over the Arctic due to their high sensitivity to liquid water in snow and the general absence of cloud cover issues faced in visible imagery analysis (e.g. Glen and Paren 1975, Zwally and Gloersen 1977). Melt onset was determined using an algorithm based on temporal variations in the differences of the brightness temperature (Tb) between 19 GHz and 37 GHz (vertical polarization) from passive microwave

satellite data (Wang et al. 2013). A continuous time series of daily Tb was obtained from the Scanning Multichannel Microwave Radiometer (SMMR, 1979–1987), SSM/I (1987 to 2008), and the Special Sensor Microwave Imager/Sounder (SSMIS, 2009-2012) mapped to the 25 km EASE-Grid available at the National Snow and Ice Data Center in Boulder, Colorado (Armstrong et al. 1994; Knowles et al. 2002). Sensor cross calibration was performed by applying adjustment coefficients derived in previous studies (Abdalati et al. 1995; Jezek et al. 1993; Stroeve et al. 1998). Since our melt detection algorithm only uses the relative change in the temporal variations in Tb, slight offsets in Tbs between sensors should not affect algorithm performance. Nevertheless, the differences in the SMMR and SSM/I(S) sensors may still introduce some uncertainties in the long-term trends of MOD, and changes in sensor calibration could potentially have caused an apparent but not real change in MOD. As explained in Tedesco et al. (2009), this uncertainty cannot be quantified, but these data were calibrated as well as possible by Wang et al. (2013). The gaps in the SMMR data (due to its narrower swath and availability of every other day) and SSM/I(S) data are filled by linear interpolation from adjacent days.

The melt detection algorithm is capable of distinguishing early periodic snow melt onset from the main seasonal melt onset (Wang et al. 2008; 2013). Multiple melt events were determined based on temporal variations in the differences of the brightness temperature between 19 GHz and 37 GHz (TbD =19 v - 37 v) from the passive microwave satellite measurements. The MOD was detected if the difference in daily TbD and the previous 3-day average (M) was greater than a threshold (TH1=0.35 x M) for four or more consecutive days. An iterative approach was used for melt end date (MED)

detection: melt end was detected as the first day when daily TbD was less than a threshold (TH2=mean TbD in July + 7K) for at least 28 continuous days. If these conditions were not met at a given grid cell, the number of days was reduced from 28 to 21, and then to 14 if necessary. Melt duration was the number of days between MOD and MED for each melt event, with the main melt event identified as the event with the longest melt duration. More details on the determination of the melt detection thresholds can be found in Wang et al. (2013).

The melt detection algorithm was evaluated using observations at weather stations across the pan-Arctic (Wang et al., 2008; 2013). The results showed that the primary MOD was associated with the early stage of the final ablation of the snowpack when the snowpack was wet but still fully covering the ground. The detected MODs corresponded to a clear shift in the statistical distribution of mean daily air temperatures from largely below freezing to above freezing. Since melt characteristics and melt season timing over permanent snow and ice are different from seasonal snow cover over land, a land ice mask was used to mask out those areas in our analysis (Brown et al. 1998). Due to the uncertainty of microwave measurements in complex alpine terrains (e.g. Tong et al. 2010), the performance of the melt detection algorithm in mountainous areas may have a larger uncertainty and needs to be tested further.

For melt attribution analysis, this MOD dataset is regridded to the MERRA model grid using a patch recovery interpolation method (Zienkiewicz and Zhu 1992). This interpolation method is a type of finite element method that operates by determining (recovering) the derivatives of the finite elements at each node of the generated data

mesh. Though computationally more expensive than more common piecewise polynomial interpolation methods, the "superconvergent" property of patch recovery allows for less resulting interpolation error because the solution error converges faster than expected based on the maximum error in the domain of the boundary value problem.

2.5 Principal Component Analysis of Variability in the Date of Melt Onset

Spatial clusters with similar MOD were identified with Principal Component Analysis (PCA) using analysis in what is referred to as S-mode (Richman 1986), which is used to identify spatial clusters in time series. Here, PCA in S-mode was used on the standardized and mean-centered melt onset field to isolate regions of homogeneous variance in MOD. The principal components of PCA are eigenvectors, which are the linear combinations of the original variables but weighted by their contribution to explaining the variance in each dimension. These components were then linearly transformed, or rotated, using the varimax method (Kaiser 1958), implemented using MATLAB's 'rotatefactors' function. This is an important step for such an application of PCA because rotated components are then less domain-dependent and more localized in space, which helps to draw out physically meaningful clusters (Richman 1986).

To identify regions with similar MOD, each of the resulting 34 components was correlated with the melt onset anomaly field. In 16 of the 18 first components, one region of uniform correlation coefficients with $R^2 > 0.2$ could be identified (Fig. 2.1). For this function of PCA, the strength of the correlation is not nearly as important as the spatial orientation of correlation coefficients. Components 19 to 34 explain less than 20% of the

variance in the melt anomaly field as the components begin to degenerate into primarily statistical noise (i.e. are not physically meaningful; Hwang and Nettleton 2003). Not all northern hemisphere land is incorporated into the subregion due to the nature of PCA, but we sacrifice some areal coverage for accuracy in the development of targeted regions. For example, regions with a strong gradient in MOD due to topography particularly near the coast will not be identified by the PCA algorithm, such as across much of the Rockies and in Greenland and Scandinavia. This limitation was part of the justification for not incorporating the longitudes of the latter in the broader analysis.

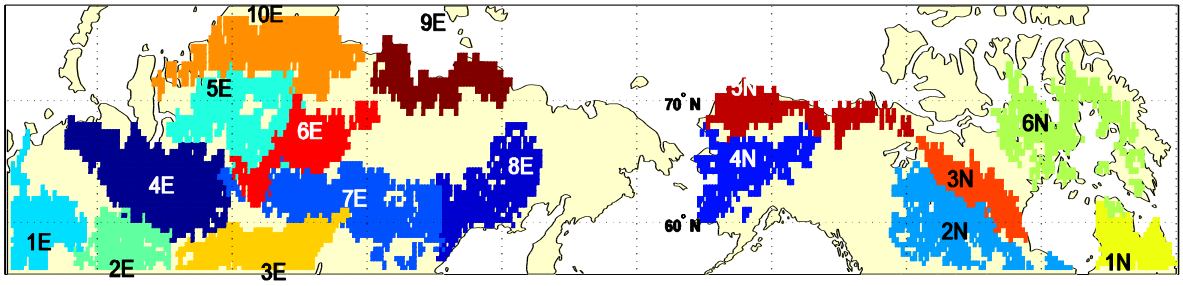

Fig. 2.1) 16 study regions obtained from the first 18 components obtained from S-mode PCA. Eurasian regions are denoted with the "E" prefix while North American regions are denoted with the "N" prefix.

In the 16 regions identified, melt onset timing covaries among the region's grid cells reasonably well through the 34 year period. The MOD does not necessarily occur on the same date within each region every year, but it is likely that these regions respond to the same atmospheric forcing much of the time around the MOD. In many of these regions, there is considerable similarity in topography and landcover. For example, Region 5N aligns well with the Yukon River Valley, 6N covers the tundra of Northeastern Canada and part of the Canadian Archipelago, and 6E represents a significant subset of

the Russian Plain. However, the Urals nearly cut Region 4E in half, and Region 8E overlays part of the Russian Far East with topography dominated by a complex system of mountain ranges, so topography is not always uniform. The extent to which landcover types are homogeneous throughout regions is more likely a function of climate rather than any influence landcover has on MOD, which would manifest in the PCA output. Additionally, dominant snowpack (Sturm et al. 1995) and landcover types are not nearly as important for snow melt onset as they are for the melt dynamics of the ensuing melt season.

2.6 R-mode Principal Component Analysis and Multiple Linear Regression

Multiple linear regression analysis was performed with eight forcing variables encompassing a range of potential melt drivers: downwelling LW, incoming SW, sensible heat fluxes, LW CRE, 2 m temperature, 850 hPa specific humidity, 1000-500 hPa thicknesses, and EC. Anomalies were calculated relative to a fixed day of the year (DOY), i.e. relative to the 34-year mean of the variable for a given DOY. Then, the variable anomalies were averaged over a 1-4 day period prior to MOD such that the averaging period maximized the correlation between the 34-year time series of time-averaged anomalies and melt onset anomalies. Anomalies of Net LW and SW could not be used due to their strong dependency on surface conditions (i.e. whether snow-covered), which strongly influences the relationship between anomalies and MOD timing, so incoming LW and SW were used instead. This is a problem when defining anomalies relative to the day of the year because in some years, the melt season will be

well underway with snow disappearance even possible.

Before regression was conducted, R-mode PCA was done on the eight variables. This type of PCA is the extraction of features from a set of variables such that the dataset is represented by a smaller number of new, orthogonal components (Richman 1986), rather than the S-mode which finds clusters in a spatial field of time series. Each component is often comprised of only one or a few highly correlated variables in the dataset, allowing physical interpretation while reducing dataset dimensionality and multicollinearity. They can then be used to replace the original variables in an analysis such as multiple linear regression, which is done here using MOD anomalies as the dependent variable. We seek to use these distinct "melt schemes" developed by the PCA to explain MOD anomalies through regression. For example, increased water vapor in the atmosphere does not alone drive melt onset in a particular year, but it can do so in coincidence with increased atmospheric thicknesses, surface temperature, LW radiation, and potentially low cloud cover.

Identifying the variables that comprise each PC is done by correlating each component's loading pattern with the field of variables. The loading pattern is itself a correlation matrix, obtained by correlating the original data with each principal component, such that each component has a loading pattern. This second correlation results in a vector of correlation coefficients for each component, but determining the correlation cutoff value for which a variable should be considered to comprise that component is not trivial. This variable selection has been studied extensively (e.g. Cadima and Joliffe 1995; Al-Kandari and Joliffe 2001), and a universal cutoff value is

not recommended (Joliffe 2002). Therefore, we apply an empirical method to determine this cutoff loading by using biserial correlation analysis following Richman and Gong (1999), which locates the point at which the PC loading pattern agrees best with the corresponding signal in the original data. In this analysis, the biserial correlation peaks near a component loading value of 0.45, meaning that variables within each component with a correlation coefficient higher than 0.45 are considered to comprise that component.

A primary advantage of R-mode PCA is the reduction of variables made possible by constructing much of the variance in the data into the first few components. Several methods for component selection criteria in PCA exist (e.g. an overview in Joliffe (2002)); here, we selected the first components that explain more than 90% of the dataset variance. This resulted in retention of the first four components, and rejection of trailing components. In addition to containing redundancy and degenerating into noise, the trailing components have very small variances that generate significant instability (i.e. large confidence intervals) in linear regression coefficients, if they were to be used. Regression analysis proceeded on the retained components using a backward selection linear model, discarding resultant regression coefficients not significant at $\alpha = 0.05$. Because both dependent and independent variables were standardized to run the PCA, the regression coefficients are in standardized units, and can be interpreted as the MOD response (standard deviation of days) to a one standard deviation change in the given component with the remaining components held constant.

2.7 Surface Atmospheric Pressure Analysis

Synoptic conditions at MOD were identified by correlating the S-mode PCA loading pattern corresponding to each region with mean sea level pressure (SLP) averaged between the dates of earliest and latest melt in the given region. This reveals the spatial configuration of SLP during the range of time when snow begins to melt in each region. A positive correlation indicates the tendency for positive SLP anomalies during late melts and/or negative SLP anomalies during early melts, with the opposite true for negative correlations. Wind direction can then be inferred based on the orientation of SLP centers relative to each other. As such, this analysis also provides a physical mechanism for regional variations in EC that are explored further as well. However, this type of analysis does not account for climatologically favored, semi-permanent systems such as the Siberian High and Aleutian Low and their existing effect on wind direction.

2.8 MOD and Forcing Variable Trends and Variability

The mean MOD varies from March across the boreal forest region to early June in the Arctic tundra, with a strong inverse relationship with longitude (in addition to the first-order relationship with latitude) evident on both continents (Fig. 2.2a). MOD variability is largest across southern North America, northwestern Eurasia, and coastal locations. In those regions, the standard deviation exceeds two weeks (Fig. 2.2b), which is roughly consistent with the regions of earliest MOD (Fig. 2.2a). This pattern exhibits larger variation over locations that average earlier MODs, and about half as much variation over northern North America and eastern Eurasia. There are marked differences

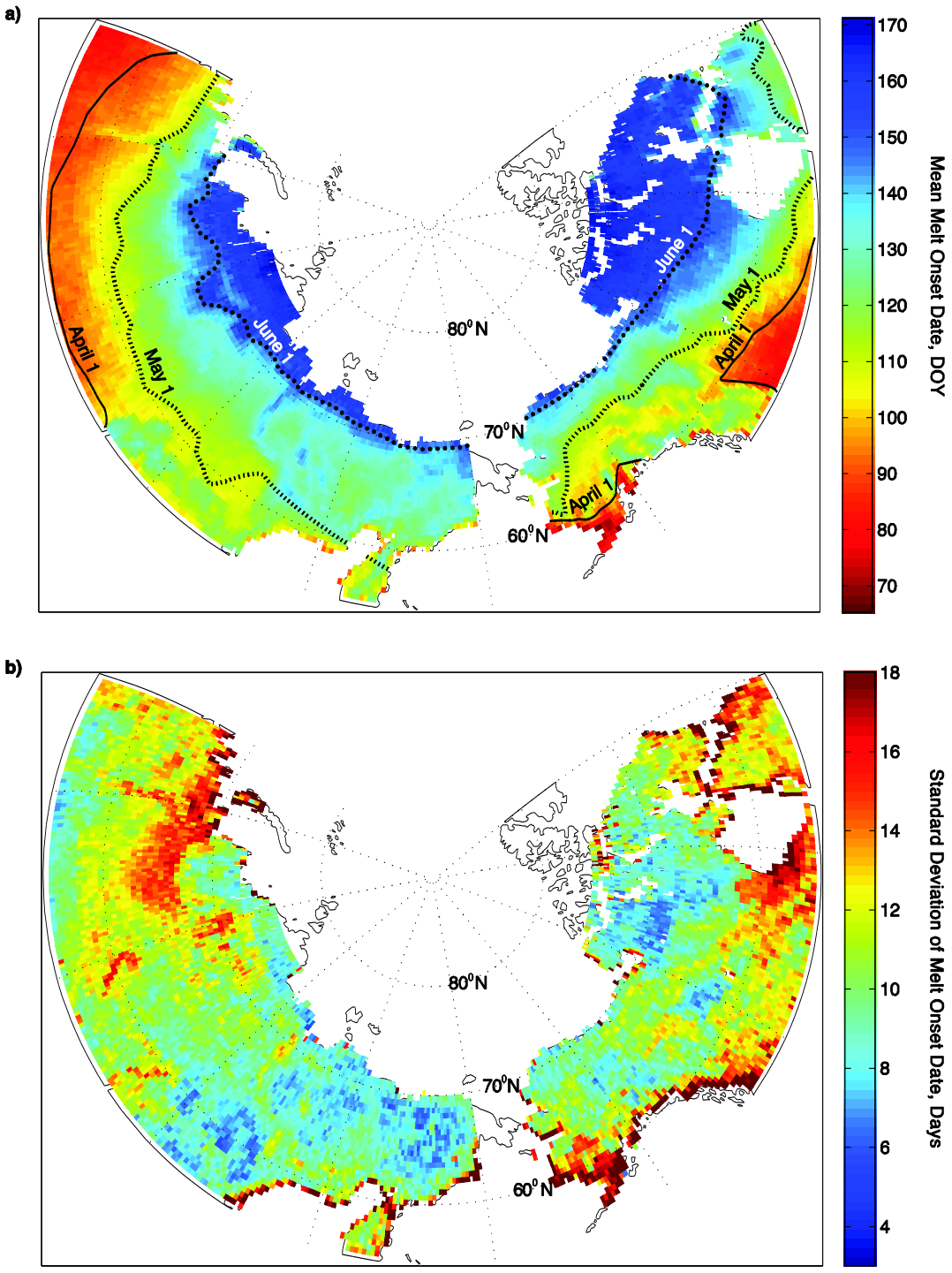

Fig. 2.2) a) 34-year mean and b) standard deviation of MOD. Units are (a) DOY and (b) days.

in spatial patterns of the mean of forcing variables in the 3-day time period prior to and including MOD (Fig. 2.3). The spatial patterns in these means are similar to the pattern in

MOD for several of these variables, including net SW and LW radiation, diurnal and 2 m temperature, and sensible heat fluxes. More surface energy, primarily from radiative fluxes (Fig 2.3a and 2.3b), and warmer temperatures (Fig 2.3h) is available in the northernmost locations where snow begins to melt in May and June. This is primarily due to greater insolation closer to the solstice, with an average of over 150 W m^{-2} more net SW radiation compared to the southern part of the Eurasian and North American regions where melt starts earlier. Additionally, more moisture in the atmosphere on average in these northern regions, shown in 850 hPa specific humidity (Fig. 2.3e), combines with higher atmospheric thicknesses to generate levels of net LW radiation comparable to other regions, which would otherwise be lower due to less energy converging into the atmospheric column. This results in higher 2 m temperatures, but a lower diurnal temperature range due to similar daily maximum temperatures near freezing.

A larger percentage of energy is derived from outside the region than from local radiative fluxes in southern and western regions of North America and Eurasia where snow begins melting earlier in March and April. This is shown in higher levels of EC farther south and west in these regions (Fig. 2.3g) but with lower atmospheric thicknesses (Fig. 2.3d) and specific humidity (Fig 2.3e) leading to lower mean 2 m temperatures (Fig 2.3h). While spatial differences in EC exceed 300 W m^{-2}, only a fraction is available as part of the surface energy balance to melt snow. Some of this energy is radiated out to space or is temporarily stored in the air column, while the remainder heats the column and is thermally radiated to the surface. Finally, regional differences in LW radiation generated by clouds are under 40 W m^{-2} (Fig. 2.3f), although inter-annual differences can exceed 100 W m^{-2} given that years with relatively clear and overcast conditions are

averaged together.

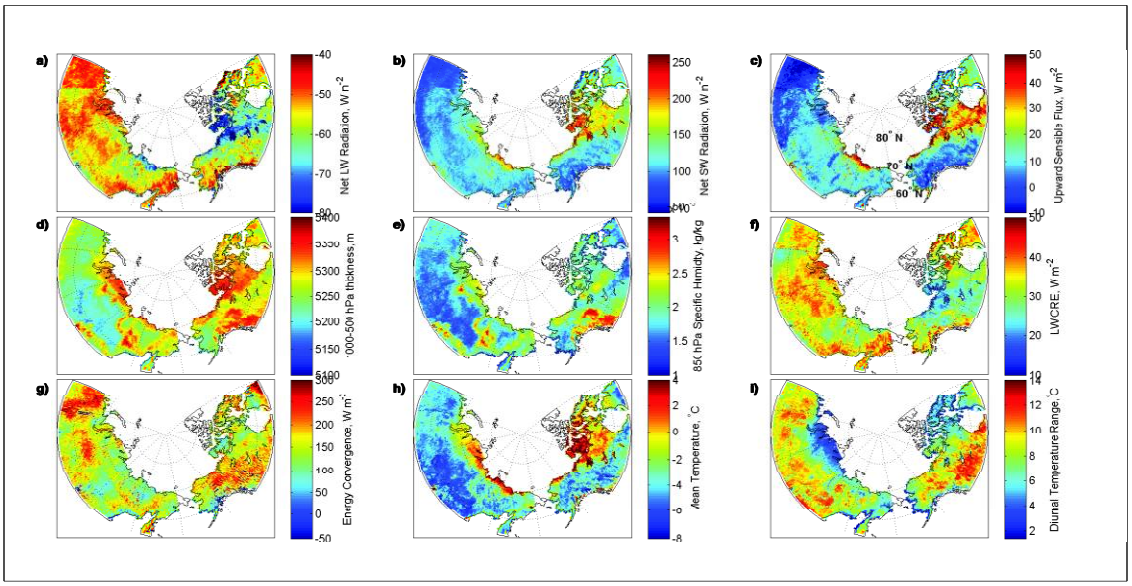

Fig. 2.3) 34-year mean for the 3-day period prior to MOD for a) Net LW radiation b) Net SW radiation c) Sensible heat flux d) 1000-500 hPa thickness e) 850 hPa specific humidity f) LW CRE g) Energy convergence h) Mean 2-m temperature i) Diurnal temperature range.

Most of the strongest trends toward earlier MOD are located across northern regions and are limited to regions 4E-10E, where melt begins 10-15 days sooner (Table 2-1). Across much of the remainder of Eurasia and northern North America, statistically significant (α=0.05) trends suggest that MOD occurs 7-10 days earlier. The southern half of the North American region has no significant MOD trend, and no significant trend toward later MOD was found in any region. Significant trends in forcing variables exist mostly in regions where there are strong trends in MOD (Table 2-1). Because of the strong seasonal cycle of forcing variables, earlier MOD occurs when most forcings (particularly net LW and SW, specific humidity, 1000-500 hPa thickness, and 2 m temperature) have smaller values than at the date of mean melt onset (Fig. 2.4). The only exception is EC, which is higher earlier in the year when the atmosphere acts as more of

Region	Melt Date	Net LW	Sensible Heat	Net SW	1000-500 hPa Thickness	2-m Temp.	LW CRE	EC	850 hPa Humidity	Max. Temp.	850 hPa Temp.	Diurnal Temp.
	Days	W m^{-2}	W m^{-2}	W m^{-2}	m	°C	W m^{-2}	W m^{-2}	g/kg	°C	°C	°C
1E	**-10.53**	-2.05	-1.47	14.15	-34.46	**-2.57**	-2.63	**133.74**	-0.21	**-1.25**	-1.44	**3.18**
2E	**-7.62**	-2.64	-2.34	13.28	**-72.53**	**-3.16**	-0.15	**285.98**	**-0.40**	**-2.37**	**-3.21**	**2.35**
3E	-8.40	-0.26	4.10	17.48	**-69.60**	**-2.48**	2.40	87.22	**-0.44**	**-1.89**	**-2.76**	1.61
4E	**-11.65**	1.57	2.02	24.01	**-53.15**	**-2.24**	0.44	**177.67**	-0.27	**-1.99**	**-1.99**	**1.57**
5E	**-14.69**	1.59	1.40	**24.61**	**-49.91**	**-2.13**	1.58	**95.65**	**-0.30**	**-1.59**	**-2.11**	**0.97**
6E	**-15.77**	1.28	1.82	**23.23**	**-35.52**	**-3.49**	-2.60	**117.10**	**-0.41**	**-1.99**	**-2.43**	**2.58**
7E	**-9.16**	3.35	2.32	**21.51**	**-74.10**	**-3.12**	5.23	68.64	**-0.39**	**-2.40**	**-3.72**	**2.04**
8E	**-11.24**	6.32	-3.18	**26.75**	-27.93	**-1.71**	4.62	37.16	**-0.30**	**-1.41**	**-1.56**	0.39
9E	**-13.83**	-1.22	-9.08	**26.59**	-20.22	**-1.29**	-3.88	12.94	-0.31	-1.37	-1.25	-0.01
10E	**-11.54**	-7.94	4.53	2.65	-33.84	0.11	-5.52	39.31	-0.29	0.23	-1.58	0.42
6N	**-10.32**	**9.93**	**-10.04**	**43.84**	-29.39	**-2.15**	8.70	**90.05**	-0.20	**-3.25**	-1.55	**-1.91**
5N	-7.52	**12.22**	**-15.04**	**37.83**	-1.26	-0.98	7.28	20.76	0.22	**-2.54**	0.35	**-1.76**
4N	-6.22	0.37	-6.61	-7.17	17.31	-0.27	-4.09	**57.43**	-0.18	0.00	0.43	0.42
3N	0.54	-10.21	**22.57**	8.75	-29.88	-1.13	-1.45	-27.63	-0.41	-1.61	**-2.91**	-1.18
2N	-7.38	-4.12	-5.10	-7.67	-3.652	-1.39	**-6.82**	37.57	**-0.39**	-1.43	-0.54	-0.01
1N	-1.87	0.467	-1.07	**-16.53**	-45.29	-1.55	3.15	**65.61**	**-0.37**	-1.31	**-2.27**	-0.70

Table 2-1) 34-year trends in all variables obtained from Sen's Slope. Bolded cells are statistically significant at $\alpha = 0.05$ determined with the Mann-Kendall test. All variables are averaged over the 3-day period centered on MOD.

sink for energy. Thus an earlier shift in MOD results in an increasing trend for EC. However, it is unclear whether increased EC is driving earlier snowmelt, or whether it only appears larger because it tends to be earlier in the spring, and this is investigated further below. Additionally, the lack of a trend in LW radiation in all regions suggests

that these opposing trends between EC and other correlated terms such as atmospheric thicknesses and specific humidity that influence LW are negating each other.

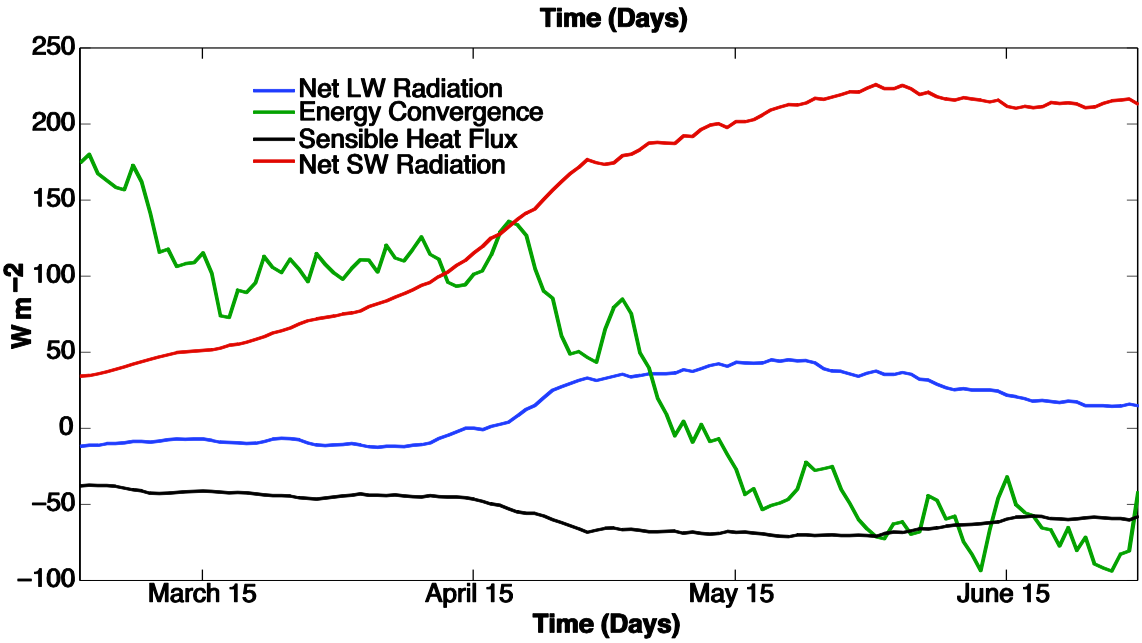

Fig. 2.4) Primary energy balance terms, March 1 – June 30 in region 4E. Data are averaged over the 34-year period.

2.9 Principal Component Regression

Results from the R-mode PCA show that the first principal component is comprised of a combination of LW radiation, specific humidity, 1000-500 hPa thicknesses, and 2 m temperature in most regions, explaining 45-55% of the variance in the data field (Table 2-2). Though more variance is contained in the first component, this only indicates that these variables comprise the most spatially coherent covariance in the data with the trailing components being constrained orthogonally, and they are not necessarily the most important predictor of MOD anomalies. The second component typically describes cloud cover, with LW CRE, incoming SW (of the opposite sign), and sometimes specific humidity exceeding the 0.45 correlation coefficient truncation level. LW radiation often

appears significant in both components because it is highly correlated with humidity water vapor, atmospheric thicknesses, and 2 m temperature, but also has a strong positive and negative correlation with LW CRE and SW radiation, respectively. The third and fourth components are both largely a combination of only sensible fluxes and EC.

Variable	PC 1	PC 2	PC 3	PC 4
Incoming LW	0.358	0.369	0.102	0.088
Specific Humidity	**0.448**	0.211	0.150	0.142
Atmospheric Thicknesses	**0.445**	0.167	0.137	0.204
2 m Temperature	**0.465**	0.110	0.103	0.152
Incoming SW	0.1933	**0.546**	0.151	0.208
LW CRE	0.276	**0.488**	0.116	0.164
Sensible Heat Flux	0.214	0.279	**0.434**	**0.691**
Energy Convergence	0.1761	0.159	**0.741**	**0.477**

Table 2-2) Region-averaged correlation coefficients between each forcing variable and each of the first four principal component loadings. Bolding indicates the dominant variables in each component. The absolute value of the coefficients is taken before regional averaging so that opposing signs do not cancel out, so anticorrelations are not indicated.

The results of the regression show that all regression coefficients for PC 1 are statistically significant, and are consistently some of the largest, with absolute values ranging from 0.33 – 0.47 (Table 2-3). Regression coefficients for PC 2 are generally smaller, but with a positive sign, indicating that anomalously early (late) MODs are correlated with negative (positive) anomalies in cloud cover in most regions. The composition of the first and second components in Regions 9E, 10E, 6N, and 3N is mixed between these two melt schemes (Table 2-3, bold), i.e. both components exhibit a significant correlation with both sets of forcing variables that are otherwise split between these first two components (Table 2-2). Therefore, it is not clear how to interpret those

regression coefficients, and this ambiguity also lowers some of the coefficients in PC 1 and 2. Only one component of PC 3 and 4 is typically significant in the regression, so the regression coefficient that is significant is shown regardless of whether it represents PC 3 or 4. Regression results for this component indicate that positive (negative) EC anomalies explain some early (late) melt variability primarily in regions with earlier mean melt dates, though northern North America is included as well.

Region	PC 1	PC 2	PC 3/4
1E	-0.327	N/S	-0.473
2E	-0.365	0.204	-0.268
3E	-0.389	0.137	-0.397
4E	-0.421	0.222	-0.244
5E	-0.469	0.113	-0.173
6E	-0.456	N/S	-0.329
7E	-0.421	N/S	-0.408
8E	-0.447	N/S	N/S
9E	**0.398**	**0.245**	N/S
10E	**-0.464**	**0.254**	N/S
6N	**-0.257**	**0.347**	-0.21
5N	-0.401	0.177	-0.311
4N	-0.385	0.324	-0.212
3N	**-0.476**	**0.235**	N/S
2N	-0.415	N/S	N/S
1N	-0.423	N/S	-0.267

Table 2-3) Multiple linear regression coefficients for PC 1, PC 2, and PC 3/4 (both are correlated only with sensible heat and energy convergence). Bolding indicates that there is no clear separation between PC 1 and PC 2. N/S is not significant at $\alpha = 0.05$.

2.10 Analysis of Energy Convergence

The influence of EC as a melt driver was explored further by region due to the importance of advection in providing melt energy. EC time series in the week before and after MOD have a very distinct pattern where EC nearly always rises sharply to a peak just prior to MOD before returning to pre-melt levels (Fig. 2.5a). The maximum increase

in its peak in the 3- or 4- day time period before MOD was at least 300 W m^{-2} on average in all regions, with the exception of Regions 2E, 4E and 1N where it increased at between 500 – 600 W m^{-2} (Fig. 2.5b). Similarly, EC peaks at over 300 W m^{-2} in all regions and achieves a peak of over 400 W m^{-2} across some of the earliest melt regions. Regional differences in EC anomalies (relative to fixed DOY as described previously) show the

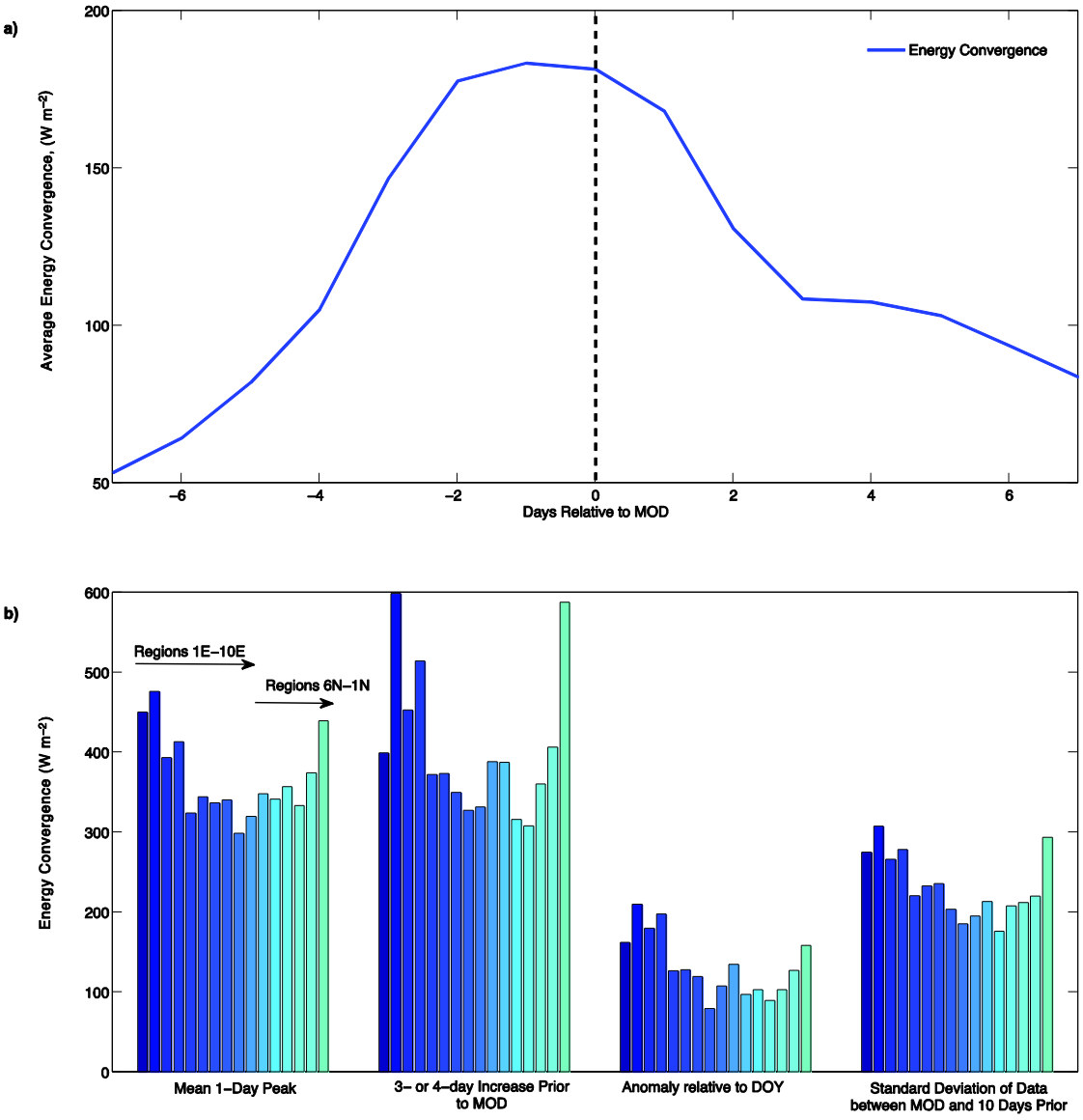

Fig. 2.5) a) Time series of energy convergence within one week of MOD and averaged over the 34-year period over region 4E. b) Measures of 34-year mean energy

convergence by region.

same pattern (Fig. 2.5b), with larger anomalies in regions farther to the south in North America and south and southwest in Eurasia.

The time series of EC prior to MOD shows considerable variability in terms of standard deviation (Fig 2.5b), but differing levels of variability regionally. In earlier melt regions, greater variability in the EC time series exists and manifests as the observed larger increase just prior to MOD (Fig 2.5a), and results in larger EC anomalies. Farther north, EC is greater prior to MOD with a smaller increase, and it follows that EC anomalies are lower here. These results show that regions with an earlier MOD exhibit more variability in EC prior to MOD with a larger increase to a higher peak in the 3-4 days prior to MOD. As a result, EC anomalies are higher here, agreeing with regression results showing EC anomalies explain the most variability in MOD in many of the same regions.

2.11 Surface Pressure Analysis

The correlation between SLP around MOD and S-mode loading patterns provides insight into the regional preference for certain synoptic conditions if they are very different between early and late melts. The spatial configuration of SLP favors flow from the south or southwest during years with early melt onset in many regions such as regions 2E-7E where EC has been shown to be a more significant melt driver (Fig. 2.6). This is demonstrated by positive correlations to the west or northwest of the given region and/or

negative correlations to the southeast or south, indicating the preference for low and high pressure, respectively, during earlier melt years. The opposite interpretation could be constructed for late melt years, though early melt forcing tends to be more anomalous. Additionally, the climatological mean flow (not shown) is from the south and southwest during March and April across southern and western Eurasia, in the same regions as mentioned above, further supporting the greater influence of EC.

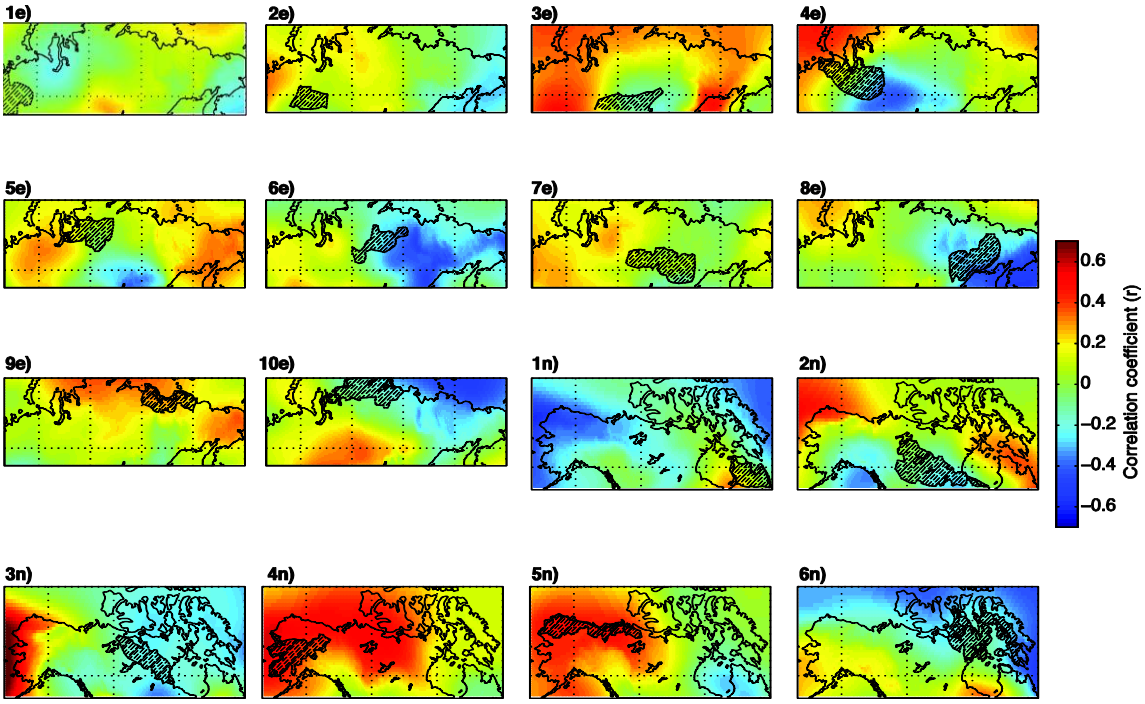

Fig 2.6) Spatial distribution of correlations between each region's component loadings and SLP, which is averaged over the period between a given region's earliest and latest MOD. Each component loading's corresponding region is labeled and indicated by hatching.

The synoptic pattern is unclear across the northernmost regions where there is either little correlation between SLP and MOD, as in Regions 9E and 6N, or a more zonal flow as in Regions 10E and 5N. Regions 2N and 3N in central Canada exhibit a very similar correlation pattern to each other. However, with a large area of anomalous lower

SLP to the northwest during early melts (or higher SLP during late melts), the effect of this SLP configuration on the circulation is unclear; this is too far displaced to be a mode of the Pacific North America Pattern. The general circulation does not appear to favor more energy advection in early melt years (or less in late melt years) in these regions. This supports the conclusion that the temperature increase to the freezing point at MOD occurs through means other than EC.

2.12 Analysis of Cloud Cover

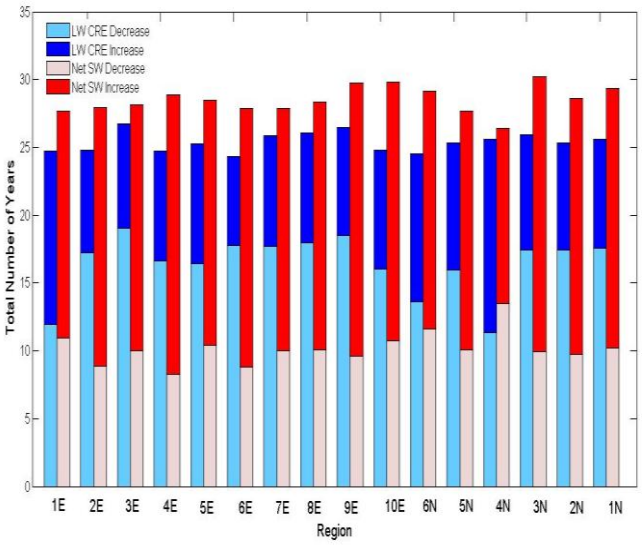

Fig 2.7) Total number of years in each region when LW CRE increased or decreased 10 W m^{-2} in the 3 days prior to MOD (blue), and correspondingly when net SW radiation increased or decreased over 10 W m^{-2} (red). The difference between total years (34) and the height of the stacked bar indicates years when this change did not exceed 10 W m^{-2}.

Due to its ability to significantly alter the surface radiation balance, the influence of clouds was examined in more depth by evaluating the change in LW CRE prior to MOD. LW CRE was found to decrease by at least 10 W m^{-2} approximately twice as often as it increases past that threshold before MOD, with a corresponding increase in net SW

radiation (Fig. 2.7). The exceptions to this are regions 1E, 6N, and 4N where LW CRE increases about as often as it decreases, though these three regions are generally dissimilar otherwise. While the magnitude of change is not directly calculated, this gives an inter-annual cross section of the typical cloud cover conditions rather than averaging LW CRE over the 34-year period. Furthermore, given that the increase in net SW radiation occurs slightly more often than a decrease in LW CRE, it is reasonable to assume that the magnitude of the corresponding increase in SW radiation offsets or exceeds the loss in LW from clouds more often than not.

2.13 Discussion

Multiple linear regression and PCA analysis show that the strongest predictor of early (late) MOD anomalies are positive (negative) anomalies of atmospheric thicknesses, water vapor, and consequently LW radiation and 2 m temperature, and that regional differences in this regression coefficient are small. These four forcing variables comprise PC 1 in all regions except 9-10E, 3N, and 6N, and as such have the strongest covariance between 1979 and 2012. EC has less coherent anomalies and higher frequency variability, and exhibits insignificant correlation with the components until PC3 and PC4 when 65-75% of the data's variance has been accounted for. Positive EC anomalies and sensible heat flux are associated with early MOD anomalies, particularly in southern and western Eurasia. However, EC anomalies do not always correlate well with MOD anomalies, which makes the regression less useful for an analysis of its influence. Nonetheless, PC3/PC4 regression coefficients are largest through southern and western Eurasia as well as western North America where EC anomalies peak immediately prior to

the MOD, whereas coefficients are not significant across northern Eurasia and much of North America.

While much of the analysis of regression coefficients is focused on explaining melt in early melt years, melt onset in late melt years is still initiated by some forcing even if that is the seasonal increase in solar radiation. We hypothesize that this forcing is most likely to be the increased amount of insolation that more readily brings the temperature to the freezing point. Insolation represents a forcing that exists to initiate melt if EC does not do so first because it does not provide a mechanism by itself; its daily increase is minimal. But SW radiation adds over 150 W m^{-2} on average (more in those regions when melt begins later) after accounting for surface reflection, which is a significant contribution to the surface energy balance and the energy available for snow melt. Although there is some increase in net LW radiation throughout the season from higher geopotential heights and water vapor as the general circulation transitions into a warm season regime, the consistent increase in insolation tends to exceed this as shown in Fig. 2.3 (evidence is indirectly based on mean MOD) and Fig. 2.4.

Our conclusion that insolation is more important both in late melt years and in regions where melt begins later is consistent with other research, particularly in contrast with turbulent fluxes. It is generally agreed that turbulent fluxes have a minimal influence in the Arctic and subarctic, with a greater influence in the mid-latitudes and marine locations, while insolation has a much greater effect farther north and with later melts (Leathers and Robinson 1994; Zhang et al. 1997; Ohmura 2001; Liston and Hiemstra 2011; Shi et al. 2013). While we are unable to separate sensible fluxes from EC in the regression coefficients, the magnitude of average sensible fluxes is low, and of positive

sign (directed away from the surface) across much of the study area (Fig. 2.3b). There is larger diurnal variation in this term, so a positive mean value for sensible flux is still likely directed toward the surface for part of the day, but its overall contribution to melt energy is small.

Cloud cover in all regions except 1E, 6N, and 4N decreases prior to MOD in at least two thirds of the years, and this decrease is independent of the magnitude of the MOD onset anomaly. In this study we find that on average, the increase in insolation when clouds disappear compensates for or exceeds the loss of LW radiation, thus neutralizing the energy balance effect. Regression results showing more cloud cover correlating with late melts (Table 2-2) is more due to this decrease rather than a causal relationship with MOD anomalies, since LW CRE anomalies in late melt years tend to be higher relative to the same DOY in other years. The ability of clouds to substantially add LW energy to the surface and initiate melt is well documented (e.g. Zhang et al. 1997; Stone 1997; Stone et al. 2002), and is a factor in some years. However, this study shows that this likely occurs in a minority of years in most of our study regions, and the surface from an energy balance standpoint does not depend on a surge of LW radiation to begin the melt season.

We show that there are large regional differences in EC such that much of the southern part of the entire study area relies more on EC as a melt driver. In these locations, EC is greater, more variable, and more anomalous both in regions where melt begins earlier and in anomalously early melt years. Much of the magnitude in these anomalies is generated only a few days prior to MOD, as shown in Fig. 2.5. Furthermore,

there is a tradeoff between EC and radiative fluxes (primarily SW, as LW is also generated from moist static energy convergence into the column) in terms of what is present at MOD; radiative fluxes play less of role in melt in locations where EC is the dominant driver. There is also considerable zonal asymmetry in meridional energy transport, with poleward transport climatologically occurring at preferred longitudes such as western Siberia and Alaska, with even a net equatorward transport over northeastern Canada. This was calculated across the 70^{th} parallel by Serreze et al. (2007) and attributed to differences in the mean long-wave circulation patterns in the middle troposphere. This explains some of the inconsistency in Fig. 2.6 with other analysis; anomalies in SLP do not need to be strong to facilitate extensive energy transport across southern and western Eurasia where Fig. 2.3 and Fig. 2.5 show EC is strongest.

Our results show that regions that rely more on advective energy exhibit greater inter-annual variability in MOD due to the weekly to monthly duration of prevailing synoptic patterns, whereas regions dominated more by radiative energy should have a more predictable onset date. This is seen in Fig 2.2b, with MOD standard deviations in western Eurasia and southern and eastern North America about twice those in northeastern North America and eastern Eurasia. Lack of advective energy in the latter regions is due to the gradual climatological shift in the circulation pattern limits opportunities for transient eddies to transport heat and moisture poleward.

Trends in MOD and many of the forcing variables differ among groups of regions. There are relatively strong trends toward earlier melt in Regions 1E-7E with corresponding significant increases in EC and decreases in atmospheric thicknesses,

specific humidity, and weaker trends downward in net SW radiation. 2 m temperatures show trends downward by 2-3°C, though some decrease is accounted for in a 1-2°C increase in diurnal temperature range. 850 hPa temperatures also show a 2-3°C trend downward, which precludes the possibility that warm air aloft is still advected into the region to generate LW radiation despite the colder surface temperatures. Therefore, we theorize that the increase in EC compensates for the lower remaining energy balance terms in these regions. This may be a primary forcing behind the earlier melt, but the effect would be the same: with less radiative energy available earlier in the season, the atmosphere naturally acts as more of a sink for energy which manifests as a larger amount of EC. Regardless of the extent to which it is a cause or an effect, we have shown that there is more energy available to converge into the atmospheric column. Additionally, the strong signal for EC as a melt forcing across much of the southern and western Eurasian region is consistent with other studies showing strong correlations with southerly and southwesterly flow bringing warmer and more moist air into primarily western and central Siberia (Ueda et al. 2003; Vicente-Serrano et al. 2007)

In contrast to Regions 1E-7E, forcings driving the strong trends toward earlier melt in Regions 8E to 10E are not possible to identify. In these areas, insolation has a stronger control on MOD, and they are more insulated from anomalous energy transport from the south. EC is constant as MOD shifts to earlier dates, and other variables exhibit weak trends when melt begins in May and early June. Nonetheless, decreasing amounts of net SW radiation here and in many other regions where MOD is arriving earlier suggest there are some broad limits on how anomalously soon MOD could come in a given location. Even earlier spring melts would occur with climatologically less energy

in the atmosphere and especially less from insolation, particularly close to the equinox when insolation changes rapidly. This would require an even larger fraction of energy to come from EC, and there is likely a theoretical limit to how much energy can be transported poleward, so this may limit how much earlier MOD can occur in some places.

In North America outside of Region 6N, MOD trends are not significant, and there are few significant trends in forcing variables. Wang et al. (2013, Fig. 2.2a) shows linear regression-based trends in the same MOD dataset over 33 years on a grid-cell basis over the Northern Hemisphere north of 50°N, which shows significant MOD trends in a sizable minority of Canada and Alaska. This demonstrates that MOD trend differences between continents are not as large as they may appear here due to region selection and regional pixel averaging. It has also been established that the trend in snow disappearance is greater than that in earlier MOD, so there may be a shortening of the melt season in some places, as suggested in Tedesco et al. (2009) who found a shortening of 0.57 day/year across the Arctic due to the difference in trends between these two dates. The explanation for why there are few significant trends in forcing variables over North America is less clear, but changes in spring atmospheric circulation across northern Alaska (Stone et al. 2002) and northern Canada (Brown and Braaten 1998) have been documented. How these changes translate into warmer spring temperatures and earlier melt onset regionally is not a simple problem, and given the vastly different geography of these two continents there may be different mechanisms at work that require further research.

We have found that the predominant snow melt drivers in the Northern

Hemisphere can be broadly split into two categories: those processes involved in energy advection, and those in radiative fluxes. This is unsurprising given the range of latitude, land cover types, continentality, and consequently the more than three month difference in mean MOD. Further, melt drivers shift from advective toward radiative as the MOD occurs closer to the solstice with stronger insolation and weaker synoptic influences. This may account for the weaker variability in MOD in the northernmost regions where this MOD occurs later in May and June.

As snow melt occurs earlier in the spring, the dominant melt drivers may shift more toward advective mechanisms depending on corresponding regional changes in atmospheric circulation. While insolation controls the time period when melt can begin, increased equatorward energy available for transport north will continue to force earlier melting across much of the Northern Hemisphere. Given the regional variation in MOD standard deviation, this shift would likely result in greater variability in each season's MOD. Furthermore, reduction in snow cover at lower latitudes would further enhance energy advection northward, which may already be occurring here demonstrated by a shift toward advective drivers farther north. The impacts of this type of shift in spring snow cover on the rest of the crysphere and boreal climate system remains an uncertainty.

2.14 Conclusions

An assessment of the energy and radiation balance variables driving melt onset across much of the Northern Hemisphere over a 34 year period around the beginning of the snow melt season has led to the following conclusions:

1) The melt onset date has advanced by 1-2 weeks in the 1979-2012 time period

across much of the Northern Hemisphere, with the strongest trends in northern and western Eurasia. In these regions, an increasing amount of advective energy is replacing decreasing levels of many other forcing variables associated with an earlier MOD.

2) Large differences in forcing variables at MOD generally follow the spatial pattern of melt timing, with weaker radiative fluxes and colder mean 2 m temperatures where MOD occurs earlier, though a greater magnitude of energy convergence. This pattern is also found in trends: as MOD comes sooner, there is less energy in the system and more advected from elsewhere.

3) Evidence supports the hypothesis that the date of melt onset is less variable farther north and therefore relies less on EC and more on radiative fluxes (insolation as well as LW radiation generated from higher atmospheric thicknesses and water vapor). Conversely, inter-annual MOD variability is larger farther south in regions that receive more outside energy. This is consistent with MOD synoptic-scale pattern changes that can generate flow from the south and southwest and increased energy advection.

4) Linear regression and PCA analysis show that the strongest predictors of early (late) MOD anomalies are positive (negative) anomalies of atmospheric thicknesses, water vapor, and consequently downward LW radiation and 2 m temperature. Secondary to this, positive (negative) anomalies of EC are associated with early (late) MOD anomalies in many regions and regression coefficients are of similar magnitude to those of the first principal component across southern Eurasia in particular.

5) Regional differences in EC are substantial. Compared to other regions, southern and western Eurasia and southern North America stand out. Here, EC increases more to a higher peak prior to MOD, is more of an anomaly relative to DOY, and is more variable

from day to day. This suggests that EC is a much more important melt driver in these regions than in northern Eurasia and North America.

6) There is little difference regionally in cloud cover at MOD with no significant change over the study period, and often a decrease in cloud cover just prior to MOD.

Snow melt onset across the high latitudes of the terrestrial Northern Hemisphere appears to be controlled by relatively different processes. As snow melt occurs earlier in the spring, the dominant melt drivers may shift more toward advective mechanisms depending on corresponding regional changes in atmospheric circulation. The uncertainty that remains in the observed and future variability of snow melt requires further work to help resolve this. Given the limitations of reanalysis data and the difficulty in separating cause from effect in some of the processes involved in snow melt, it is crucial to continue to address this important component of the changing cryosphere with a variety of methods and perspectives.

References

Abdalati, W., K. Steffen, C. Otto, and K. C. Jezek, 1995: Comparison of brightness temperatures from SSM/I instruments on the DMSP F8 and F11 satellites for Antarctica and the Greenland ice sheet, *Int. J. Remote Sens*., **16**, 1223– 1229, doi:10.1080/01431169508954473.

Aizen, E. M., V. B. Aizen, J. M. Melack, and A. N. Krenke, 2000: Heat exchange during snow ablation in plains and mountains of Eurasia. *J. Geophys. Res.*, **105**, 27,013-27,022.

Al-Kandari, N. M., and I. T. Jolliffe, 2001: Variable Selection and Interpretation of Covariance Principal Components. *Commun. Stat. - Simul. Comput.*, **30**, 339–354, doi:10.1081/SAC-100002371.

Armstrong, R. L., K. W. Knowles, M. J. Brodzik and M. A. Hardman, 1994: updated 2013. DMSP SSM/I-SSMIS Pathfinder Daily EASE-Grid Brightness Temperatures. Boulder, Colorado USA: National Snow and Ice Data Center.

Bamzai, A. S., 2003: Relationship between snow cover variability and Arctic oscillation index on a hierarchy of time scales. *Int. J. Climatol.*, **23**, 131–142, doi:10.1002/joc.854.

Bao, Z., R. Kelly, and R. Wu, 2011: Variability of regional snow cover in spring over western Canada and its relationship to temperature and circulation anomalies. *Int. J. Climatol.*, **31**, 1280–1294, doi:10.1002/joc.2155.

Barnett, T. P., J. C. Adam, and D. P. Lettenmaier, 2005: Potential impacts of a warming climate on water availability in snow-dominated regions. *Nature*, **438**, 303–309, doi:10.1038/nature04141.

Bicheron, P., and coauthors, 2008: GLOBCOVER. [Available online at http://due.esrin.esa.int/globcover/LandCover_V2.2/GLOBCOVER_Products_Description_Validation_Report_I2.1.pdf]

Bosilovich, M. G., F. R. Robertson, and J. Chen, 2011: Global Energy and Water Budgets in MERRA. *J. Clim.*, **24**, 5721–5739, doi:10.1175/2011JCLI4175.1.

Brown, J., Ferrians, O. J., Heginbottom, J. A., Jr., and E. S. Melnikov, 1998, Revised February 2001: Circum-arctic map of permafrost and ground ice conditions. Boulder, CO: National Snow and Ice Data Center/World Data Center for Glaciology, Digital media.

Brown, R., and B. Goodison, 1996: Interannual variability in reconstructed Canadian snow cover, 1915-1992. *J. Clim.*, **9**, 1299–1318.

Brown, R., and R. Braaten, 1998: Spatial and temporal variability of Canadian monthly snow depths, 1946–1995. *Atmosphere-Ocean*, **36**, 37-54, **doi:** 10.1080/07055900.1998.9649605.

Brown, R., C. Derksen, and L. Wang, 2007: Assessment of spring snow cover duration variability over northern Canada from satellite datasets. *Remote Sens. Cryosph. Spec. Issue*, **111**, 367–381.

——, ——, and ——, 2010: A multi-data set analysis of variability and change in Arctic spring snow cover extent, 1967–2008. *J. Geophys. Res.*, **115**, D16111, doi:10.1029/2010JD013975.

Brown, R. D., 2000: Northern Hemisphere Snow Cover Variability and Change, 1915 – 97. *J. Clim.*, **13**, 2339–2355.

Brown, R. D., and D. A. Robinson, 2011: Northern Hemisphere spring snow cover variability and change over 1922–2010 including an assessment of uncertainty. *Cryosph.*, **5**, 219–229, doi:10.5194/tc-5-219-2011.

Cadima, J., and I. T. Jolliffe, 1995: Loading and correlations in the interpretation of principal components. *J. Appl. Stat.*, **22**, 203–214, doi:10.1080/757584614.

Camill, P., 2005: Permafrost thaw accelerates in boreal peatlands during late-20th century climate warming. *Clim.Change*, **68**, 135–152.

Clark, M. P., M. C. Serreze, and D. A. Robinson, 1999: Atmospheric controls on Eurasian snow extent. *Int. J. Climatol.*, **19**, 27–40.

Comiso, J. C., C. L. Parkinson, R. Gersten, and L. Stock, 2008: Accelerated decline in the Arctic sea ice cover. *Geophys. Res. Lett.*, **35**, L01703, doi:10.1029/2007GL031972.

Cullather, R. I., and M. G. Bosilovich, 2012: The Energy Budget of the Polar Atmosphere in MERRA. *J. Clim.*, **25**, 5-24, doi:10.1175/2011JCLI4138.1.

——, and ——, 2011: The Moisture Budget of the Polar Atmosphere in MERRA. *J. Clim.*, **24**, 2861–2879, doi:10.1175/2010JCLI4090.1.

Derksen, C., and R. Brown, 2012: Spring snow cover extent reductions in the 2008–2012 period exceeding climate model projections. *Geophys. Res. Lett.*, **39**, L19504, doi:10.1029/2012GL053387.

Déry, S. J., and R. D. Brown, 2007: Recent Northern Hemisphere snow cover extent trends and implications for the snow-albedo feedback. *Geophys. Res. Lett.*, **34**, L22504, doi:10.1029/2007GL031474.

Dye, D. G., 2002: Variability and trends in the annual snow-cover cycle in Northern Hemisphere land areas. *Hydrol. Process.*, **16**, 3065–3077.

Dyer, J. L., and T. L. Mote, 2006: Spatial variability and trends in observed snow depth over North America. *Geophys. Res. Lett.*, **33**, L16503, doi:10.1029/2006GL027258.

Foster, J. L., D. A. Robinson, D. K. Hall, and T. W. Estilow, 2008: Spring snow melt timing and changes over Arctic lands. *Polar Geography*, **31(3-4)**, 145–157.

Francis, J. A., and S. J. Vavrus, 2012: Evidence linking Arctic amplification to extreme weather in mid-latitudes. *Geophys. Res. Lett.*, **39**, L06801, doi:10.1029/2012GL051000.

Gleason, K. E., A. W. Nolin, and T. R. Roth, 2013: Charred forests increase snowmelt: Effects of burned woody debris and incoming solar radiation on snow ablation. *Geophys. Res. Lett.*, **40**, n/a–n/a, doi:10.1002/grl.50896.

Glen, J. W., and J. G. Paren, 1975: The electrical properties of snow and ice. *J. Glaciol.*, **15**, 15-38.

Groisman, P. Y., T. R. Karl, and R. W. Knight, 1994: Observed impact of snow cover on the heat balance and the rise of continental spring temperatures. *Science*, **263**, 198–200.

Helsel, D. R., and R. M. Hirsch, 2002: Techniques of Water Resources Investigations. *Statistical Methods in Water Resources*, US Geological Survey, p. 522.

Hwang, J., and D. Nettleton, 2003: Principal components regression with data chosen components and related methods. *Technometrics*, **45**, 1–27.

Iijima, Y., K. Masuda, and T. Ohata, 2006: Snow disappearance in Eastern Siberia and its relationship to atmospheric influences. *Int. J. Clim.*, **27**, 169–177, doi:10.1002/joc.

Jezek, K. C., C. J. Merry, and D. J. Cavalieri, 1993: Comparison of SMMR and SSM/I passive microwave data collected over Antarctica. *Ann. Glaciol.*, **17**, 131– 136.

Johannessen, O., and coauthors, 2004: Arctic climate change: Observed and modelled temperature and sea ice variability. *Tellus*, **56**, 328–341.

Jolliffe, I., 2005: *Principal Component Analysis*. 2nd ed. Springer-Verlag, 488 pp.

Kaiser, H., 1958: The Varimax criterion for analytic rotation in factor analysis. *Psykometrika*, **23**, 187-200.

Kapsch, M.-L., R. G. Graversen, and M. Tjernström, 2013: Springtime atmospheric energy transport and the control of Arctic summer sea-ice extent. *Nat. Clim. Chang.*, **3**, 744–748, doi:10.1038/nclimate1884.

Kapsch, M., R. Graversen, T. Economou, and M. Tjernström, 2014: The importance of spring atmospheric conditions for predictions of the Arctic summer sea ice extent. *Geophys. Res*, **41**, 5288–5296, doi:10.1002/2014GL060826.

Kendall, M. G., 1975: *Rank Correlation Measures*. Charles Griffin, London, 202 pp.

Kennedy, A. D., X. Dong, B. Xi, S. Xie, Y. Zhang, and J. Chen, 2011: A Comparison of MERRA and NARR Reanalyses with the DOE ARM SGP Data. *J. Clim.*, **24**, 4541–4557, doi:10.1175/2011JCLI3978.1.

Knowles, Kenneth W., E. G. Njoku, R. L. Armstrong, and M. J. Brodzik., 2002: Nimbus-7 SMMR Pathfinder Daily EASE-Grid Brightness Temperatures. Boulder, Colorado USA: National Snow and Ice Data Center. Digital media.

Leathers, D. J., and D. A. Robinson, 1997: Abrupt Changes in the Seasonal Cycle of North American Snow Cover. *J. Clim.*, **10**, 2569–2585.

Lindsay, R., M. Wensnahan, A. Schweiger, and J. Zhang, 2014: Evaluation of Seven Different Atmospheric Reanalysis Products in the Arctic. *J. Clim.*, **27**, 2588–2606, doi:10.1175/JCLI-D-13-00014.1.

Liston, G. E., and C. A. Hiemstra, 2011: The Changing Cryosphere: Pan-Arctic Snow Trends (1979–2009). *J. Clim.*, **24**, 5691–5712, doi:10.1175/JCLI-D-11-00081.1.

Male, D., and R. Granger, 1981: Snow surface energy exchange: *Water Resour. Res.*, **17**, 609-627.

Mann, H.B., 1945: Nonparametric tests against trend, *Econometrica*, **13**, 245–259.

Marsh, P., P. Bartlett, MacKay, M., S. Pohl, and T. Lantz, 2010: Snowmelt energetics at a shrub tundra site in the western Canadian Arctic. *Hydrol. Process.*, **24**, 3603–3620, doi:10.1002/hyp.7786.

Mioduszewski, J. R., A. K. Rennermalm, D. A. Robinson, and T. L. Mote, 2014: Attribution of snowmelt onset in Northern Canada. *J. Geophys. Res. Atmos.*, **119**, 9638–9653, doi:10.1002/2013JD021024.

Morinaga, Y., S.-F. Tian, and M. Shinoda, 2003: Winter snow anomaly and atmospheric circulation in Mongolia. *Int. J. Climatol.*, **23**, 1627–1636, doi:10.1002/joc.961.

Nijssen, B., G. O'Donnell, A. Hamlet, and D. Lettenmaier, 2001: Hydrologic sensitivity of global rivers to climate change. *Clim. Change*, **50**, 143–175.

Ohmura, A., 2001: Physical Basis for the Temperature-Based Melt-Index Method. *J. Appl. Meteorol.*, **40**, 753–761.

Pomeroy, J., Bewley, D., Essery, R. L. H., Hedstrom, N., Link, T., Granger, R. J., and J.R. Janowicz, 2006: Shrub tundra snowmelt. *Hydrol Process.*, **20**, 923–941, doi:10.1002/hyp.6124.

Post, E., and coauthors, 2009: Ecological dynamics across the Arctic associated with recent climate change. *Science*, **325**, 1355–1358.

Reichle, R. H., R. D. Koster, G. J. M. De Lannoy, B. A. Forman, Q. Liu, S. P. P. Mahanama, and A. Touré, 2011: Assessment and Enhancement of MERRA Land Surface Hydrology Estimates. *J. Clim.*, **24**, 6322–6338, doi:10.1175/JCLI-D-10-05033.1.

Richman, M. B., 1986: Rotation of Principal Components. *J. Clim.*, **6**, 293–335.

——, and X. Gong, 1999: Relationships between the Definition of the Hyperplane Width to the Fidelity of Principal Component Loading Patterns. *J. Clim*, **12**, 1557–1576.

Rienecker, M. M., and Coauthors, 2011: MERRA - NASA's Modern-Era Retrospective Analysis for Research and Applications. *J. Clim.*, **24**, 3624–3648, doi:10.1175/JCLI-D-11-00015.1.

Robertson, F. R., M. G. Bosilovich, J. Chen, and T. L. Miller, 2011: The Effect of Satellite Observing System Changes on MERRA Water and Energy Fluxes. *J. Clim.*, **24**, 5197–5217, doi:10.1175/2011JCLI4227.1.

Rupp, D. E., P. W. Mote, N. L. Bindoff, P. A. Stott, and D. A. Robinson, 2013: Detection and attribution of observed changes in Northern Hemisphere spring snow cover. *J. Clim.*, **26**, 130321123001001, doi:10.1175/JCLI-D-12-00563.1.

Serreze, M. C., and J. A. Francis, 2006: The Arctic Amplification Debate. *Clim. Change*, **76**, 241–264, doi:10.1007/s10584-005-9017-y.

Serreze, M. C., A. P. Barrett, A. G. Slater, M. Steele, J. Zhang, and K. E. Trenberth, 2007: The large-scale energy budget of the Arctic. *J. Geophys. Res.*, **112**, 1–17, doi:10.1029/2006JD008230.

Serreze, M. C., A. P. Barrett, J. C. Stroeve, D. N. Kindig, and M. M. Holland, 2009: The emergence of surface-based Arctic amplification. *Cryosph.*, **3**, 11–19.

Sedlar, J., and A. Devasthale, 2012: Clear-sky thermodynamic and radiative anomalies over a sea ice sensitive region of the Arctic. *J. Geophys. Res. Atmos.*, **117**, n/a–n/a, doi:10.1029/2012JD017754.

Ye, K., R. Wu, and Y. Liu, 2015: Interdecadal change of Eurasian snow, surface temperature and atmospheric circulation in the late 1980s. *J. Geophys. Res.*, **120**, 1–16, doi:10.1002/2015JD023148.

Semmens, K. A., J. Ramage, A. Bartsch, and G. E. Liston, 2013: Early snowmelt events: detection, distribution, and significance in a major sub-arctic watershed, *Environ. Res. Lett.*, **8**, 014020, doi:10.1088/1748-9326/8/1/014020.

Shi, X., P. Y. Groisman, S. J. Déry, and D. P. Lettenmaier, 2011: The role of surface energy fluxes in pan-Arctic snow cover changes. *Environ. Res. Lett.*, **6**, 035204, doi:10.1088/1748-9326/6/3/035204.

——, S. J. Déry, P. Y. Groisman, and D. P. Lettenmaier, 2013: Relationships between Recent Pan-Arctic Snow Cover and Hydroclimate Trends. *J. Clim.*, **26**, 2048–2064, doi:10.1175/JCLI-D-12-00044.1.

Sicart, J., and J. Pomeroy, 2006: Incoming longwave radiation to melting snow: observations, sensitivity and estimation in northern environments. *Hydrol. Process.*, **20**, 3697– 3708, doi:10.1002/ hyp.6383

Stone, R. S., 1997: Variations in western Arctic temperatures in response to cloud radiative and synoptic-scale influences atmosphere. *J. Geophys. Res.*, **102**, 21769–21776.

Stone, R. S., E. G. Dutton, J. M. Harris, D. Longenecker, and W. Irrad, 2002: Earlier spring snowmelt in northern Alaska as an indicator of climate change, *J. Geophys. Res.*, **107**, doi: 10.1029/2000JD000286.

Stroeve, J., J. Maslanik, and L. Xiaoming, 1998: An intercomparison of DMSP F11- and F13-derived sea ice products. *Remote Sens. Environ.*, **64,**132–152, doi:10.1016/S0034-4257(97)00174-0.

Sturm, M., J. Holmgren, and G. E. Liston, 1995: A seasonal snow cover classification system for local to global applications. *J. Clim.*, **8**, 1261–1283.

Takala, M., J. Pulliainen, S. Member, S. J. Metsämäki, and J. T. Koskinen, 2009: Detection of Snowmelt Using Spaceborne Microwave Radiometer Data in Eurasia From 1979 to 2007. *IEEE Trans. Geosci. Remote Sens.*, **47**, 2996–3007.

Tang, Q., X. Zhang, and J. a. Francis, 2014: Extreme summer weather in northern mid-latitudes linked to a vanishing cryosphere. *Nat. Clim. Chang.*, **4**, 45–50, doi:10.1038/nclimate2065.

Tedesco, M., M. Brodzik, R. Armstrong, M. Savoie, and J. Ramage, 2009: Pan arctic terrestrial snowmelt trends (1979–2008) from spaceborne passive microwave data and correlation with the Arctic Oscillation. *Geophys. Res. Lett.*, **36**, 21 doi:10.1029/2009GL039672.

Tong, J., S. Dery, P. Jackson, and C. Derksen, 2010: Testing snow water equivalent retrieval algorithms for passive microwave remote sensing in an alpine watershed of western Canada. *Can. J. Remote Sens.*, **36**, 74–86.

Ueda, H., M. Shinoda, and H. Kamahori, 2003: Spring northward retreat of Eurasian snow cover relevant to seasonal and interannual variations of atmospheric circulation. *Int. J. Climatol.*, **23**, 615–629, doi:10.1002/joc.903

Vicente-Serrano, S. M., M. Grippa, T. Le Toan, and N. Mognard, 2007: Role of atmospheric circulation with respect to the interannual variability in the date of snow cover disappearance over northern latitudes between 1988 and 2003. *J. Geophys. Res.*, **112**, 1–15, doi:10.1029/2005JD006571.

Wang, L., C. Derksen, and R. Brown, 2008: Detection of pan-Arctic terrestrial snowmelt from QuikSCAT, 2000–2005. *Remote Sens. Environ.*, **112**, 3794–3805, doi:10.1016/j.rse.2008.05.017.

Wang, L., C. Derksen, R. Brown, and T. Markus, 2013: Recent changes in pan-Arctic melt onset from satellite passive microwave measurements. *Geophys. Res. Lett.*, **40**, 522-528, doi:10.1002/grl.50098.

Ye, K., R. Wu, and Y. Liu, 2015: Interdecadal change of Eurasian snow, surface temperature and atmospheric circulation in the late 1980s. *J. Geophys. Res.*, **120**, 1–16, doi:10.1002/2015JD023148.

Zienkiewicz, O.C., and J.Z. Zhu, 1992: The superconvergent patch recovery and a posteriori error estimates. Part 1: The recovery technique. *Int. J. Numer. Meth. Engng.*, **33**, 1331-1364.

Zhang, T., S. A. Bowling, and K. Stamnes, 1997: Impact of the atmosphere on surface radiative fluxes and snowmelt in the Arctic and Subarctic. *J. Geophys. Res.*, **102**, 4287, doi:10.1029/96JD02548.

Zhang, T, Stamnes, K., Bowling, S. A., 1996: Impact of Clouds on Surface Radiative Fluxes and Snowmelt in the Arctic and Subarctic. *J. Clim.*, **9**, 2110–2123.

——, 2001: Impact of the Atmospheric Thickness on the Atmospheric Downwelling Longwave Radiation and Snowmelt under Clear-Sky Conditions in the Arctic and Subarctic. *J. Clim.*, **14**, 920–939.

Zib, B. J., X. Dong, B. Xi, and A. Kennedy, 2012: Evaluation and Intercomparison of Cloud Fraction and Radiative Fluxes in Recent Reanalyses over the Arctic Using BSRN Surface Observations. *J. Clim.*, **25**, 2291–2305, doi:10.1175/JCLI-D-11-00147.1.

Zwally, H. J., and P. Gloersen, 1977: Passive microwave images of the polar regions and research applications. *Polar Rec.*, **18**, 431-450.

Chapter 3: Attribution of Snowmelt Onset in Northern Canada

3.1. Introduction

As the Arctic warms, terrestrial spring snow melt has occurred an average of two to four weeks earlier than it did three decades ago (Tedesco et al. 2009). June snow cover extent, largely confined to the Arctic, has decreased nearly twice as fast as the well-publicized September sea ice extent during the satellite era (Derksen and Brown 2012), and nearly 50% since 1967 (Brown et al. 2010). Snow cover across the entire Northern Hemisphere has shown similar earlier snow loss trends responding to warmer temperatures and changes in atmospheric circulation (Dye 2002; Brown 2000; Dery and Brown 2007). This has been less pronounced over North America than Eurasia (Dyer and Mote 2006; Brown and Robinson 2011; Wang et al. 2013), with no trend over the tundra of northern Canada, depending on the data set (Wang et al. 2005). The regional and monthly differences in these trends suggest that melt drivers may exhibit considerable variability, requiring attribution that adequately resolves these differences.

The most important variables controlling snow melt are radiative fluxes, energy advection, turbulent heat fluxes, and the temperature departures that synthesize these (Groisman et al. 1994; Zhang et al. 1997; Aizen et al. 2000; Ohmura 2001; Kapsch et al. 2013; Mioduszewski et al. 2015), but it is unclear whether warmer temperatures primarily drive increased melt, or whether warmer temperatures are a consequence of the earlier melt. It is also uncertain what causes these temperature departures, and temperature departures are not always responsible for earlier melt. Large-scale attribution studies of

spring snow melt have been a challenging undertaking due to the volume of data and its dimensions involved, and tend to provide results constrained by this limitation (Shi et al. 2011; Bamzai 2003; Tedesco et al. 2009; Vicente-Serrano et al. 2006; Shi et al. 2013). Regional studies have largely been confined to central and eastern Eurasia (Aizen et al. 2000; Aizen et al. 2002; Shinoda et al. 2001; Ueda et al. 2003; Iijima et al. 2007; Ye et al. 2015) or western Canada and Alaska (Bao et al. 2011; Semmens et al. 2013). In contrast, small- and point-scale studies of snow melt attribution often have the advantage of utilizing detailed energy balance and turbulent flux data at a high temporal resolution (Sicart et al. 2006; Stone et al. 2002; Pomeroy et al. 2003; Marsh et al. 2010) but can be difficult to generalize beyond the unique geography of the study location and are often limited to one melt season.

Radiation is the primary mechanism providing energy for snow melt. Radiative fluxes have been found to play a larger role in melt energy, especially at high latitudes, with advective energy and resultant sensible heat fluxes contributing more to melt at lower latitudes and earlier in the year (Ohmura 2001; Leathers and Robinson 1997; Zhang et al. 1996, 1997; Liston and Heimstra 2011). The greatest control on downwelling longwave (LW) radiation variability during the melt season, however, is considered to be the change in atmospheric moisture content (Zhang et al. 2001; Kapsch et al. 2014) and temperature (Sedlar and Devasthale 2012), and low cloudcover can raise this radiance by up to 100 W m^{-2} (Stone et al. 2002). Iijima et al. (2007) concluded that atmospheric warming and wetting played the greatest role in eastern Siberian snow ablation, with mean water vapor pressure doubling to 4 hPa in the 30 days before the melt onset date. The impact of clouds on snow melt has been studied extensively (Bintanja and Van den

Broeke 1996; Zhang et al. 1996; Stone et al. 2002; Maksimovich and Vihma 2012), with most concluding that low clouds can be responsible for a large contribution to the net radiation balance and subsequent melt. However, averaged over longer time periods, the additional thermal radiation emitted by increased clouds is nearly balanced by the solar energy they block at these latitudes in spring, and this becomes a net cooling effect as the albedo decreases (Zhang et al. 1996; Dong et al. 2001).

The time period in which snow can begin melting is generally understood to be controlled by insolation, whereas inter-annual variation in this date can be most attributed to variability in downwelling LW radiation (Zhang et al. 2001; Kapsch et al. 2013). Variability in downwelling LW radiation is largely a function of heat and moisture transport changing the mean atmospheric thickness, as well as cloud cover variations. Synoptic conditions that generate the patterns that control energy advection have been studied on a regional and hemispheric scale. There has been some success correlating winter snow conditions and subsequent melt season timing with teleconnections such as the Arctic Oscillation and Pacific North American pattern (Tedesco et al. 2009; Bamzai 2003; Brown 2000), or simply height fields and modes of atmospheric circulation (Vicente-Serrano et al. 2006; Stone et al. 2002; Bao et al. 2011; Ye et al. 2015), but these results depend on the region as well as such methodological considerations as time lags and temporal and spatial averaging. Only few studies explore regional snow melt drivers by analyzing the local energy balance within the larger synoptic perspective, seeking to build on both small- and large-scale research.

Here, the snow melt onset drivers between 2003 and 2011 in northern Canada are characterized and analyzed by using passive microwave radiometer and atmospheric

reanalysis data. This time period was chosen due to the availability of the snow melt dataset. Snow melt onset dates (MOD) were derived from the Advanced Microwave Scanning Radiometer – Earth Observing System (AMSR-E) passive microwave radiometer, while all other data were obtained from Modern Era Retrospective-Analysis for Research and Applications (MERRA), NASA's current state of the art reanalysis product. A range of near-surface energy and atmospheric variables in northern Canada are analyzed at the beginning of the melt season, including 2 m temperature, energy convergence, insolation, specific humidity, and LW cloud radiative effect (CRE). Emphasis is placed on the date of melt onset in three distinct sub regions to isolate the primary regional differences. First, validation of the AMSR-E algorithm with station data is provided, and the spatial variability of melt onset times is shown. This is followed by a comparison of energy balance terms to evaluate the importance of each term relative to each other, and how they differ regionally. Attribution of melt is examined primarily by identifying the number of years in each grid cell when each variable exceeds a predefined threshold to separate the contribution of radiation vs. synoptic influences. Next, composites of 500 hPa height fields are calculated to show the typical synoptic conditions during melt in each region and gain a sense of the large-scale dynamics that drive the local energy balance. Finally, the earliest and latest melt onset occurrences are analyzed to examine if melt drivers are different in extreme snow melt years.

3.2 Study Area

The study region spans 59° to 70° N, 90° to 115° W and is split into three sub regions for much of the analysis (Fig. 3.1). Seasonal temperature patterns and land cover

distribution take on a southwest-northeast orientation, with boreal forest transitioning to tundra (Fig. 3.1). The southwest-northeast orientation of temperature and land cover is likely in part due to the orientation of the Rocky Mountains, which favors a 500 hPa trough near Hudson Bay and a ridge further downstream (Seager et al. 2002). Lake coverage is more extensive moving north and east into the tundra (Fig. 3.1 or refer to Global Lakes and Wetlands Database (Lehner and Doll 2004)), which increases the region's albedo during melt, particularly relative to the boreal forest where snow is removed from dark canopy.

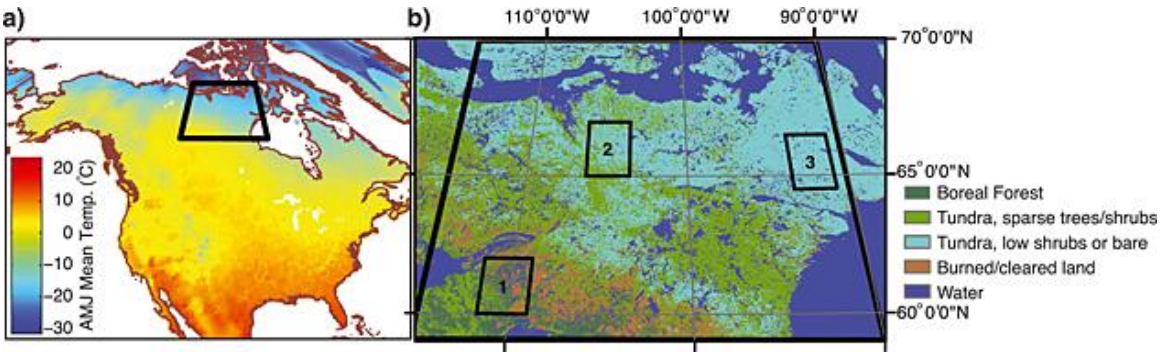

Fig. 3.1) Map of (a) North America showing the study region with mean April–June 2 m temperature (NOAA/NCEP reanalysis) overlaid and (b) land cover map (modified from *Latifovic et al.*, 2002) of the study area with subregions shown in boxes.

3.3 Melt Onset Algorithm

The occurrence of melt in a grid cell was determined using input from a gridded binary (presence/absence) dataset of surface snow melt that incorporates observations from AMSR-E (Knowles 2006) and the National Ice Center's Interactive Multisensor Snow and Ice Mapping System (IMS) product (Ramsay 1998). In this dataset, a grid cell is designated as experiencing surface melt if the diurnal amplitude variation (DAV) (i.e. the absolute value of the brightness temperature difference between the ascending and

descending nodes) exceeds 18 K. The melt identification methodology here is similar to that used in previous studies, which incorporate a minimum DAV criterion and a minimum brightness temperature (Tb) criterion to identify melt (e.g., Ramage et al. 2007). In this study, only the DAV criterion is used because the maximum Tb threshold used for identification of snow-covered surfaces would be mutually exclusive with the minimum Tb to identify melt.

Snow presence prior to melt onset was identified following the approach used in AMSR-E/Aqua L3 Global Snow Water Equivalent product, where snow was indicated with Tb36V $\leq$ 255 K and Tb36H $\leq$ 245 K (Tedesco et al. 2004), and using IMS as a supplement. Gaps due to missing satellite imagery are filled using the previous day's data for up to 5 days. This algorithm was validated in section 4.1 over the 2003-2009 period with Baker Lake (64º N, 96º W) and Yellowknife (62º N, 114º W) snow depth and maximum temperature data, obtained from Environment Canada. These stations are representative of the climate across much of the study region's tundra and boreal forest, respectively.

The MOD between 2003-2011 was determined from the data generated from the above methodology with an algorithm that identifies the date corresponding to the first day of melt in the "primary" melt season without incorporating early melt events, similar to previous studies (e.g. Wang et al. 2013). MOD is specified if surface melt is indicated for either four or more consecutive days, or three consecutive days and at least twice more in the following four days. If melt is not triggered, this condition is relaxed to three consecutive days and one of the following four days. The surface melt product was regridded from its original 25 km grid on Equal-Area Scalable Earth projection to 2/3° x

1/2° to be compatible with MERRA data.

3.4 MERRA Data

Near-surface energy budget and atmospheric variables were obtained from MERRA products (Bosilovich et al. 2011; Cullather and Bosilovich 2011, 2012; Rienecker et al. 2011). Data were obtained for a 108 day period from March 15 – June 30 capturing the melt seasons between 2003 – 2011. All MERRA variables were aggregated from hourly to daily, though diurnal temperature range was derived from hourly 2 m temperature data. MERRA is run on a 1/2° latitude by 2/3° longitude global grid with 72 hybrid-sigma vertical levels to produce analysis at 6-h intervals covering the modern satellite era from 1979 to present. This program is generated with version 5.2.0 of the Goddard Earth Observing System atmospheric model and data assimilation system. It is coupled to the Community Radiative Transfer Model for radiance assimilation, and coupled to a catchment-based hydrologic model and a multilayer snow model for hydrological processes, with the specific goal of improving the representation of water cycle processes in analyses. These fields are forced by the atmospheric model, with inputs assimilated from a wide range of remote sensing (primarily satellite) observations in addition to non-hydrologic surface observations.

MERRA has been evaluated extensively since its release (e.g. Reichle et al. 2011; Robertson et al. 2011; Kennedy et al. 2011; Zib et al. 2012) and evaluated or used in the Arctic (Cullather and Bosilovich 2011, 2012; Liston and Hiemstra 2011). Given MERRA's heavy reliance on satellite data, changes in the observing systems and the evolution of bias correction schemes over more than 30 years poses a challenge to data

integrity. The assimilation of the Special Sensor Microwave Imager in 1987 and Advanced Microwave Sounding Unit in 1998 provided some of the largest continuity challenges, but artifacts associated with their introduction were found to affect energy and moisture budget continuity mostly at lower latitudes and over the ocean (Bosilovich et al. 2011; Robertson et al. 2011). Clouds in MERRA have generally been found to be optically weaker resulting in negative biases in water vapor and downwelling LW radiation (Bosilovich et al. 2011; Kennedy et al. 2011), though a validation of MERRA cloud fraction at two Arctic stations compared more favorably than the four other reanalysis products in the study (Zib et al. 2012). While the melt season can often pose the largest challenge to reanalysis surface fluxes due to rapidly changing albedo (Cullather and Bosilovich 2011), MERRA's energy transport terms do compare favorably (Cullather and Bosilovich 2011) and has validated reasonably well at the surface with some negative flux biases likely due to cloud fraction and cloud properties (Zib et al. 2012). Additionally, many of the largest issues found in MERRA's evaluation do not apply to the variables or levels of the atmosphere used in this study (Kennedy et al. 2011).

Eastern Pacific Oscillation (EPO) index data were obtained from the National Oceanic and Atmospheric Administration's Earth System Research Laboratory. A 3-day moving average is used to calculate the EPO index to filter high frequency variability. The index is not standardized, but 1 standard deviation is approximately 90 dam. The EPO has centers of action of 500 hPa height fields where values from 55 to 65° N, 160 to 125° W are subtracted from values from 20 to 35° N, 160 to 125° W. The positive phase of the EPO manifests itself primarily as a trough in the Gulf of Alaska and a ridge in the

Central Pacific, with a secondary ridge near Hudson Bay. This results in the tendency for warmer air to be advected northward over western Canada into the southwestern part of the study area. While the EPO is a descriptive tool rather than itself a mechanism for initiating the melt season, it is useful in further exploring the large-scale dynamics that control the energy balance when snow begins to melt.

3.5 Attribution Methodology

Five atmospheric variables that best represent the spectrum of potential melt drivers were used in the attribution study of melt onset, including 2 m temperature, total convergence of energy into the atmospheric column, insolation, 850 hPa specific humidity, and LW CRE. LW CRE is the contribution of LW radiation from clouds, and is obtained by subtracting surface-absorbed all-sky LW radiation from surface-absorbed LW radiation assuming a clear sky. Energy convergence is defined in terms of the remaining energy balance terms as

$$-\nabla \cdot \tilde{\vec{F}}A \equiv Rtop + Fsfc - \frac{\partial A_E}{\partial t}$$

where R_{top} is the downward radiative flux at the top of the atmosphere, F_{sfc} is the net surface energy flux (positive upwards), and A_E is the total energy in the atmospheric column. Energy convergence is obtained using a combination of MERRA moist static energy fields following Cullather and Bosilovich (2012, Appendix).

Temperature is generally determined by all the other terms in the energy balance, so it is a useful synthesis of them (Zhang et al. 1997). Other factors influencing MOD that were either not accounted for or were not relevant in this region include elevation

(with associated slope and aspect influences), land cover, rain on snow events, katabatic winds, and turbulent heat fluxes. All turbulent fluxes were omitted in the attribution because their magnitude was found to be too small, generally under 5 W m^{-2} for the daily mean.

Dominant controls on melt onset, i.e. melt attribution, were chosen based on their influence in the above energy balance and to account for the primary mechanisms by which energy is brought to the surface. All of these variables are largely interrelated, so melt can be attributed to more than one driver at once. Anomalies from the 33-year (1979 – 2011) mean were used for the attribution analysis except for LW CRE and energy convergence which used absolute values (Table 3-1). The time series of the 9-year mean of both these variables has a large variance, making their anomalies less meaningful. The averaging interval for each variable in the time period around MOD was chosen to best suit its ability to operate as a melt stimulus, and reduce high-frequency noise when necessary (Table 3-1). For example, cloudcover tends to vary over shorter time scales than energy advection, so both

Melt Driver	Anomaly	Averaging Period
Insolation	Yes	None
LW CRE	No	None
Specific Humidity	Yes	MOD ± 1 day
Temperature	Yes	MOD ± 1 day
Energy Convergence	No	MOD ± 2 days

Table 3-1: Summary of data preparation, indicating for each melt driver whether an anomaly was used in place of absolute values, and over what period (if any) data were averaged. An averaging period of "none" indicates that data only on the MOD were used.

LW CRE and insolation were not averaged beyond daily.

For all variables except energy convergence (see below), a threshold of 50 W m^{-2} was chosen in a physically and empirically (e.g. time series analysis) based assessment of the magnitude necessary to perturb the system enough to initiate melt. For temperature and humidity anomalies, a linear regression was done with downwelling LW radiation anomalies around MOD to determine how much of an increase in these respective variables would result in an increase in 50 W m^{-2} of incoming radiation, on average. The regression was done using only temperature values between -10 °C and 10 °C, the typical range of temperatures near melt onset. The regression results yielded 4 °C for temperature and 1.3 x 10^{-3} kg/kg for specific humidity. The threshold for energy convergence was set at 150 W m^{-2}. In contrast to incoming SW and LW radiation at the surface, energy convergence is used both in heating the atmospheric column (dA_E/dt) and escaping to space (R_{top}). Thus, a conservative estimate of this threshold must be considerably greater than for incoming SW and LW radiation alone. The amount of advected energy reaching the surface varies considerably, but 150 W/m^{-2} was chosen as an estimate with the caveat that the number of years attributed to energy convergence is subject to a higher range of uncertainty. Given these thresholds, the number of years that exceeded them were calculated for each variable and then averaged across each region, hence resulting values for years are not typically whole numbers. To examine the sensitivity of the melt attribution to the magnitudes of the threshold values, the attribution was done with a range of values from 25 – 75 W m^{-2} for the energy balance variables, and 75 to 225 W m^{-2} for energy convergence. This sensitivity study shows that the average change in attributed years for a 10 W m^{-2} (30 W m^{-2} for energy convergence)

change in threshold is generally under 1 year for all melt drivers, with no apparent regional variation in sensitivity (Table 3-2). Sensitivity is slightly higher for energy convergence and LW CRE and lower for specific humidity anomalies, but the difference is not enough to alter conclusions. Thus, this method is suitable to assess regional differences in dominant drivers for melt onset.

Melt Driver	Region 1	Region 2	Region 3
Insolation	0.7	0.92	0.48
LW CRE	0.62	0.76	1.36
Specific Humidity	0.72	0.32	0.6
Temperature	0.24	0.2	0.56
Energy Convergence	0.74	1.06	0.90

Table 3-2: Sensitivity analysis of the attribution analysis to the incoming radiation threshold, performed in the range of 25 – 75 W m^{-2} (75 – 225 W m^{-2} for energy convergence) in each subregion. Units are 1 Yr/10 W m^{-2} (1 Yr/30 W m^{-2} for energy convergence).

3.6 Algorithm Validation and Melt Climatology

Validation of the melt algorithm at Baker Lake and Yellowknife is provided using snow depth and maximum temperature data (Fig. 3.2). In nearly every year, the melt algorithm indicates melt onset within a day of inferred onset (i.e. maximum temperature above freezing accompanied by a decrease in snow depth). 2005 at Baker Lake is the only discrepancy, when the maximum temperature is between 0 ºC and 4 ºC for nearly a week with a large reduction in snow depth before the DAV increases over 18 K, while onset detection at Yellowknife has no such aberrations. The first date when DAV exceeds 18 K is not necessarily the MOD, but becomes a candidate to be such when the onset algorithm is applied to mask early melt events. In a few years at Baker Lake (e.g. 2006),

there is an early melt event that is correctly ignored by the MOD algorithm; the DAV rises above its threshold, but not for enough days to indicate that the primary melt season is underway. In fact, the largest uncertainty in MOD may not be from melt detection methods themselves, but simply in consistently extracting the onset of the primary melt season which can sometimes be relatively indistinct.

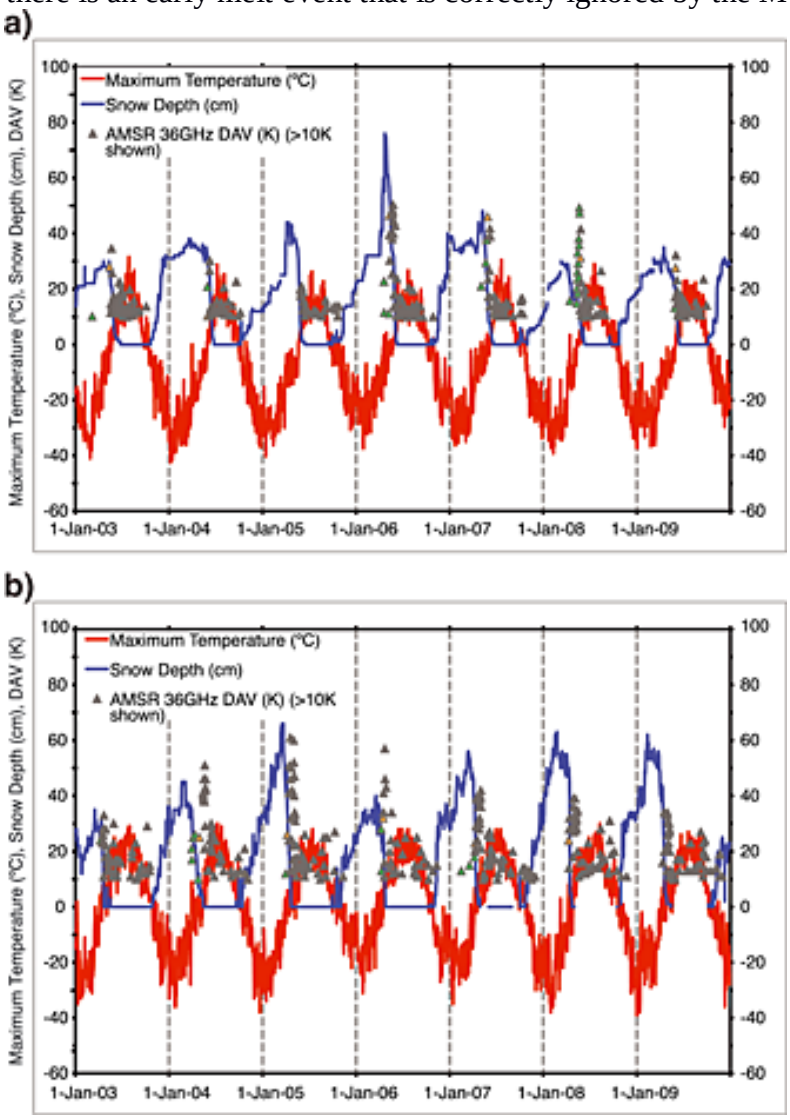

Fig. 3.2) Time series of maximum temperature (°C) and snow depth (cm) with AMSR diurnal amplitude values (K) at the 36 GHz frequency overlaid for 2003–2009 at (a) Baker Lake, NU, and (b) Yellowknife, NT. The MOD is determined by a secondary algorithm, and the marker on this date is colored orange while any days with DAV > 10 K prior to this are colored green. DAV values greater than 10 K are displayed here even though only days when DAV exceeds 18 K are considered candidates for MOD.

Snow melt onset varies strongly over the study area dictated by latitude and longitude (Fig. 3.3). Melt typically begins by April 1 near Region 1 and much of the boreal forest, but not for another two months farther northeast towards Region 3 (Fig. 3.3). Snow cover duration and snow water equivalent

(SWE) have been assessed in other studies, showing a very similar spatial gradient from southwest to northeast (Brown et al. 2007). Wulder et al. (2007) reported mean February SWE values from 80 – 110 mm across the southwestern third of the study area, while this sharply decreased to 40 – 60 mm in the tundra transition zone and less than 30 mm even farther to the northeast. The division of the current study area into three regions is motivated by this spatial distribution of MOD and associated hydrologic terms. A further understanding of the differences in melt season, particularly around MOD, requires an understanding of the energy balance terms at the local scale in the context of the general synoptic pattern during this period.

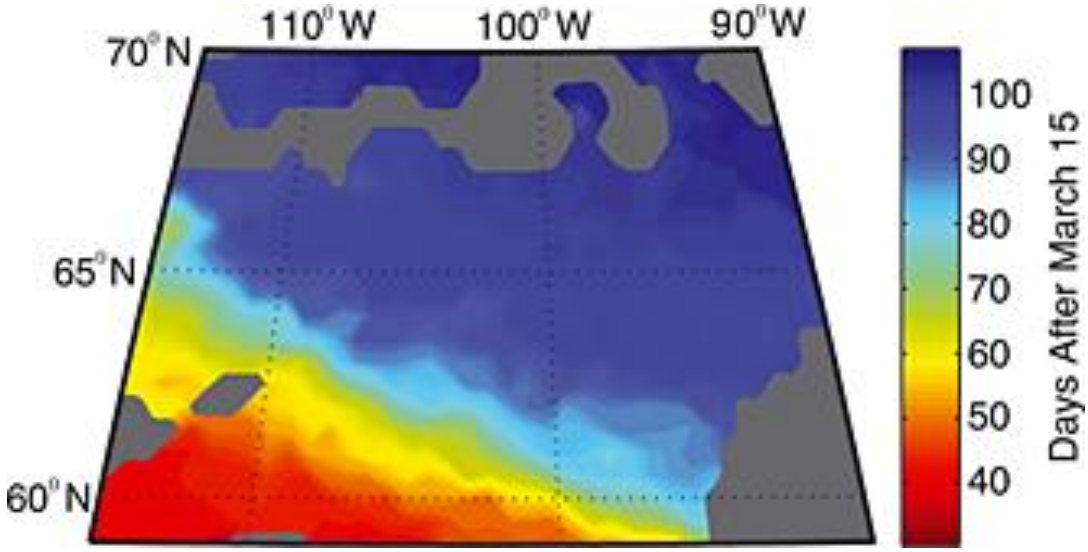

Fig. 3.3) The 2003–2011 mean melt onset date plotted in days after 15 March.

3.7 Energy Balance

Much of the motivation for choosing the location of the three regions comes from the spatial differentiation in energy balance terms. The energy balance in all three regions is dominated by energy convergence, but with growing influence of shortwave (SW)

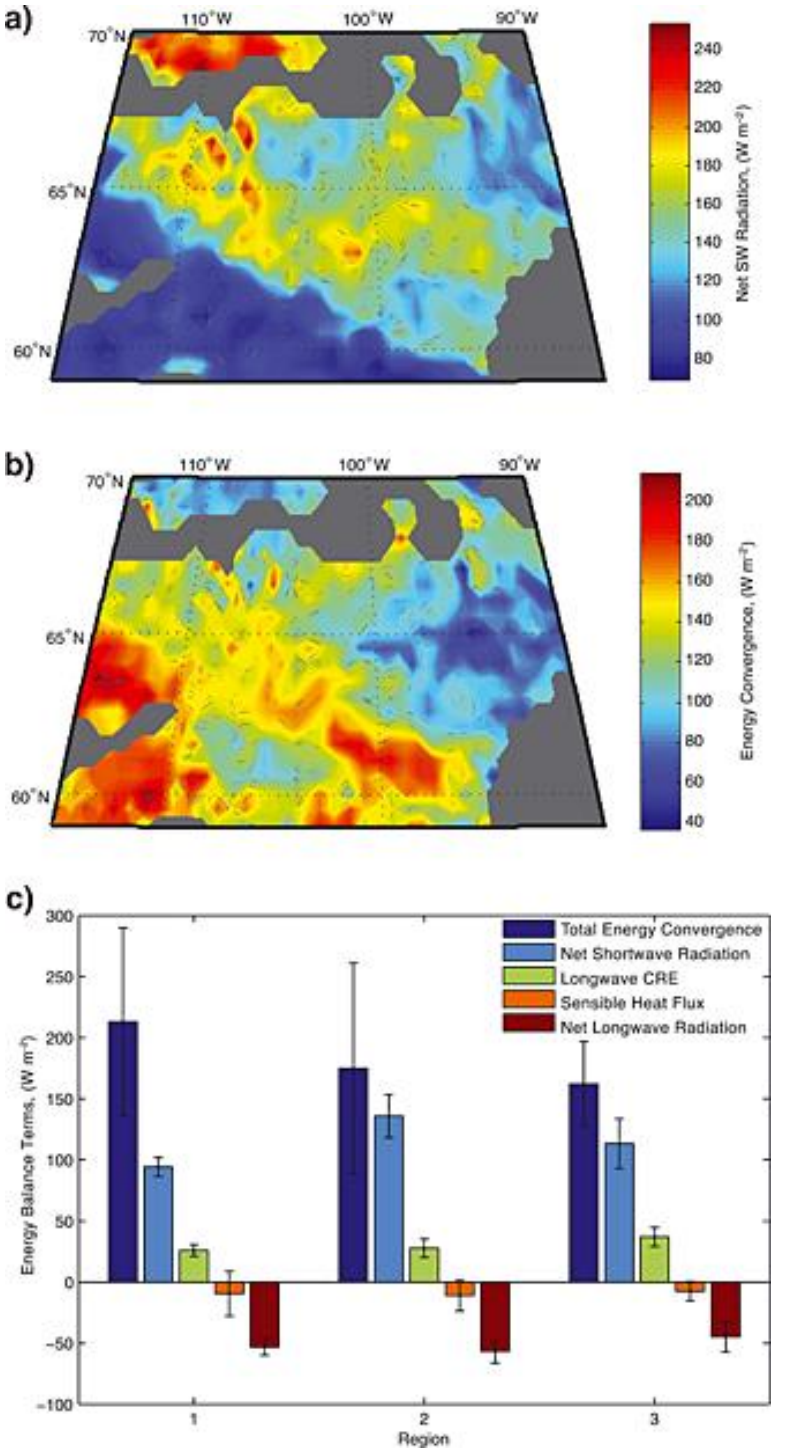

radiation in the northern regions (i.e. Region 2 and 3) (Fig. 3.4). Energy convergence is used as a proxy for the advective energy of air masses, following Aizen et al. (2000). Not all of this energy is available as melt energy at the surface; energy that advects into the atmospheric column both warms the column and is radiated in all directions primarily as LW radiation, including energy lost to space and the downwelling LW radiation considered in this surface energy balance. The energy balance in

Fig. 3.4) (a) Three day mean centered on MOD of 2003–2011 averaged net SW radiation and (b) energy convergence and (c) 2003–2011 mean values of the four primary components of the energy balance and the LW contribution from clouds in each region. A 3 day mean centered on the spatially averaged MOD for each region is used. Error bars are placed at 95% confidence intervals.

Fig. 3.4 is dominated by SW radiation and energy convergence, whereas LW radiation and sensible fluxes are slightly negative (positive upward flux). A positive upward flux in LW radiation indicates that surface emission exceeds atmospheric downwelling of LW radiation. The typical LW contribution from clouds is generally insignificant relative to all incoming LW radiation, which ranges from approximately 220 – 270 W m^{-2} on average.

The largest differences regionally in the energy balance are in SW radiation and energy convergence terms. Region 1 exhibits less SW radiation due to the earlier melt date, but also greater energy convergence, particularly relative to Region 3. There is also evidence for a different split in the net radiation balance between Regions 2 and 3, with slightly more LW radiation and LW CRE but less SW radiation in Region 3 than Region 2. This is consistent with observations of greater cloud cover and atmospheric moisture in Region 3 in the analysis below. Furthermore, downwelling LW radiation does not vary temporally nearly as much as SW radiation because many factors control atmospheric LW emission (e.g. cloud fraction, cloud base height, optical thickness, advected energy, and atmospheric thickness), whereas SW radiation fluctuates to first order only with cloud cover (at a constant latitude and Julian day). Therefore, the effect of cloud cover on the net surface LW radiation over periods of several days is reduced relative to the effect of increased SW radiation in its absence.

3.8 Melt Attribution

Strong regional variation in melt attribution variables around MOD closely follows variation found in the energy balance (Fig. 3.5). Anomalies in insolation can be

considered a melt driver in up to six years of the study period in the area surrounding Region 2, but in only a few years in Region 3 and never southwest of Region 1 (Fig.

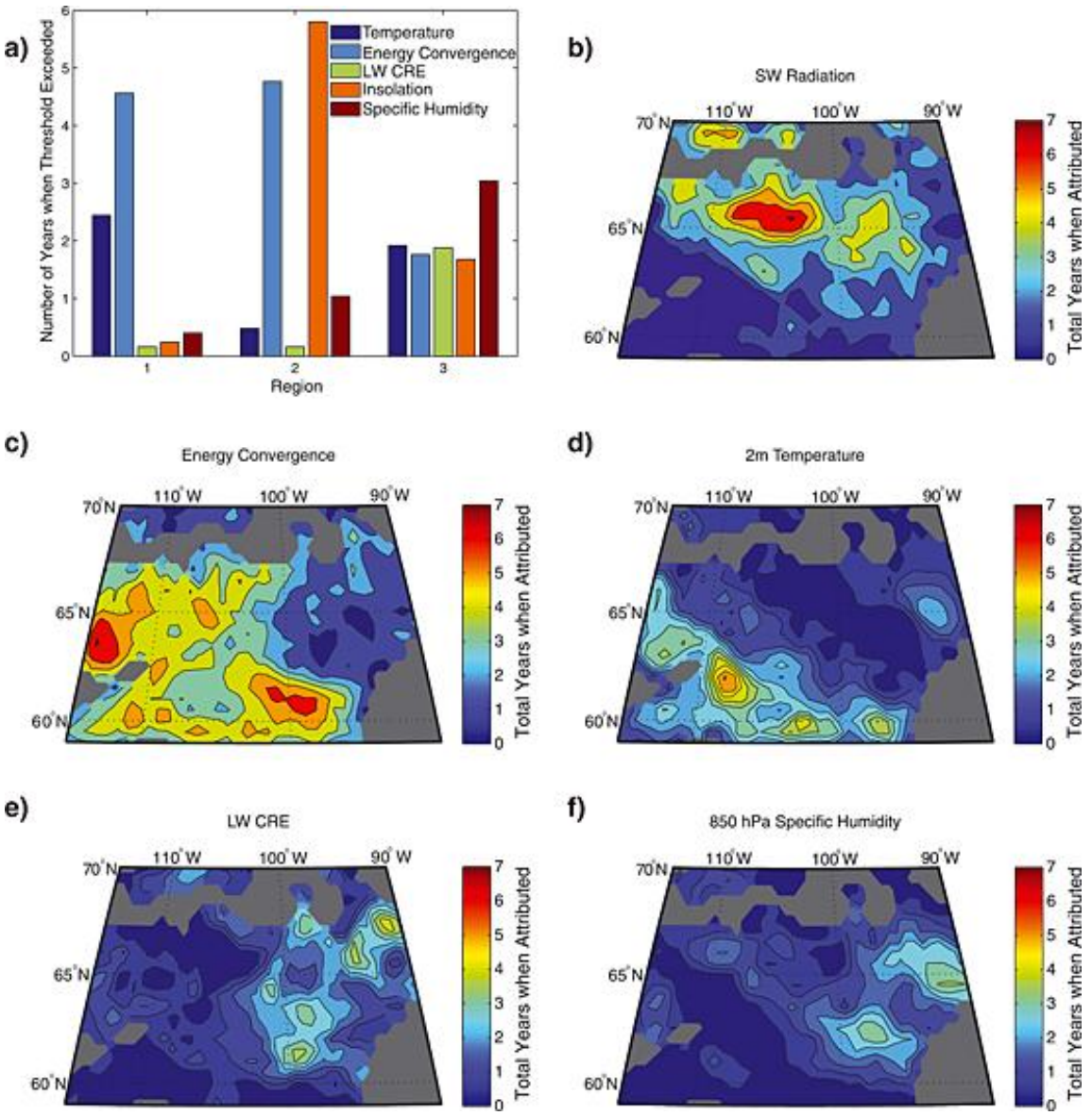

Fig. 3.5) Attribution of melt onset to melt drivers given as the number of years out of nine when the threshold is exceeded for each variable, (a) summarized by region and expressed spatially for (b) insolation anomalies, (c) convergence of total energy, (d) temperature anomalies, (e) LW CRE, and (f) specific humidity anomalies. Attribution threshold is 50 W m^{-2} for LW CRE and insolation, 150 W m^{-2} for energy convergence, 4 C for temperature, and 1.3×10^{-3} kg/kg for specific humidity. Data in map panels are smoothed with a convolution filter.

3.5a). Energy convergence accounted in part for three to six melt onsets in Regions 1 and 2, but for fewer than two in the tundra surrounding Region 3 (Fig. 3.5b). Temperature anomalies exceeded 4 °C in 3-5 melt seasons in the boreal forest, but fewer than two seasons across much of the tundra, particularly around Region 2 (Fig. 3.5c). LW CRE contributed to melt onset in an average of two years in Region 3, but was rarely a factor elsewhere (Fig. 3.5d). Similarly, 850 hPa specific humidity anomalies could be considered a melt driver in about three melt seasons in Region 3 but in one or no melt seasons elsewhere and especially over the boreal forest (Fig. 3.5e). Therefore, melt onset drivers appear to vary regionally, with energy convergence the dominant factor in Region 1, a large contribution from both energy convergence and insolation in Region 2, and mixed drivers in Region 3 with a greater influence from water vapor and clouds but less from energy convergence and insolation (summarized in Fig. 3.5f).

Box plots of attribution terms show the largest regional differences to be in specific humidity anomalies and LW CRE (higher in Region 3 than elsewhere) and insolation (higher in Region 2 than elsewhere) (Fig. 3.6). Energy convergence is generally lower in Region 3, but with high standard deviations in all regions (Fig. 3.6b). Absolute values of LW CRE average only 20 W m^{-2} in Regions 1 and 2, with few values over 50 W m^{-2} anywhere, suggesting the significance of LW CRE as a melt driver may be relatively low (Fig. 3.6c). 850 hPa specific humidity anomalies showed no sign preference in Regions 1 and 2, though the mean of 1 kg/kg in Region 3 is typically enough to increase downwelling LW radiation more than 40 W m^{-2} (Fig. 3.6d). Energy convergence exhibits the largest magnitude and temporal variability, with about half the data ranging between 150 and 250 W m^{-2} in Region 1 compared to 25 to 125 W m^{-2} in

Region 3.

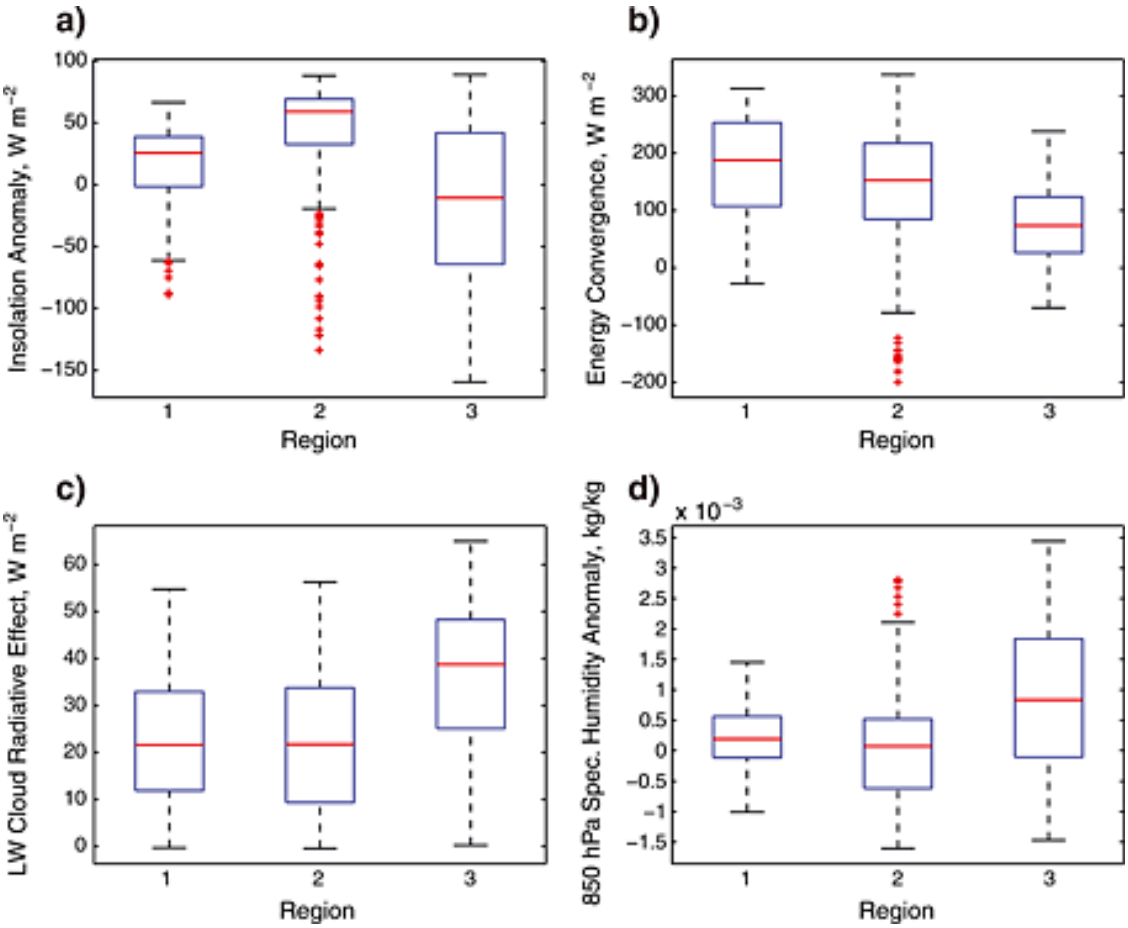

Fig. 3.6) Box plots showing the 25th and 75th percentiles (box), median (red line), range (whiskers), and outliers (crosses) of (a) SW radiation anomalies, (b) convergence of total energy, (c) LW CRE, and (d) 850 hPa specific humidity anomalies.

Temperature at MOD shows some of the largest variation across the entire study region. Daily mean temperature in the 3-day period surrounding MOD (Fig. 3.7a) shows over 10 °C in variation, with daily mean temperatures well below freezing in the southwest corner. The standard deviation of temperature in the broader period surrounding MOD (10 days; melt onset = day 7) in Regions 1, 2, and 3 is 5.2 °C, 2.5 °C, and 3.1 °C, respectively, and the diurnal temperature range (not shown) varies from only 3 – 4 ºC in the northeast corner to over 12 ºC in the boreal forest. It is notable that daily

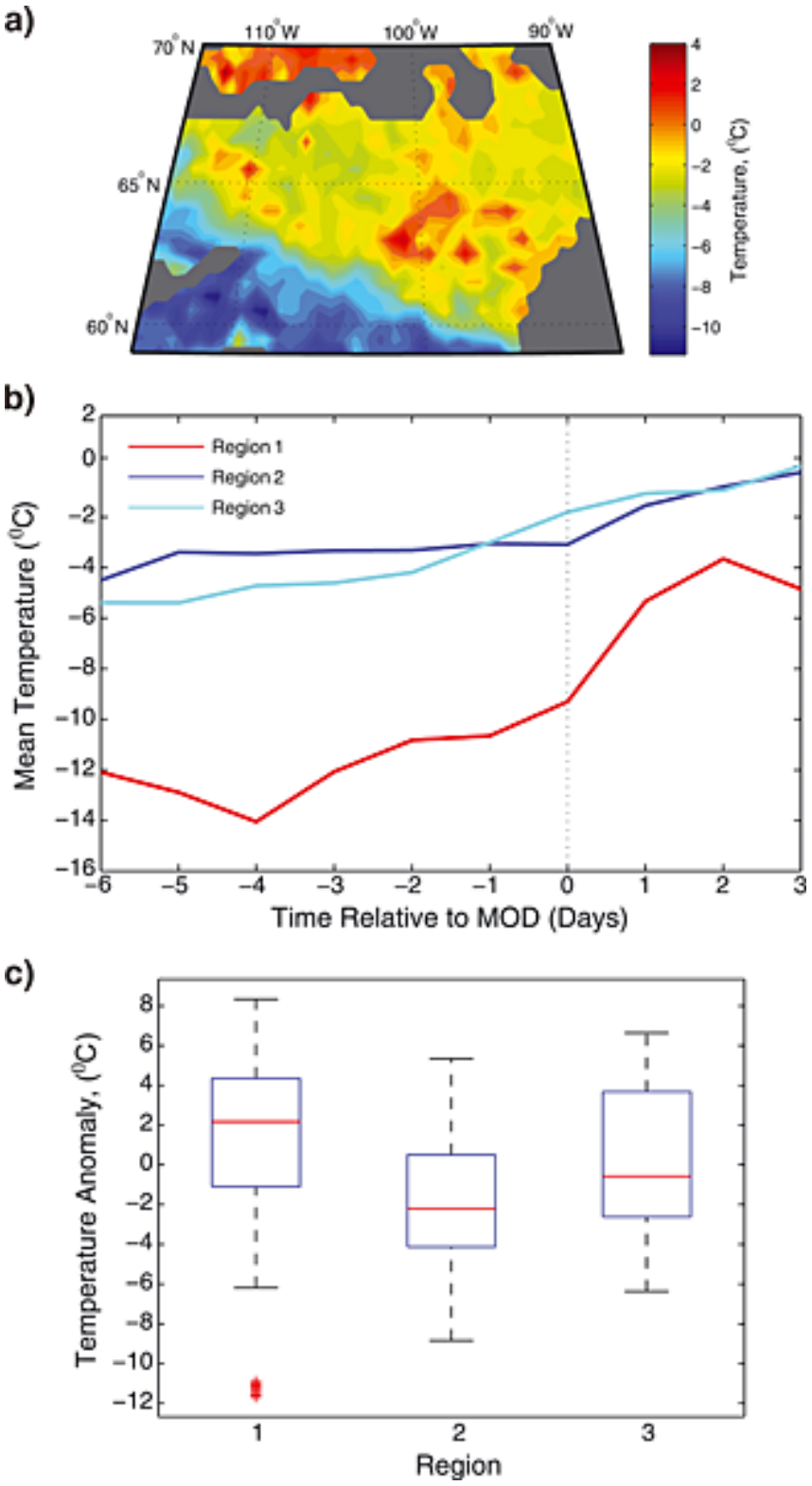

Fig. 3.7) (a) Three day mean of 2 m temperature centered on MOD for each grid cell. (b) Time series of 2003–2011 mean 2 m temperature by region from the week before to the week after MOD. (c) Same as Fig. 3.6 but for temperature anomalies.

means are used for temperature, which explains why melt begins at subzero temperatures. Much of the regional mean temperature difference is a result of differences in the diurnal temperature variation, which is not resolved with daily averages. Finally, mean regional temperatures in the week before and after MOD approaches 0 °C in Regions 2 and 3 with a slight increase of a few degrees during this time, but the lower temperatures in Region 1 increase sharply around MOD (Fig. 3.7b). Temperature anomalies around MOD are typically positive in Region 1, slightly negative in Region 2, and have no favored sign in Region 3 (Fig. 3.7c). However, there is generally no strong bias towards positive temperature anomalies, indicating that temperature anomalies are not a reliable predictor of melt onset across the study area, particularly in Regions 2 and 3.

Results from this section provide support for the following observations: Region 1 is dominated by energy convergence and positive temperature anomalies, while Region 2 is controlled by energy convergence and SW radiation anomalies. Compared to the other regions,melt in Region 3 is more strongly controlled by water vapor anomalies and cloud-derived LW radiation. Diurnal temperature differences as well as those in temperature increase prior to MOD support the idea that melt is initiated by synoptic-scale events that can raise the temperature above freezing for at least a few days around Region 1, whereas the mean temperature farther into the tundra is warmer on average, likely from the greater amount of net radiation, and requires less stimulus to trigger melt onset.

3.9 Synoptic Overview

The three regions have widely different large-scale synoptic regimes shown by composite 500 hPa height anomaly fields and 2 m temperature anomalies at the time of

MOD in each region, though Regions 2 and 3 bear more resemblance to each other than Region 1 (Fig. 3.8). While average MOD in Regions 2 and 3 are very similar, individual years differ more with MOD being at least 1 week apart in 5 years out of 9. The different synoptic regimes help explain observed differences in several variables, particularly energy convergence. In Region 1, height anomalies are more pronounced during melt onset, showing a tendency for an upstream trough over Alaska. Such a trough generates higher heights over Region 1 with corresponding positive meridional wind anomalies advecting warmer air from the south (not shown). Positive 2 m temperature anomalies associated with this composite are 3–5°C (Figs. 3.7c and 3.8a). Regions 2 and 3 (Figs. 438b and 3.8c, respectively) have similar composite 500 hPa height anomaly fields for MOD but

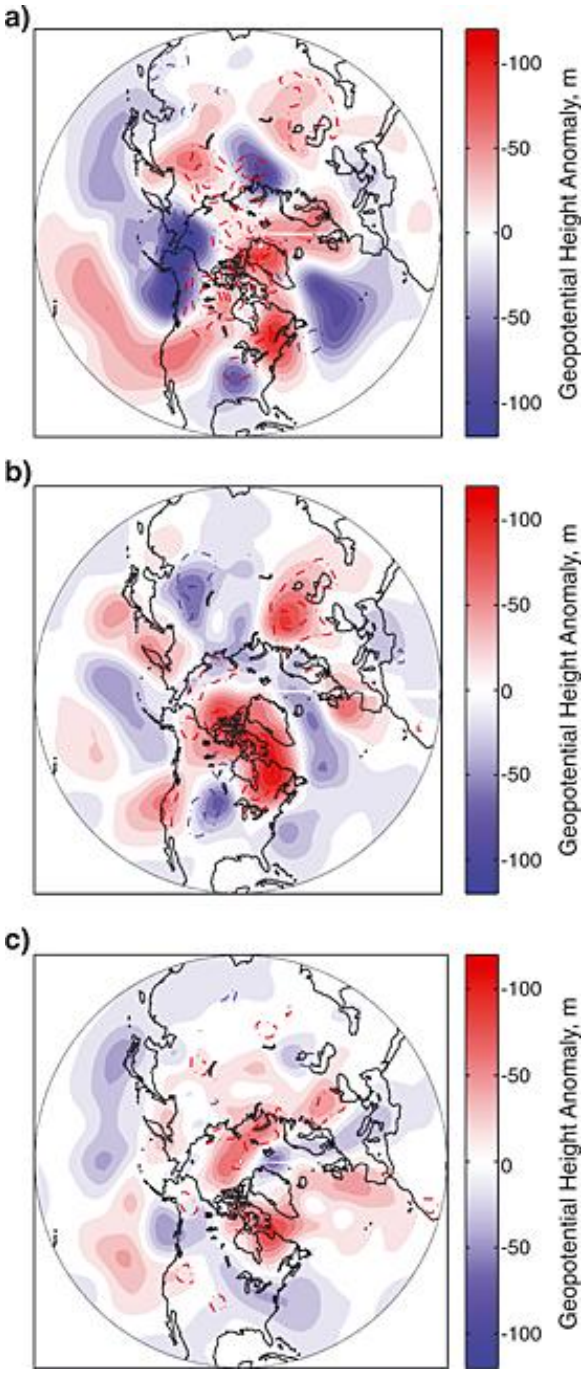

Fig. 3.8) Composite 500 hPa height field anomaly maps from MERRA data at MOD spatially averaged for (a) Region 1, (b) Region 2, and (c) Region 3 each year from 2003 to 2011. Temperature anomalies are shown in dash-dotted lines in increments of 2°C with greater anomalies displayed as thicker lines.

poorly defined synoptic features compared to Region 1. Relative to Region 1, Regions 2 and 3 have small positive height anomalies. In contrast to Region 1, Region 2 and 3's overall synoptic pattern is less conducive for meridional transport of heat, with temperature anomalies showing no sign preference.

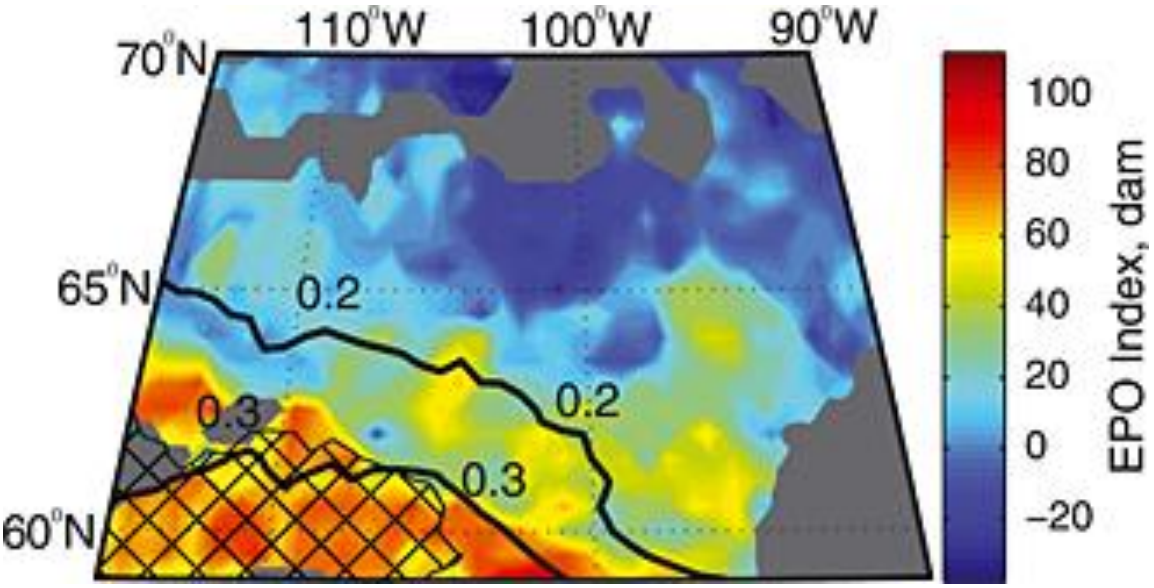

Fig. 3.9) The 2003–2011 mean value of the EPO index at the 2003–2011 mean MOD in each grid cell. The 9 year mean Pearson product-moment correlation coefficient for the 15 March to 30 June time series of 2 m temperature and EPO index (contoured) shows a significant positive correlation across the southwestern part of the area. The hatched region indicates statistically significant correlation at $\alpha = 0.05$.

Some of these dominant synoptic patterns are characteristic of regional modes of low frequency variability (atmospheric teleconnections), and several of these teleconnections were tested for correlation with melt onset drivers. The synoptic pattern in Region 1 corresponds closely with the positive phase of the EPO (Fig. 3.9). The EPO does exhibit some positive correlation over the March 15 – June 30 time period with temperature, LW radiation, and energy convergence. The highest positive correlation averaged over the 9-year period in all these variables occurs in Region 1 where the EPO index is highest during melt (temperature shown in Fig. 3.9). There is no apparent

relationship elsewhere in the study area, farther from the EPO center of action. During years when melt can be attributed to energy convergence, the mean EPO exceeds 1 std (90 m) in approximately the region bounded by the 0.2 correlation contour. Given the patterns in Fig. 3.8, it is very likely that the correlation would be higher if only dates around MOD were used. The short record precluded this, but it is still notable that more than 25% of variance in daily spring temperature from Region 1 to the southwest can be explained by the EPO. No significant correlation with temperature in the study area was found with the other dominant regional teleconnections, including the Arctic Oscillation, North Atlantic Oscillation, and Pacific North America pattern.

3.10 Analysis of Extreme Years

The earliest and latest MOD in each grid cell were obtained, and spatial means of similar atmospheric variables were calculated by region in Fig. 3.10. Because extreme years were determined at the grid cell level, spatial averages in each region incorporate different years in some cases. The largest differences in most variables are differences across the region at MOD rather than differences between extreme years, and these differences are consistent with those found in the attribution analysis. 2 m temperature in Region 1 is 5-10 °C lower than elsewhere, while energy convergence is nearly 50 W m^{-2} higher in Regions 1 and 2 than Region 3. Insolation and consequently net radiation are more than 50 W m^{-2} lower on average in Region 1 than elsewhere as a result of the earlier average melt date.

The greatest difference between early and late melts is in net radiation, derived mostly to more incoming SW radiation during late melts. There is a statistically

significant difference in downwelling LW radiation and humidity in Region 1, with more water vapor in the earliest melts enhancing LW radiated to the surface. Nearly every other variable is unchanged among extreme years, indicating that melt drivers typically remain regionally consistent regardless of when melt begins.

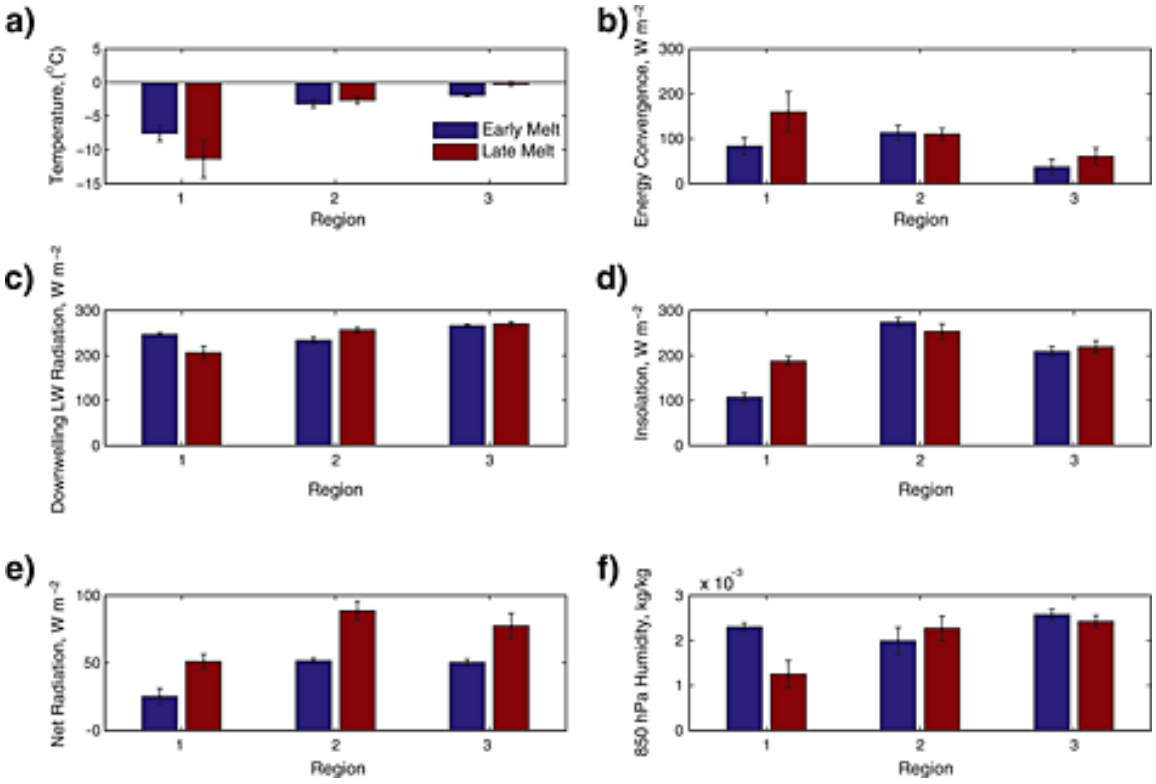

Fig. 3.10) Spatial means and 95% confidence intervals during the year with earliest and latest MOD between 2003 and 2011 of (a) 2 m temperature, (b) energy convergence, (c) downwelling LW radiation, (d) insolation, (e) net radiation, and (f) 850 hPa specific humidity.

3.11 Discussion

In this study we demonstrate large differences in mean MOD in northern Canada, with a spatial pattern exhibiting a southwest-northeast orientation. This matches the mean synoptic pattern with a trough near Hudson Bay, due in part to the topography of the Rocky Mountains and also the sharp boundary between boreal forest and tundra. This

northwest-southeast oriented trough can be seen in 500 hPa height fields (manifested in 2 m temperature in Fig. 3.1a) in all months, and results in large differences in snow melt timing as well as the corresponding energy balance terms across this relatively small region. The proximity to James and Hudson Bay does not appear to influence annual temperature variation, with Conrad's continentality index (Conrad 1946) showing spatially uniform values in the 52-60 range. The large difference in surface land covers is not just a result of the climate, but can strongly influence the spring melt process through its influence on surface albedo. The snow-albedo feedback is much stronger over bare tundra than over the boreal forest, and this feedback is largest when the change in snow cover results in a large change in albedo (Brown 2000). While changes in shrub type and density across the warming Arctic's tundra transition zone can locally generate deeper snow depths and minor changes to the surface energy balance (Sturm et al. 2001), the MERRA resolution is to coarse to capture these changes.

This part of Canada has been of additional interest recently due to some disagreement over spring snow cover duration among satellite data sets. Wang et al. (2005) evaluated the agreement in these data sets over tundra from 66°–74° N, 80°–120° W and concluded that the NOAA weekly snow cover product exhibited a positive snow duration bias likely due to lower data coverage at high latitudes and enhanced cloud cover frequency during May and June, or to mixed pixels in the low resolution IMS product prior to 1999. However, only years prior to the systematic change in this product to a higher resolution, daily, improved computer mapping system in 1999 were studied. Regardless of the cause, there is no reason to assume that there should be a trend toward earlier melt in this region. Here, we have shown that the tundra near Hudson Bay is

climatologically unique and may not respond strongly to enhanced energy advection that may be melting snow sooner elsewhere. The methodological nature and limited time span of this study cannot directly address the issue of data set quality, but could provide further insight given that at least part of the discrepancy among data sets is likely rooted in snow-atmosphere interaction during the melt season. No IMS data are used in this study, but this discord has served as motivation to examine this region of Canada.

Composite 500 hPa anomalies show large differences in the hemispheric pattern during melt onset between Region 1 and Regions 2 and 3. There are stronger height anomalies at this time over Region 1 with a synoptic pattern that supports strong meridional wind anomalies and consequently large positive temperature anomalies. This pattern of height anomalies closely reflects the positive phase of the EPO, with its dominant mode over the North Pacific. This strong EPO signature during MOD in Region 1 underscores the importance of synoptic influences particularly in this area, specifically those with a North Pacific center of action.

Height anomalies are weaker and with a pattern that is less clear overall in Regions 2 and 3, though there is a stronger signal for ridging over Region 2. This is at least partially because these composite dates are later in the spring (late May/early June) when large-scale dynamics aren't as strong when Rossby Waves become shorter and less amplified. Height anomalies over Region 3 show no discernible pattern, and likely are instead a mix of disparate patterns over the 9-year period suggesting that the typical source of melt energy here is more local than a function of the synoptic pattern.

Mean temperatures prior to MOD in Region 1, relative to the remainder of the area, are 1) considerably lower but exhibit a greater increase, 2) more of a positive

anomaly relative to mean temperatures for that Julian day, and 3) more variable on a daily basis given the higher standard deviation and much larger diurnal variation. Higher temperature anomalies are consistent with the lower mean temperatures in Region 1 because anomalies have to be more amplified to reach the freezing point, and this is also supported in Fig. 3.7b where temperature rises more sharply when snow begins to melt.

In Region 1, energy advection is the dominant driver for melt onset shown by both its energy balance magnitude and number of days above the threshold. In contrast, LW CRE and 850 hPa specific humidity anomalies are very low, and SW radiation is not sufficient to generate anomalies on the scale of those in the remainder of the study area. Large temperature anomalies cannot be attributed to increased atmospheric moisture and clouds or greater amounts of SW radiation. Attribution variables and attributed days in Region 2 are similar to Region 1, only differing in mean insolation and temperature. Mean temperature anomalies are negative in Region 2 with strongly positive insolation anomalies, weak mean LW CRE, and neutral 850 hPa specific humidity anomalies. Melt in Region 3 appears to be more influenced by water vapor anomalies and cloud cover, which is also evident in 1000-500 hPa thicknesses and subsequently downwelling LW radiation (not shown), where it tends to be slightly higher than elsewhere. There is also less energy convergence in Region 3, indicating that melt relies less on advected energy and more on local-scale phenomena such as low clouds and local moisture sources. Finally, mean insolation is low relative to Region 2 at approximately the same latitude and Julian day, supporting the hypothesis that more energy here is derived from downwelling LW radiation from clouds and moisture than SW radiation. However, an assessment of mean low cloud fraction at MOD shows no significant difference between

coverage over Regions 2 and 3 (though greater coverage than Region 1), so the observed differences in LW CRE and insolation anomalies may be accounted for by differences in cloud level or optical thickness, and it is possible that the two regions respond to these differently as melt drivers.

Advection of warm and moist air is commonly linked to snow ablation, particularly when there is no snow cover in the source region. Ueda et al. (2003) largely attributed snow ablation to energy advection from southwesterly winds over much of Eurasia, while Aizen et al. (2000) found that ablation in northern Russia was either augmented or delayed by the presence of snow cover to the south, which reduced the advective energy of air masses. Locally, the boundary between snow and bare vegetation (and snow patches at the smallest scale) can generate turbulent heat fluxes that advect melt energy over a snow covered region (Liston 1995; Shook and Gray 1997). This has been found to enhance melt, though these processes are too small-scale to resolve with MERRA data. However, given the sharp boundary between boreal forest and tundra, and the resultant boundary in snow cover that often appears during the spring, it is conceivable that this mechanism commonly operates in this part of the study area, even though its relative significance is unknown.

Analysis of extreme years shows little difference among energy balance terms in the earliest and latest years (aside from SW radiation and its effect on net radiation), with again more of a regional difference supporting some of the conclusions discussed. Iijima et al. (2007) reached similar conclusions in an extreme year analysis at snow disappearance, finding that there was no significant difference between early and late values of surface air temperature, water vapor pressure, and LW radiation terms. While

the sample size here (n = 9) is small, this does provide some evidence that the inter-annual variability in melt date is not dependent on the type of melt stimulus in this region.

3.12 Conclusions

This study analyzed the period of spring snow melt onset between 2003-2011 in a climatologically diverse region of northern Canada west of Hudson Bay. Analysis indicates that there is more energy in the system further northeast by May and June, mostly from increased SW radiation closer to the solstice, but also less energy being advected into the atmosphere. This contrasts with less overall energy and lower temperatures to the southwest, requiring synoptic events and associated energy transport to provide the energy to initiate the primary melt season as well as the more frequent early melt events observed here. This is evident in composite 500 hPa height anomalies that are much more conducive to meridional energy transport. Sources of melt energy vary within the study region, with more energy typically being transported into Regions 1 and 2, a larger proportion from SW radiation in Region 2, and more from LW radiation derived from cloud cover and moisture in Region 3. While there is a greater increase in temperature in Region 1 prior to MOD, the lack of positive bias in temperature anomalies indicates that they are not a reliable predictor for MOD anomalies across the region. Finally, there is little difference in energy balance terms in extreme years, suggesting that the type of melt driver may not control inter-annual variability.

In a warming world with earlier melt onset dates, the results of this study can be

informative in several ways. Snow melt timing will likely respond differently to increased greenhouse gas forcing and Arctic amplification if there are large regional variations in melt drivers. Hemispheric studies addressing this research question should be prepared to downscale analysis to adequately resolve this variability. Additionally, some of these drivers and their associated feedbacks are predicted to change as the high latitudes change, such as atmospheric moisture and cloud cover, and energy advection (Francis and Hunter 2007; Graversen et al. 2009; Lu and Cai 2009; Chen et al. 2011; Ghatak and Miller 2013) while others, such as insolation, will remain constant. Being able to attribute melt onset to those drivers that are changing allows for better long-term prediction of melt season dynamics and the climatological processes influenced by snow cover and its feedbacks. A better understanding of the spring melt process and its sensitivity to a warming Arctic is critical to distributed hydrologic modeling, cryospheric feedback parametrization, and climate dynamics that extend beyond the Arctic into the entire hemisphere.

References

Aizen, E. M., V. B. Aizen, J. M. Melack, and A. N. Krenke (2000), Heat exchange during snow ablation in plains and mountains of Eurasia, *J. Geophys. Res.*, *105*(D22), doi:10.1029/2000JD900279.

Aizen, V., E. Aizen, and J. Melack (2002), Estimation of the energy used to melt snow in the Tien Shan mountains and Japanese Islands, *Global Planet. Change*, *32*, 349–359.

Bamzai, A. S. (2003), Relationship between snow cover variability and Arctic oscillation index on a hierarchy of time scales, *Int. J. Climatol.*, *23*(2), 131–142, doi:10.1002/joc.854.

Bao, Z., R. Kelly, and R. Wu (2011), Variability of regional snow cover in spring over western Canada and its relationship to temperature and circulation anomalies, *Int. J. Climatol.*, *31*(9), 1280–1294, doi:10.1002/joc.2155.

Bintanja, R., and M. R. van den Broeke (1996), The influence of clouds on the radiation budget of ice and snow surfaces in Antartica and Greenland in summer, *Int. J. Climatol.*, *6*(11), 1281–1296.

Bosilovich, M. G., F. R. Robertson, and J. Chen (2011), Global Energy and Water Budgets in MERRA, *J. Clim.*, *24*(22), 5721–5739, doi:10.1175/2011JCLI4175.1.

Brown, R. D. (2000), Northern Hemisphere Snow Cover Variability and Change, 1915 – 97, *J. Clim.*, *13*(1986), 2339–2355.

Brown, R., C. Derksen, and L. Wang (2007), Assessment of spring snow cover duration variability over northern Canada from satellite datasets, *Remote Sens. Environ. Special Issue*, *111*(2-3), 367–381.

Brown, R., C. Derksen, and L. Wang (2010), A multi-data set analysis of variability and change in Arctic spring snow cover extent, 1967–2008, J. Geophys. Res., 115, D16111, doi:10.1029/2010JD013975.

Brown, R. D., and D. A. Robinson (2011), Northern Hemisphere spring snow cover variability and change over 1922–2010 including an assessment of uncertainty, *The Cryosphere*, *5*(1), 219–229, doi:10.5194/tc-5-219-2011.

Chen, Y., J. R. Miller, J. A Francis, and G. L. Russell (2011), Projected regime shift in Arctic cloud and water vapor feedbacks, *Env. Res. Lett.*, *6*(4), 044007, doi:10.1088/1748-9326/6/4/044007.

Conrad, V. (1946), Usual formulas of continentality and their limits of validity. *Trans. Am. Geophys. Union*, 27, 663.

Cullather, R. I., and M. G. Bosilovich (2011), The moisture budget of the Polar atmosphere in MERRA, *J. Clim.*, *24*(11), 2861–2879, doi:10.1175/2010JCLI4090.1.

Cullather, R. I., and M. G. Bosilovich (2012), The energy budget of the Polar atmosphere in MERRA, *J. Clim.*, *25*(1), 110705125533002, doi:10.1175/2011JCLI4138.1.

Derksen, C., and R. Brown (2012), Spring snow cover extent reductions in the 2008–2012 period exceeding climate model projections, *Geophys. Res. Lett.*, *39*(19), 1–6, doi:10.1029/2012GL053387.

Déry, S. J., and R. D. Brown (2007), Recent Northern Hemisphere snow cover extent trends and implications for the snow-albedo feedback, *Geophys. Res. Lett.*, *34*(22), 1–6, doi:10.1029/2007GL031474.

Dong, X., G. G. Mace, P. Minnis, and D. F. Young (2001), Arctic stratus cloud properties and their effect on the surface radiation budget: Selected cases from FIRE ACE, *J. Geophys. Res.*, *106*(D14) 15,297–15,312, doi:10.1029/2000JD900404.

Dye, D. G. (2002), Variability and trends in the annual snow-cover cycle in Northern Hemisphere land areas, *Hydrol. Process.*, *16*(15), 3065–3077.

Dyer, J. L., and T. L. Mote (2006), Spatial variability and trends in observed snow depth over North America, *Geophys. Res. Lett.*, *33*(16), L16503, doi:10.1029/2006GL027258.

Francis, J. A., and E. Hunter (2007), Changes in the fabric of the Arctic's greenhouse blanket, *Environ. Res. Lett.*, 2, 045011.

Ghatak, D., and J. Miller (2013), Implications for Arctic amplification of changes in the strength of the water vapor feedback, *J. Geophys. Res.: Atmos, 118,* doi:10.1002/jgrd.50578.

Graversen, R. G., and M. Wang (2009), Polar amplification in a coupled climate model with locked albedo, *Clim. Dyn.*, *33*(5), 629–643, doi:10.1007/s00382-009-0535-6.

Groisman, P. Y., T. R. Karl, R. W. Knight, G. L. Stenchikov (1994), Changes of snow cover, temperature, and radiative heat balance over the Northern Hemisphere, *J. Clim.*, *7(11)*, 1633–1656.

Iijima, Y., K. Masuda, and T. Ohata (2006), Snow disappearance in Eastern Siberia and its relationship to atmospheric influences, *Int. J. Climatol.*, *27*(2), 169–177, doi:10.1002/joc. 1382.

Kapsch, M.-L., R. G. Graversen, and M. Tjernström, 2013: Springtime atmospheric energy transport and the control of Arctic summer sea-ice extent. *Nat. Clim. Chang.*, **3**, 744–748, doi:10.1038/nclimate1884.

Kapsch, M., R. Graversen, T. Economou, and M. Tjernström, 2014: The importance of spring atmospheric conditions for predictions of the Arctic summer sea ice extent. *Geophys. Res*, **41**, 5288–5296, doi:10.1002/2014GL060826.

Kennedy, A. D., X. Dong, B. Xi, S. Xie, Y. Zhang, and J. Chen (2011), A Comparison of MERRA and NARR Reanalyses with the DOE ARM SGP Data, *J. Clim.*, *24*(17), 4541–4557, doi:10.1175/2011JCLI3978.1.

Knowles, K. 2006. *AMSR-E/Aqua Daily EASE-Grid Brightness Temperatures* (Northern Hemisphere). Boulder, Colorado USA: NASA DAAC at the National Snow and Ice Data Center.

Latifovic, R, Z. Zhi-Liang, J. Cihlar, and C. Giri (2002). Land cover of North America

2000, Natural Resources Canada, Canada Center for Remote Sensing, US Geological Service EROS Data Center.

Leathers, D. J., and D. A. Robinson (1997), Abrupt Changes in the Seasonal Cycle of North American Snow Cover, *J. Clim.*, *10*(10), 2569–2585.

Liston, G. (1995), Local advection of momentum, heat, and moisture during the melt of patchy snow covers, *J. Appl. Meterol. 34*(7).

Liston, G. E., and C. A. Hiemstra (2011), The Changing Cryosphere: Pan-Arctic Snow Trends (1979–2009), *J. Clim.*, *24*(21), 5691–5712, doi:10.1175/JCLI-D-11-00081.1.

Lu, J., and M. Cai (2009), Seasonality of polar surface warming amplification in climate simulations, *Geophys. Res. Lett.*, *36*(16), L16704, doi:10.1029/2009GL040133.

Maksimovich, E., and T. Vihma, 2012: The effect of surface heat fluxes on interannual variability in the spring onset of snow melt in the central Arctic Ocean. *J. Geophys. Res.*, **117**, 1–19, doi:10.1029/2011JC007220.

Marsh, P., P. Bartlett, and M. MacKay (2010), Snowmelt energetics at a shrub tundra site in the western Canadian Arctic, *Hydrol. Process. 3620*(July), 3603–3620, doi:10.1002/hyp.7786.

Mioduszewski, J.R., A.K. Rennermalm, D.A. Robinson, and L. Wang, 2015: Controls on Spatial and Temporal Variability in Northern Hemisphere Terrestrial Snow Melt Timing, 1979–2012. *J. Clim.*, **28**, 2136–2153, doi:10.1175/JCLI-D-14-00558.1.

Ohmura, A. (2001), Physical Basis for the Temperature-Based Melt-Index Method, *J. Appl. Meteorol.*, *40*(4), 753-761.

Pomeroy, J., and B. Toth (2003), Variation in surface energetics during snowmelt in a subarctic mountain catchment, *J. Hydrometeorl.*, *4*(4), 702–719.

Ramage, J. M., J. D. Apgar, R. A. Mckenney, and W. Hanna (2007), Spatial variability of snowmelt timing from AMSR-E and SSM / I passive microwave sensors, Pelly River, Yukon Territory, Canada, *21*, 1548–1560, doi:10.1002/hyp.6717.

Ramsay, B. (1998), The interactive multisensory snow and ice mapping system, *Hydrol Processes, 12*, 1537-1546.

Reichle, R. H., R. D. Koster, G. J. M. De Lannoy, B. a. Forman, Q. Liu, S. P. P. Mahanama, and A. Touré (2011), Assessment and Enhancement of MERRA Land Surface Hydrology Estimates, *J. Clim.*, *24*(24), 6322–6338, doi:10.1175/JCLI-D-10-05033.1.

Rienecker, M. M. et al. (2011), MERRA - NASA's Modern-Era Retrospective Analysis for Research and Applications, *J. Clim.*, *24*(14), doi:10.1175/JCLI-D-11-00015.1.

Robertson, F. R., M. G. Bosilovich, J. Chen, and T. L. Miller (2011), The Effect of Satellite Observing System Changes on MERRA Water and Energy Fluxes, *J. Clim.*, *24*(20), 5197–5217, doi:10.1175/2011JCLI4227.1.

Seager, R., D. S. Battisti, J. Yin, N. Gordon, N. Naik, a. C. Clement, and M. a. Cane (2002), Is the Gulf Stream responsible for Europe's mild winters?, *Q. J. Roy.*

Meteor. Soc., *128*(586), 2563–2586, doi:10.1256/qj.01.128.

Sedlar, J., and A. Devasthale, 2012: Clear-sky thermodynamic and radiative anomalies over a sea ice sensitive region of the Arctic. *J. Geophys. Res. Atmos.*, **117**, n/a–n/a, doi:10.1029/2012JD017754.

Semmens, K. A., J. Ramage, A. Bartsch, and G. E. Liston (2013), Early snowmelt events: detection, distribution, and significance in a major sub-arctic watershed, *Environ. Res. Lett.*, *8*(1), 014020, doi:10.1088/1748-9326/8/1/014020.

Shi, X.,, P Groisman, S. Dery, and D. Lettenmaier (2011), The role of surface energy fluxes in pan-Arctic snow cover changes. *Env. Res. Lett.*, 6, doi:10.1088/1748-9326/6/3/035204.

Shi, X., S. J. Déry, P. Y. Groisman, and D. P. Lettenmaier, 2013: Relationships between Recent Pan-Arctic Snow Cover and Hydroclimate Trends. *J. Clim.*, **26**, 2048–2064, doi:10.1175/JCLI-D-12-00044.1.

Shinoda, M., H. Utsugi, and W. Morishima (2001), Spring snow-disappearance timing and its possible influence on temperature fields over central Eurasia, *J. Meteorol. Soc. Jpn.*, *79*(1), 37–59.

Shook, K., and D. Gray (1997), Snowmelt resulting from advection, *Hydrol. Process.*, *11*, 1725–1736.

Sicart, J., and J. Pomeroy (2006), Incoming longwave radiation to melting snow: observations, sensitivity and estimation in northern environments, *Hydrol. Processes*, *3708*, 3697– 3708, doi:10.1002/hyp.6383.

Stone, R. S., E. G. Dutton, J. M. Harris, D. Longenecker, and W. Irrad (2002), Earlier spring snowmelt in northern Alaska as an indicator of climate change, *J. Geophys. Res.*, *107*(D10), doi: 10.1029/2000JD000286.

Sturm, M., J. P. McFadden, G. E. Liston, F. S. Chapin III, C. H. Racine, and J. Holmgren (2001), Snow – shrub interactions in Arctic tundra : A hypothesis with climatic implications, *J. Clim.*, *14*, 336–344.

Tedesco, M., R. Kelly, J. L. Foster, and A. T.C. Chang. 2004. AMSR-E/Aqua Daily L3 Global Snow Water Equivalent EASE-Grids. Version 2. Boulder, Colorado USA: NASA DAAC at the National Snow and Ice Data Center.

Tedesco, M., M. Brodzik, R. Armstrong, M. Savoie, and J. Ramage (2009), Pan arctic terrestrial snowmelt trends (1979–2008) from spaceborne passive microwave data and correlation with the Arctic Oscillation, *Geophys. Res. Lett.*, *36*(21), 1–6, doi:10.1029/2009GL039672.

Ueda, H., M. Shinoda, and H. Kamahori (2003), Spring northward retreat of Eurasian snow cover relevant to seasonal and interannual variations of atmospheric circulation, *Int. J.Climatol.*, *23*(6), 615–629, doi:10.1002/joc.903.

Vicente-Serrano, S. M., M. Grippa, T. Le Toan, and N. Mognard (2007), Role of atmospheric circulation with respect to the interannual variability in the date of snow

cover disappearance over northern latitudes between 1988 and 2003, *J. Geophys. Res.*, *112*(D8), 1–15, doi:10.1029/2005JD006571.

Wang, L., M. Sharp, R. Brown, C. Derksen, and B. Rivard (2005), Evaluation of spring snow covered area depletion in the Canadian Arctic from NOAA snow charts, *Remote Sens. Environ.*, *95*(4), 453–463.

Wang, L., C. Derksen, R. Brown, and T. Markus (2013), Recent changes in pan-Arctic melt onset from satellite passive microwave measurements, *Geophys. Res. Lett.*, *40*(3), 1–7, doi:10.1002/grl.50098.

Wulder, M. A., T. A. Nelson, C. Derksen, and D. Seemann (2007), Snow cover variability across central Canada (1978–2002) derived from satellite passive microwave data, *Clim. Change*, *82*(1-2), 113–130, doi:10.1007/s10584-006-9148-9.

Ye, K., R. Wu, and Y. Liu, 2015: Interdecadal change of Eurasian snow, surface temperature and atmospheric circulation in the late 1980s. *J. Geophys. Res.*, **120**, 1–16, doi:10.1002/2015JD023148.

Zhang, T., S. A. Bowling, and K. Stamnes (1997), Impact of the atmosphere on surface radiative fluxes and snowmelt in the Arctic and Subarctic, *J. Geophys. Res.*, *102*(D4), 4287, doi:10.1029/96JD02548.

Zhang, T, Stamnes, K., Bowling, S. A. (1996), Impact of clouds on surface radiative fluxes and snowmelt in the Arctic and Subarctic, *J. Clim.*, *9*(9), 2110–2123.

Zhang, T, Stamnes, K., Bowling, S. A. (2001), Impact of the atmospheric thickness on the atmospheric downwelling longwave radiation and snowmelt under clear-sky conditions in the Arctic and Subarctic, *J. Clim.*, *18*(14) 920–939.

Zib, B. J., X. Dong, B. Xi, and A. Kennedy, 2012: Evaluation and Intercomparison of Cloud Fraction and Radiative Fluxes in Recent Reanalyses over the Arctic Using BSRN Surface Observations. J. Clim., 25, 2291–2305, doi:10.1175/JCLI-D-11-00147.1.

Chapter 4: Large-scale Linkages Among Sea ice and Greenland Ice Sheet Melt Onset and Surface Melt, 1979-2013

4.1 Introduction

The GrIS mass balance is experiencing an annual net loss with accelerating negative trends being driven by increased surface melt (Mote 2007; Fettweis et al. 2011). Melt from the GrIS has contributed about 5 mm to sea level rise between 2000-2008 (van den Broeke et al. 2009) and is predicted to be the dominant contributor to sea level rise along with Antarctica by the end of the century (Rignot et al. 2011). Concurrent with GrIS mass loss, Arctic sea ice is declining in coverage in all seasons, and has also exhibited accelerating losses since the late 1990's (Stroeve et al. 2012a; Cavalieri and Parkinson 2012). The summer ice-free season is now up to three months longer where ice loss has been greatest (Stammerjohn et al. 2012), with autumn freeze-up occurring later primarily because the warmer ocean requires longer to cool (Laxon et al. 2003).

Trends in sea ice melt onset have shown similar declines (Stroeve et al. 2006; Markus et al. 2009), with this date over occurring nearly 3 days sooner per decade across the Arctic and 3.4 – 7.3 days per decade in the area around Greenland. An earlier melt onset of just a few days substantially increases the accumulation of shortwave radiation, making an important contribution to heat storage during the melt season (Bitz et al. 1996). Earlier snow melt onset also allows for earlier melt pond formation, which strongly decreases surface albedo and has been found to be a good predictor of sea ice concentration in September (Shröder et al. 2012). The observed trends in both melt onset

and ice freeze-up closely follow trends in surface air temperature (Smith 1998). In addition, temperature anomalies over the Arctic Ocean exhibit a strong correlation with the Arctic Oscillation (AO), even with a lag of over a month (Rigor et al. 2002). Therefore, it is no surprise that this onset date has a well-documented link with the AO index (Belchansky et al. 2004; Tedesco et al. 2009).

While the decline in sea ice coverage has well-documented implications for the larger Arctic and even global climate, there is now extensive research documenting its impact on local-scale atmospheric processes. Sea ice variability is strongly tied to patterns of turbulent heat flux and subsequent surface temperature anomalies (Deser et al. 2000; Rinke et al. 2006). Anomalous open water regionally and Arctic-wide has generated increased upward heat and moisture fluxes, leading to increased tropospheric moisture, precipitation, and decreased static stability (Francis et al. 2009, Overland and Wang 2010, Stroeve et al. 2011; Cassano et al. 2014). Together, these local effects propagate through the atmosphere and influence the weather in distant locations (Higgins and Cassano 2009).

This brings up the possibility that recent sea ice loss has had an impact on the Greenland MOD and subsequent surface melt, which has seen accelerating increases coincide with sea ice loss. Sea ice loss has been hypothesized to influence GrIS mass balance via mechanisms ranging from local advection of warmer and moister air, increased precipitation, and synoptic-scale changes altering air mass advection and storm tracks (Koenig et al. 2014; Day et al. 2013). While local effects may have some influence on ice sheet melt (e.g. Rennermalm et al. 2009), changes in the large-scale circulation generating increased poleward heat advection have been the dominant drivers of some of

Greenland's record surface melt in recent years (Fettweis et al. 2011a; Hanna et al. 2013; Hanna et al. 2014; Noël et al. 2014). Understanding the covariability between sea ice, surface melt, and the atmospheric circulation is therefore critical to understanding the role of recent sea ice loss in summer melt on the GrIS.

A potentially key factor linking the Greenland MOD with total seasonal surface melt is the albedo feedback. The albedo of Greenland's ablation zone has declined since at least 2000 as surface melt has continued to accelerate (Box et al. 2012; Alexander et al. 2014). In case studies of Greenland's 2010 and 2012 record melt seasons, Tedesco et al. (2011) and Tedesco et al. (2013) partially attributed record surface melt to below average snowfall which helped to enhance the albedo feedback. The melt season also started early in 2010, which allowed earlier bare ice exposure and contributed to this feedback effect (Tedesco et al. 2011). Theoretically, the atmospheric drivers that initiate snow melt on the ice sheet could maintain a signal that continues into the melt season, generating surface melt anomalies of the same sign. Therefore, both the albedo feedback and the atmospheric circulation are of interest in addressing this lagged relationship.

A more comprehensive view regarding how sea ice and Greenland ice sheet surface melt are linked is still lacking, however, from the MOD in the spring to the melt processes later in the season. Insight into this important question can be gained by investigating the physical linkages in the Arctic climate system that range from the large scale atmospheric forcing to the local thermodynamic influence of sea ice. This study seeks to develop an overarching understanding of these potential linkages and where and when they occur using a variety of methods, primarily different statistical analyses

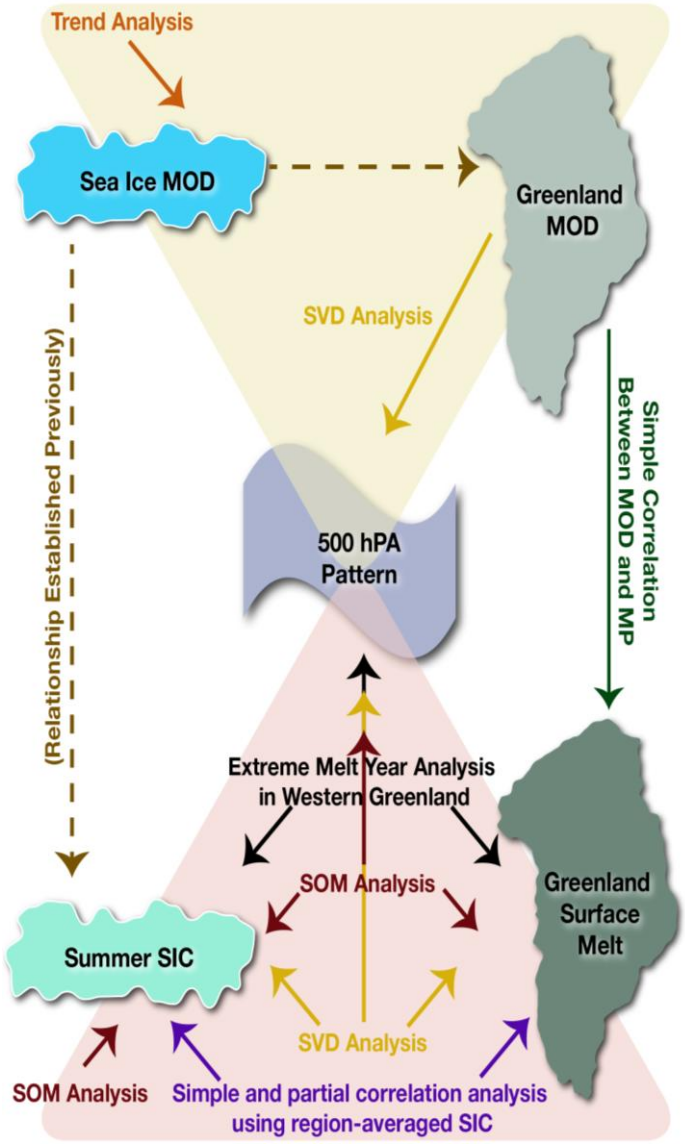

Fig. 4.1) Conceptual diagram of the research question and the methodology applied. Linkages between the five major physical components of the study are indicated by arrows, with dashed arrows indicating linkages not addressed here. Methods applied to analyzing these components and their relationships with others are given by the arrows connecting them.

applied to atmospheric reanalysis and regional climate model output across the Arctic and in the vicinity of Greenland over the 1979 – 2013 period. These conceptual linkages and the specific methods used to address them are outlined in Fig. 4.1, beginning with the MOD over sea ice and the GrIS and proceeding to processes occurring later in the season,

with the atmospheric circulation playing a central role at all time periods.

4.2 Data

500 hPa geopotential height fields were obtained from Modern Era Retrospective Analysis for Research and Applications (MERRA) reanalysis to diagnose atmospheric circulation patterns and its relationship with surface meteorological and hydrologic variables. MERRA is NASA's state-of-the-art reanalysis product generated with the Goddard Earth Observing System Model, version 5 (GEOS-5) data assimilation system (Bosilovich et al., 2011; Cullather and Bosilovich 2011, 2012; Rienecker et al. 2011). It is run on a 1/2° latitude by 2/3° longitude global grid with 72 hybrid-sigma vertical levels to produce analysis at 6 h intervals covering the modern satellite era from 1979 to 2013 for this study. These fields are forced by the atmospheric model, with inputs assimilated from a wide range of remote sensing (primarily satellite) observations in addition to nonhydrologic surface observations. MERRA has been evaluated extensively since its release (Cullather and Bosilovich 2012; Kennedy et al. 2011; Reichle et al. 2011) and has validated and compared favorably with other reanalysis products in the Arctic (Zib et al. 2012; Cullather and Bosilovich 2011; Lindsay et al. 2014).

Greenland ice sheet meltwater production between 1979 and 2013 was estimated by Modèle Atmosphérique Régional (MAR) v3.2 regional climate model data for Greenland (Tedesco et al. 2014). MAR is a three-dimensional coupled atmosphere-land surface model that uses data from ERA-40 (1958–2002) and ERA-Interim (2002–2013) reanalysis at its lateral boundaries to predict the evolution of the land-atmosphere system

at 6-hour intervals. MAR's atmospheric model is coupled to the 1-D Surface Vegetation Atmosphere Transfer scheme, SISVAT (Gallée and Schayes 1994; De Ridder and Gallée 1998), which simulates surface properties and the exchange of mass and energy between the surface and the atmosphere in both directions. SISVAT incorporates an interactive snow model based on the 1-D layered snowpack model, CROCUS (Brun et al. 1992). The data has a polar stereographic projection with an approximate grid cell size of 25 x 25 km. MAR has been validated through comparison with ground measurements (e.g. Lefebre et al. 2003; Gallée et al. 2005; Lefebre et al. 2005) and satellite data (e.g. Fettweis et al. 2005, 2011a; Tedesco et al. 2011), and applied to simulate long-term changes in the GrIS SMB and surface melt extent (Fettweis et al. 2005, 2011a; Tedesco et al. 2008, 2011).

Here, meltwater production was only used for grid cells classified by MAR as >99% ice sheet to mask the tundra region of Greenland. In addition, meltwater production values of less than 1 mm day^{-1} in all grid cells were recoded to zero to account for MAR's scaled output (where very small values are output when they should be zero). Finally, grid cells in the interior ice sheet where mean monthly meltwater production does not exceed 1 mm day^{-1} to account for spurious correlations arising from a very limited number of dates resulting in nonzero mean values of meltwater production.

The National Snow and Ice Data Center (NSIDC) provides daily and monthly fields of sea ice concentration at 25 km spatial resolution derived from Nimbus-7 Scanning Multichannel Microwave Radiometer (SMMR) and Special Sensor Microwave/Imager (SSM/I) brightness temperature on DMSP platforms using the NASA Team sea ice algorithm (Cavalieri et al. 1996; Meier et al. 2006). The combined record

extends from 1979 through present, and monthly data were used for the JJA summer season. These data were regridded to MERRA model grid to facilitate analysis. This dataset has been extensively used and validated (Markus and Cavalieri 2000; Meier and Stroeve 2008; Meier 2005).

Sea ice melt onset data (Markus et al. 2009) are derived from the same sensors as SIC using an algorithm that employs multiple indicators of melt to generate a best estimate of snow melt onset on top of sea ice. These indicators include the brightness temperature (Tb) ratio between 19 V and 37 V, SIC, and ice age. Continuous melt onset begins when the sum of the weights for these indicators is maximized according to the onset algorithm.

GrIS surface melt onset is a variable within NASA's MEaSUREs (Making Earth System Data Records for Use in Research Environments) State of the Cryosphere climate data record available at NSIDC for the years 1979 – 2012 (Robinson et al. 2014). Onset dates are calculated within this dataset using the MEaSUREs Greenland surface melt climate data record (Mote 2012), with data regridded from 25 km on EASE-Grid 2.0 to MAR grid resolution using nearest neighbor interpolation. This dataset uses SMMR, SSM/I and Special Sensor Microwave Imager and Sounder (SSMIS) data. The occurrence of melt is determined from gridded Tbs (brightness temperature) from these passive microwave radiometers. The product is a binary estimate of melt or no melt produced by identifying grid cells in the daily Tbs that exceed threshold Tbs associated with 1% liquid water by volume in the snow, calculated daily.

4.3 Methods

Singular value decomposition (SVD) analysis was used to investigate co-variability between sea ice concentration, Greenland ice sheet meltwater production, and 500 hPa geopotential heights, as well as the latter with Greenland MOD. SVD was applied to two fields at a time to produce pairs of coupled spatial patterns that explain maximum mean squared temporal covariance between the two (Bretherton et al. 1992). Each pair explains a fraction of the squared covariance (SC) between the two fields, where the first pair explains the largest SC, and the second the maximum unexplained fraction and so on (Björnsson and Venegas 1997). The temporal evolution of each pair's corresponding pattern in the two datasets are represented by the pair's associated expansion coefficients (EC where subscripts GrIS, SIC, MOD, and 500 denote the EC for ice sheet melt, sea ice concentration, GrIS melt onset date, and the 500 hPa heights, respectively). These ECs were used to calculate heterogeneous correlation (HC) maps, which show the correlation coefficients (i.e. the strength of the relationship) between each EC and the opposing data field. Here, HC maps are constructed using Pearson correlation coefficients and only values that are statistically significant at alpha = 0.05 are reported. Statistical significance for the HC correlation coefficients was determined with a two sided t-test (e.g. Chapman McGrew et al. 2014). If significant correlations were found in both HC maps, the spatial patterns of the correlation show where those fields are related. SVD has widely been used to investigate coupled modes of variability, including relationships between Arctic sea ice and snow cover (Ghatak et al. 2010), and Arctic sea ice and atmospheric variables (Stroeve et al. 2008).

The SVD analysis was used to identify sea ice regions with high covariability

with GrIS meltwater production. As will be shown, three regions were identified (Beaufort Sea, Baffin Bay and Fram Strait). To further investigate how SIC in these regions is related to GrIS meltwater production, SIC for each of the three regions were spatially aggregated, detrended and correlated (Pearson's r) with detrended time series of GrIS meltwater production.

To remove the influence of the atmospheric circulation from the correlation between SIC and GrIS meltwater production, the Greenland Blocking Index (GBI) was removed through partial correlation. The GBI is the 500 hPA geopotential height field averaged between 20º – 80º W, 60º – 80º N (Fang 2004), used here as a metric representing large scale atmospheric circulation patterns in the region. GBI data was obtained from NOAA's Earth System Research Laboratory. The GBI is used here rather than the North Atlantic Oscillation (NAO) or Arctic Oscillation (AO) because it is more representative of the atmospheric anomalies that affect the entire ice sheet (as GrIS meltwater production is spatially averaged in some analyses). The influence of the NAO and AO on GrIS mass balance has been extensively studied (Appenzeller et al. 1998, Mosley-Thompson et al. 2005; Hanna et al. 2008; Fettweis et al. 2013) and is highly correlated with the GBI (Hanna et al. 2014). However, for this analysis the GBI was used because it has been found to correlate better with Greenland runoff than the NAO (Hanna et al. 2012). One hypothesis is that the GBI (large scale circulation patterns) has a first order influence on both SIC and GriS meltwater production. To investigate this, partial correlation analysis of SIC in each region and GrIS meltwater production with GBI removed (all time series detrended) was performed.

Self organizing maps (SOM) are employed to analyze SIC data and atmospheric

circulation patterns. SOM algorithms are neural network algorithms that use unsupervised classification to perform non-linear mapping of high-dimensional datasets (Kohonen 2001). Similar to cluster analysis, this method effectively reduces a large dataset into fewer representative samples without assumptions about the final structure of these samples. This method has been used previously in similar studies of Arctic synoptic climatology and its changes (Cassano et al. 2006; Skific et al. 2009; Higgins and Cassano 2009) as well as specifically over the Greenland domain (Schuenemann et al. 2009; Schuenemann and Cassano 2009).

Here, SOM analysis is used in two ways: first, to assess the changes observed in sea ice coverage regionally in the Arctic throughout the study period. This type of SOM generates a "master" map of different SIC regimes throughout the summer, following similar applications by Reusch and Alley (2007). The second type of analysis is done on the field of 500 hPa geopotential heights across the northern hemisphere north of 60°N to develop a summer synoptic climatology of the Arctic. In this application, training data are drawn from daily 500 height fields in JJA, yielding a master SOM map with 30 "nodes" that represent the spectrum of synoptic patterns. The number of nodes is typically user-defined and is a trade-off between forcing the daily circulation pattern into a category that is a poor fit (too few nodes) to displaying an overwhelming amount of data (too many nodes). Data were first weighted by the square root of the cosine of the latitude to account for the poleward grid cell area bias in the model grid. MAR output fields were then mapped onto this master map by identifying the node corresponding most closely (smallest Euclidean distance) to the observed synoptic pattern while assigning and tabulating the value of the observed variable to that node.

4.4 Sea Ice and Greenland Melt Onset Date Analysis

Trends in MOD on sea ice show that this date has come earlier in most locations since 1979, and trends in excess of one week per decade exist almost exclusively in the marginal ice zone (Fig. 4.2). Here, trends are as large as two weeks per decade, and are greatest in Baffin Bay, Greenland Sea, and the Kara Sea. Given that many of the strongest trends are found in the waters surrounding Greenland and the well-established surface melt trends on the GrIS, analysis next shifts to the GrIS.

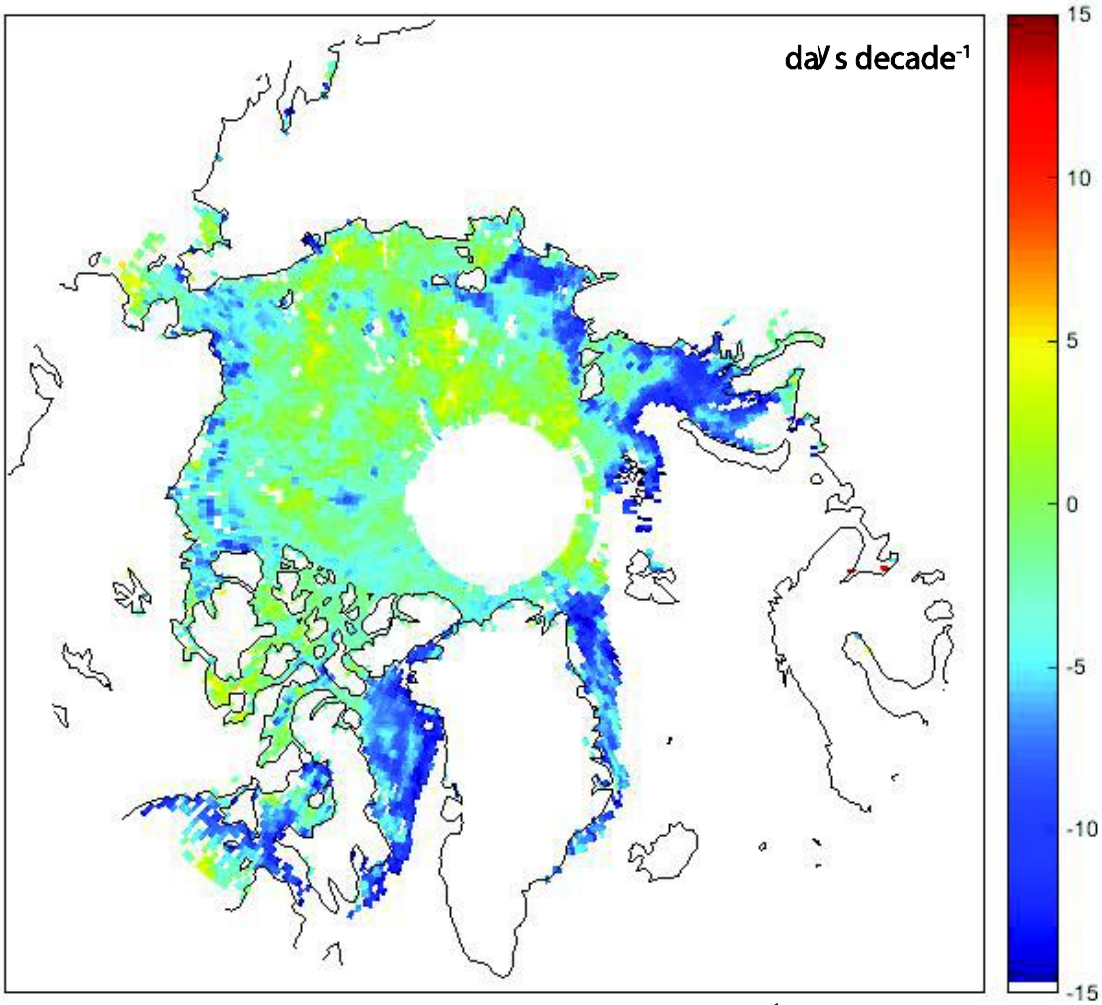

Fig. 4.2) Trend in sea ice melt onset date (MOD; days decade^{-1}). Trends were not calculated for grid cells without a continuous time series of MOD dates.

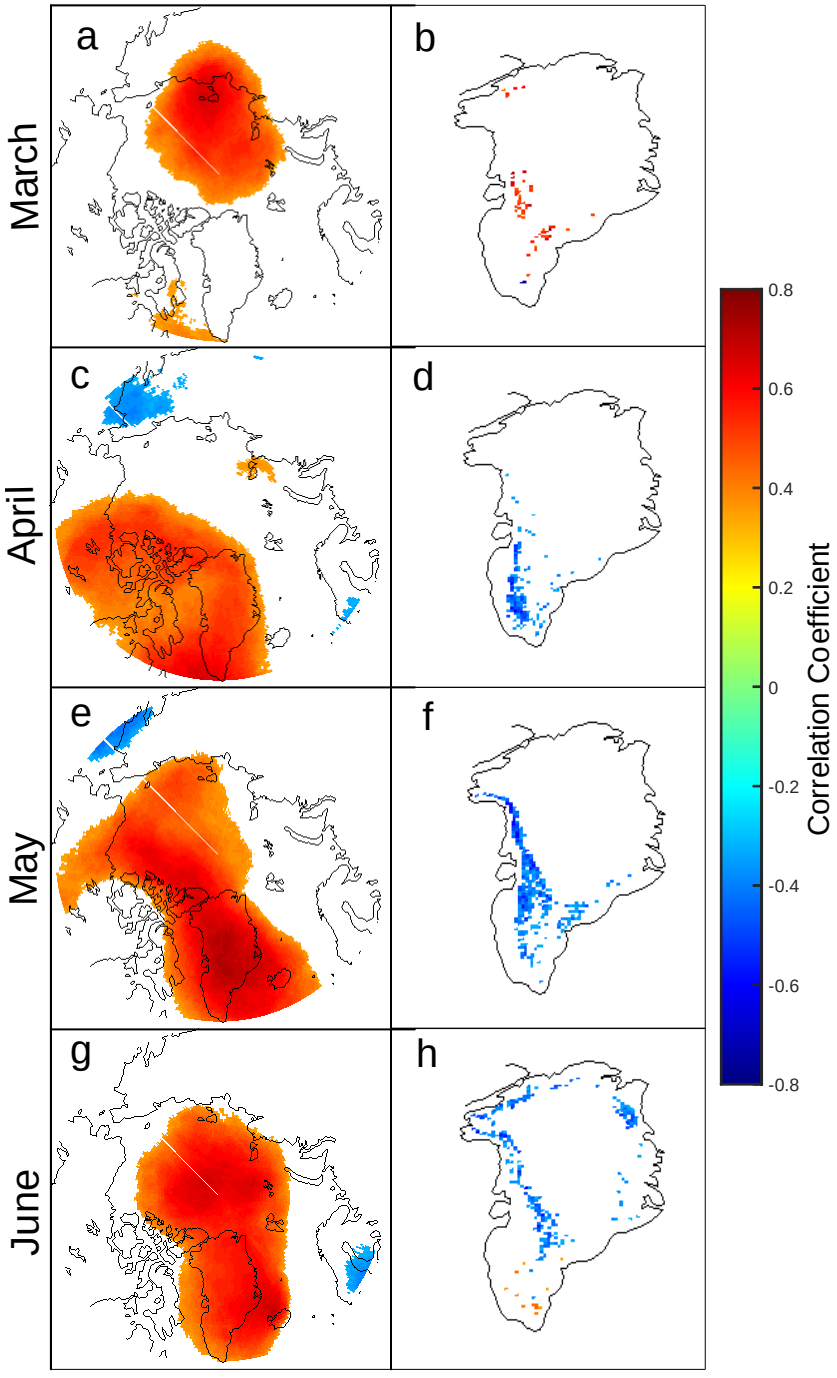

Fig. 4.3) Heterogeneous correlation between Greenland MOD and 500 hPa geopotential heights in the leading SVD mode in MAMJ. Column 1 is the correlation between 500 hPa geopotential heights and EC_{Gris}. Column 2 is the correlation between meltwater production and EC_{500}. All data are detrended anomalies.

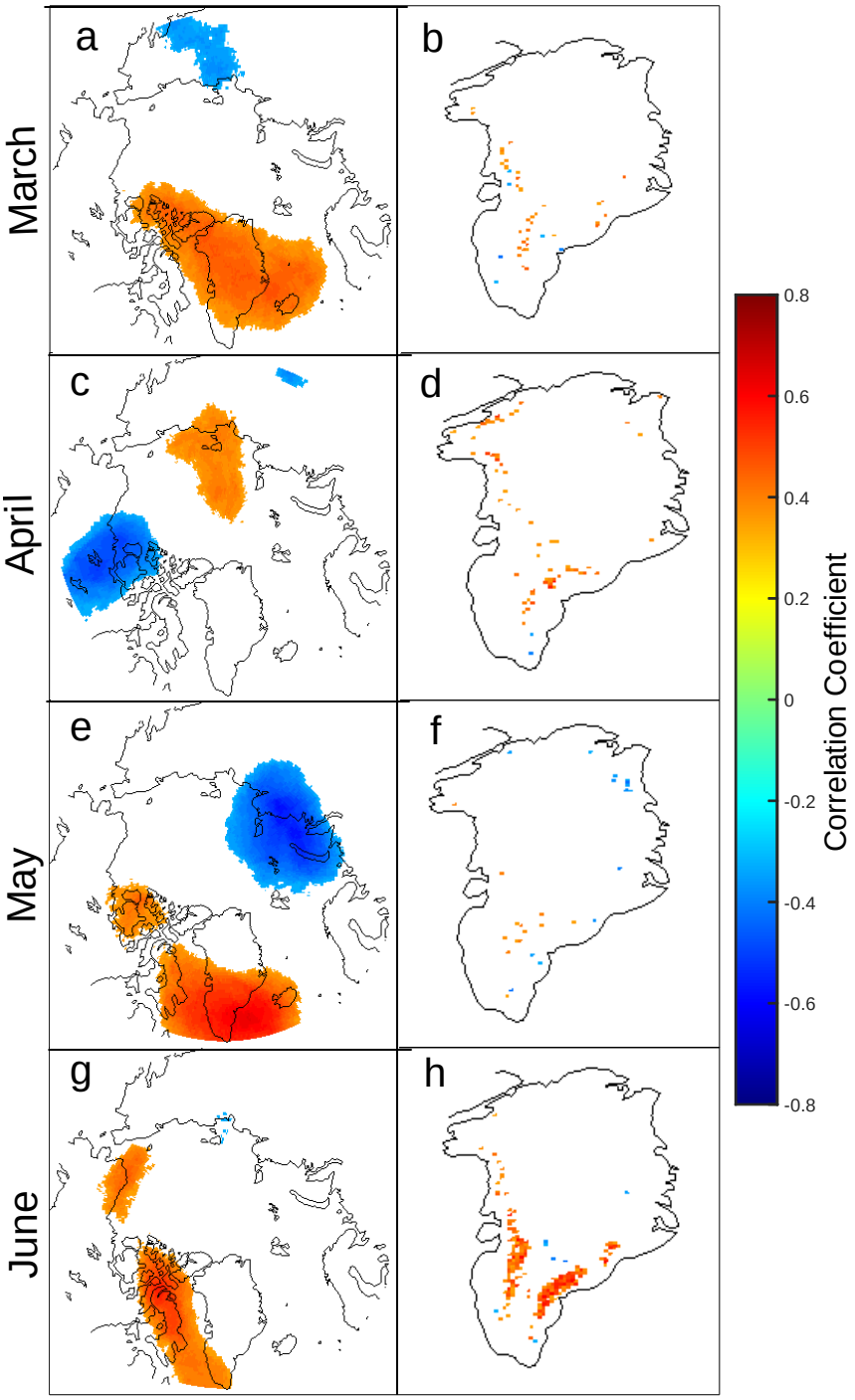

Fig. 4.4) As in Fig. 4.3, but for the 2nd SVD mode.

While sea ice MOD and Greenland MOD do not appear to be correlated (analysis not shown), any relationship between the two would likely be due to a response to

simultaneous atmospheric forcing. To further understand how closely Greenland MOD covaries with the 500 hPa height pattern, SVD analysis between these two monthly fields was undertaken for the months of MAMJ (Fig 4.3). The correlation with between 500 hPa geopotential heights and EC_{MOD} demonstrates a strong tendency for ridging in the vicinity of Greenland when the MOD occurs, as would be expected to advect anomalously warm air poleward (Fig. 4.3a,c,e,g). The only exception to this is in March when most parts of the ablation zone do not consistently experience melt onset. HC maps of the first SVD mode shows that there is a relatively strong correlation between MOD and EC_{500}, particularly over the part of the ice sheet where the MOD is occurring in that particular month (Fig. 4.3b,d,f,h). This correlation moves further up in elevation as the season advances and melt begins at higher elevations. The fraction of explained variance in this leading SVD mode is 0.48, 0.38, 0.75, and 0.66 for March, April, May, and June, respectively, so it is likely that at least the second mode contains significant information as well.

The HC maps for the second SVD mode tend to express height patterns at a more regional scale (Fig. 4.4a,c,e,g) with centers of action (positive and negative correlations) in different regions each month. The correlation between MOD and EC_{500} (Fig. 4.4b,d,f,h) is weak with only a few small areas with significant correlations with the exception of June. In June, a band of high correlations in the south roughly coincides with regional height anomalies.

Next, analysis expands later into the summer to GrIS surface meltwater production, and the potential for Greenland MOD anomalies to predict subsequent surface melt. This is partly motivated by a similar relationship that has been established

for sea ice, where melt pond occurrence early in the season is a good predictor of September sea ice anomalies (Shröder et al. 2014). Significant negative correlations exist between the MOD over Greenland and the total seasonal meltwater production in each grid cell (Fig. 4.5). However, the significant correlations are primarily at the ice sheet edge and do not extend inland from here. The cause for significant correlations is likely a combination of the albedo feedback on the ice and a persistence of atmospheric patterns into the summer, but further analysis on this research question is beyond the scope of this chapter.

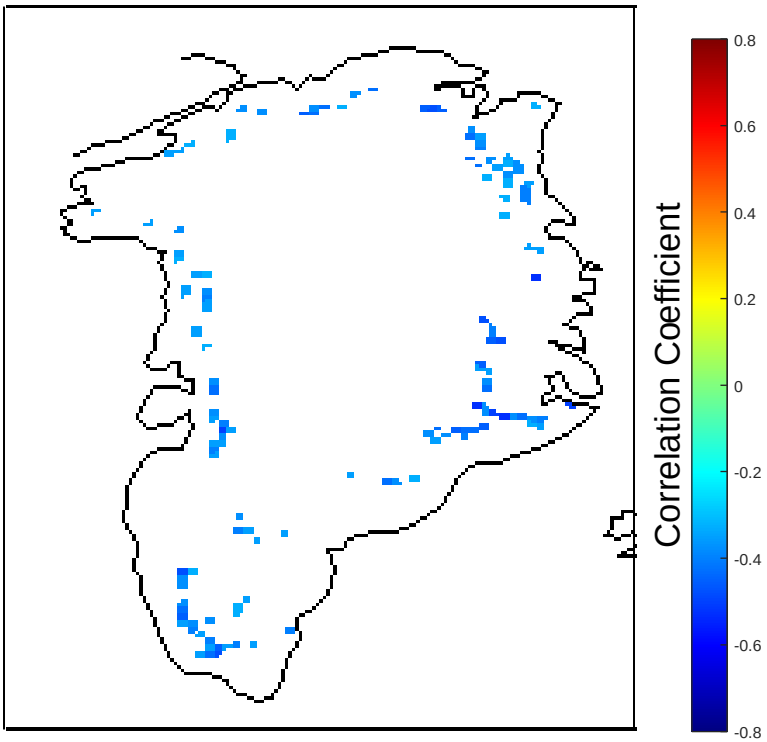

Fig. 4.5) Pearson correlation between Greenland MOD and accumulated meltwater production in the following summer. Only correlation coefficients significant at $\alpha = 0.05$ are shown.

4.5 SOM Analysis of Sea Ice Concentration

Given the concurrent decline in SIC over the same time period, a spatial analysis of summer SIC over time was performed before developing causal linkages with GrIS surface melt and circulation patterns. SOM analysis was done on anomalies of SIC during JJA from 1979 – 2013 to show an overview of how SIC has changed over this time period and where changes have been the greatest. Anomalies were calculated relative to the entire summer, so June is represented by mostly positive SIC anomalies (Fig. 4.6, left nodes) and August is represented by mostly negative anomalies (Fig. 4.6, right nodes).

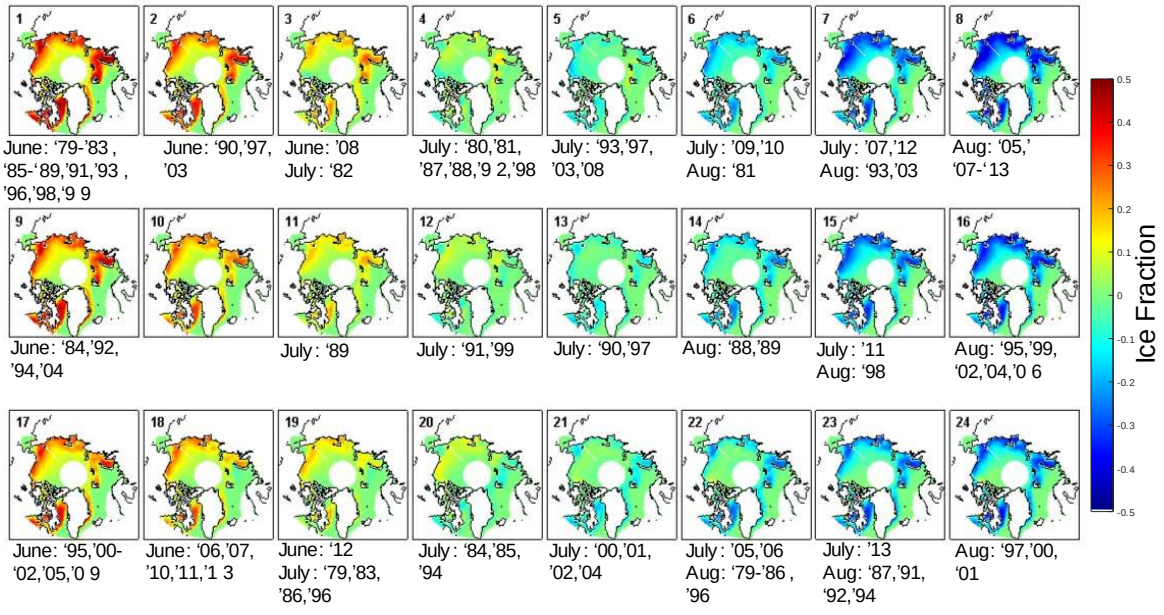

Fig. 4.6) SIC patterns from a 3 x 8 SOM analysis using JJA monthly SIC. Units are ice fraction anomaly.

The structure of this master SOM map is such that the strongest of these anomalies are characterized in the upper left and right corners. Therefore, the strong

decreasing trends in SIC nearly everywhere are easily identified by the general temporal progression of nodes over the course of 35 years, moving from top to bottom in June, bottom to top in August, and generally from left to right in all months. In a few instances, the best matching node in August has occurred in July (nodes 6,7, and 15) and the matching node for July has occurred in June (nodes 3 and 19), meaning that the difference between the advancement in the sea ice melt season was an entire month in these particular years.

4.6 CovariabilityAmong GrIS melt, SIC, and the Atmosphere

Given this context, the next part of the analysis explores SIC as it relates to summer GrIS surface melt and atmospheric forcing of both. The leading SVD mode expressing the correlation between GrIS meltwater production and SIC explains roughly half of the mean SC (0.62, 0.73, 0.42, in June, July, and August, respectively). The HC maps derived from the leading SVD mode show three general regions of sea ice with relatively high correlation, namely Baffin Bay, a large part of Beaufort Sea, and correlation of the opposite sign in Fram Strait (Fig. 4.7a,e,i). In June, all three sea ice regions have strong correlations with EC_{GrIS} exceeding $r^2 = 0.50$, and meltwater production is highly correlated with EC_{SIC} for the majority of the ice sheet surface (Fig. 4.7b). In July and August, the strong correlations for Beaufort Sea persist, while Baffin Bay correlations with EC_{GrIS} are reduced and Fram Strait correlations disappear (Fig. 4.7e,i). At the same time, meltwater production correlations with EC_{SIC} are restricted more to the west side of the ice sheet in July, and are weak area-wide in August (Fig.

4.7f,j).

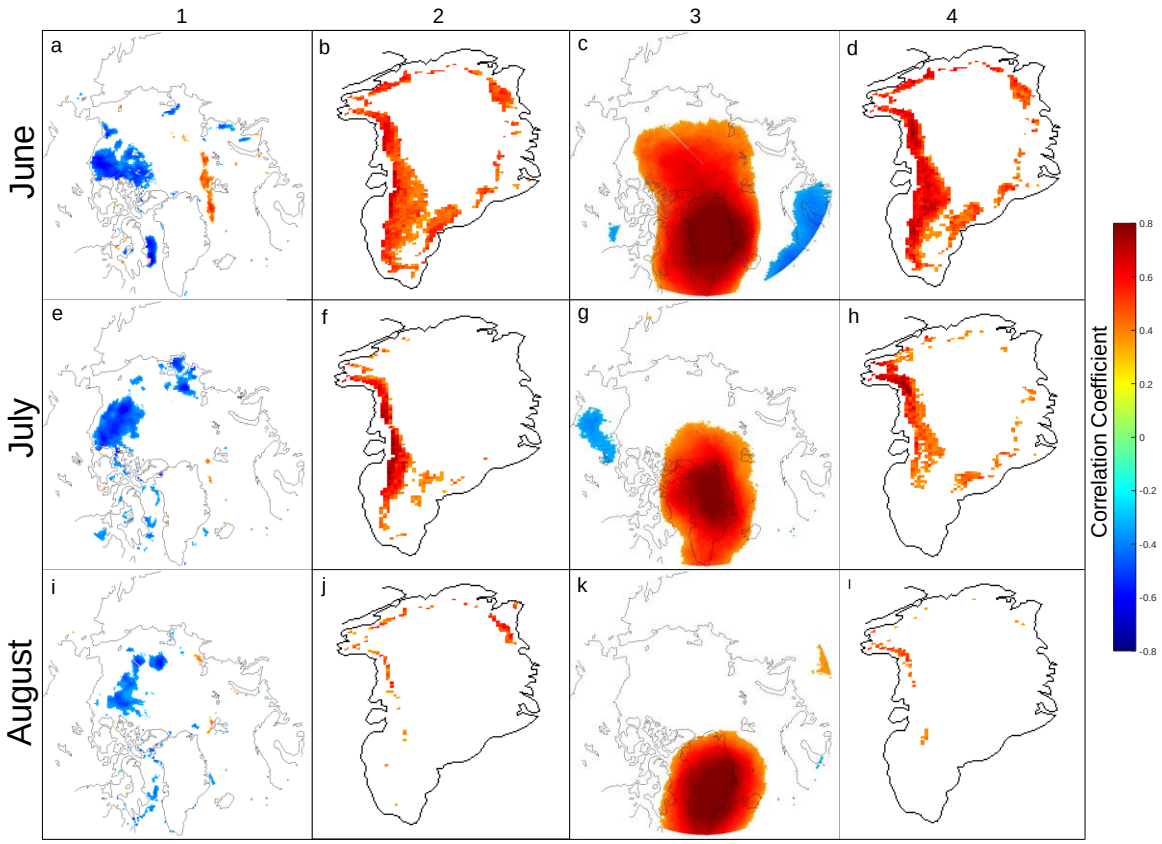

Fig. 4.7) Heterogeneous correlation between variables in the leading SVD mode in JJA. Column 1 is the correlation between sea ice concentration and EC_{Gris}. Column 2 is the correlation between meltwater production and EC_{SIC}. Column 3 is the correlation between 500 hPa geopotential heights and EC_{Gris}. Column 4 is the correlation between meltwater production and the EC_{500}. All data are detrended anomalies.

The leading SVD mode using 500 hPa geopotential heights and meltwater production explains the majority of mean SC in June and July (0.79 and 0.60, respectively), but less than half in August (0.37; Fig. 4.7c,g,k). The HC maps shows a clear tendency for positive height anomalies over the Greenland side of the Arctic, though this relationship is somewhat weaker in July and August (Fig. 4.7c,g,k). This spatial pattern covaries with GrIS meltwater production again over most of the ice sheet in June, and is restricted to mostly the west side in July.

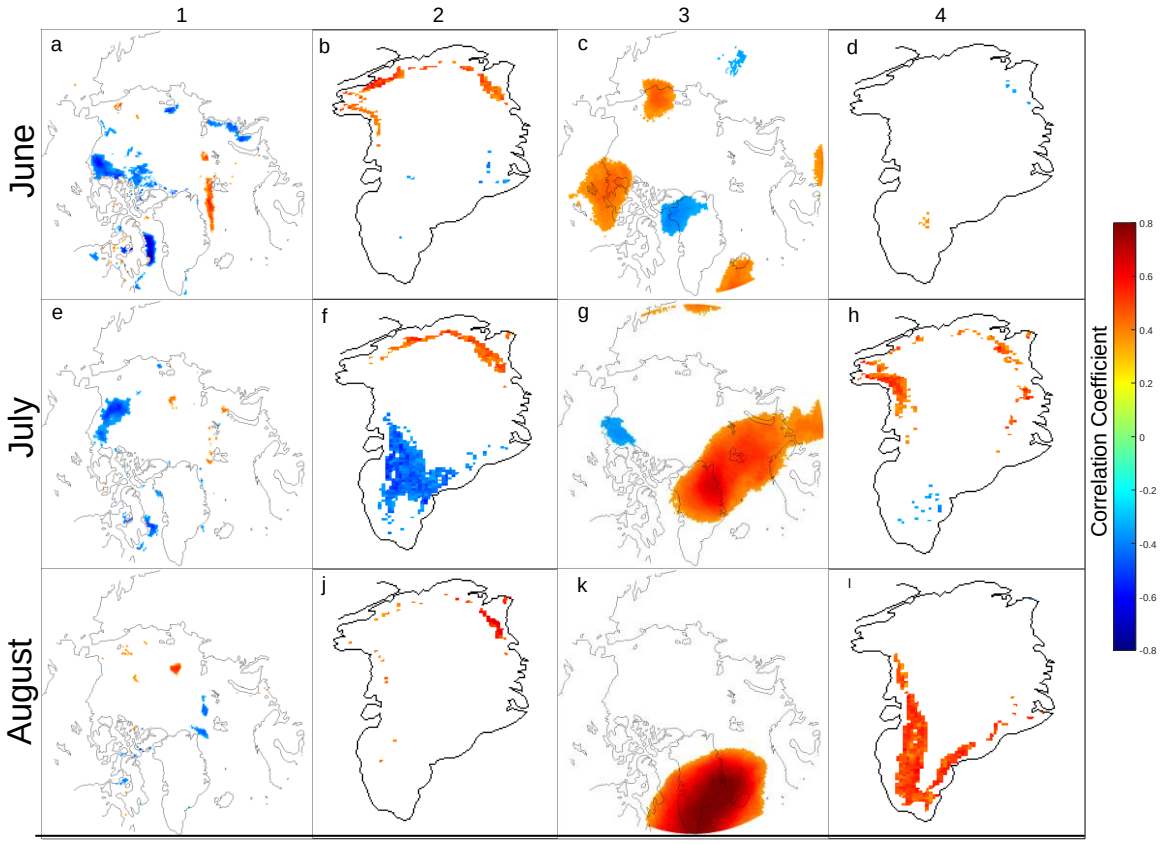

Fig. 4.8) As in Fig. 4.7, but for the 2nd SVD mode.

The leading SVD mode explains approximately half of the variance in the dataset, so it is likely that at least some of ECs in the second mode are physically meaningful as well. This second mode explains 0.10, 0.06, and 0.33 of the mean SC in June, July, and August, respectively, for the SVD of SIC and GrIS meltwater production, and 0.08, 0.14, and 0.30 of respective SC between 500 hPa heights and meltwater production. The HC map of June SIC vs. EC_{GrIS} (Fig. 4.8a) is very similar to the same HC map of the leading SVD mode (Fig. 4.7a) but July and August show less of a relationship (Fig. 4.8e,i). The HC maps of involving 500 hPa heights (Fig. 4.8, righthand panels) confirm that much of the strong relationship among these variables is again due to the geopotential height field in the vicinity of Greenland. Strong positive correlations between this field and EC_{GrIS}

show up northeast (July) and southeast (August) of Greenland (Fig. 4.8g,k) with corresponding strong correlations over the northeastern (July) and southeastern (August) GrIS between meltwater production and EC_{GrIS} (Fig. 4.8h,l).

The three sea ice regions that show strong correlation with EC_{GrIS} (i.e. Beaufort Sea, Baffin Bay and Fram Strait) are further examined by using Pearson correlation and partial correlation analysis. Detrended June SIC in the Fram Strait region shows a strong correlation with 500 hPA heights forming a ridge across most of Greenland into the Arctic Ocean (Fig. 4.9a). June SIC here also displays a positive correlation with meltwater production along the northeastern coast of Greenland (Fig. 4.9b). However, the bulk of this correlation can be explained by the GBI, which is confirmed in Fig. 4.9c where most of the significant correlation is absent in the partial correlation map in June. In July and August, these relationships appear to break down when the height pattern that supports it appears to shift away from Greenland and weaken (Fig. 4.9d-i) and sea ice in the Fram Strait region no longer appears as strongly correlated with EC_{GrIS} in the HC maps (Fig. 4.9e,i).

The correlation between SIC in Baffin Bay and geopotential heights is strongest in June before this signal mostly disappears in July and August (Fig. 4.10a,d,g), which is associated with a weakening Baffin Bay sea ice correlation with EC_{GrIS} in the HC maps (Fig. 4.7a,e,i). Significant correlations with meltwater production are focused on the west side of the ice sheet in June and July and are nearly gone by August (Fig. 4.10b,e,h).

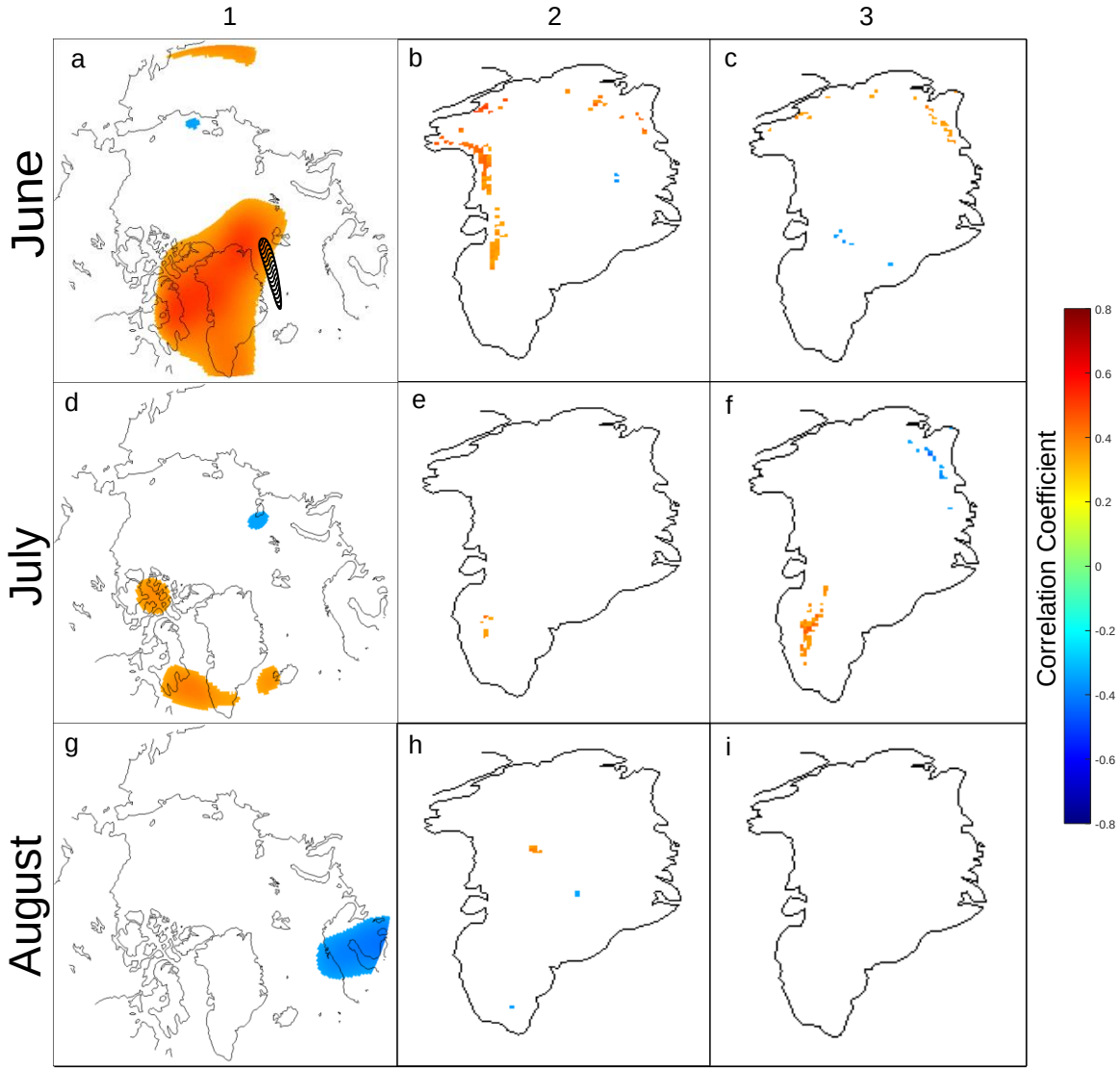

Fig. 4.9) Correlation between: Column 1) spatially averaged SIC in Fram Strait (indicated in (a)) and 500 hPa geopotential height field, Column 2) spatially averaged SIC in Fram Strait and Greenland meltwater production, and Column 3) same as Column 2 but with the effect of the Greenland Blocking Index removed (partial correlation). All data are detrended anomalies.

Partial correlation analysis indicates that the GBI explains a significant portion of this correlation in July, but not in June, leaving the possibility that variations in Baffin Bay sea ice are responsible for more of the correlation with surface melt in western Greenland.

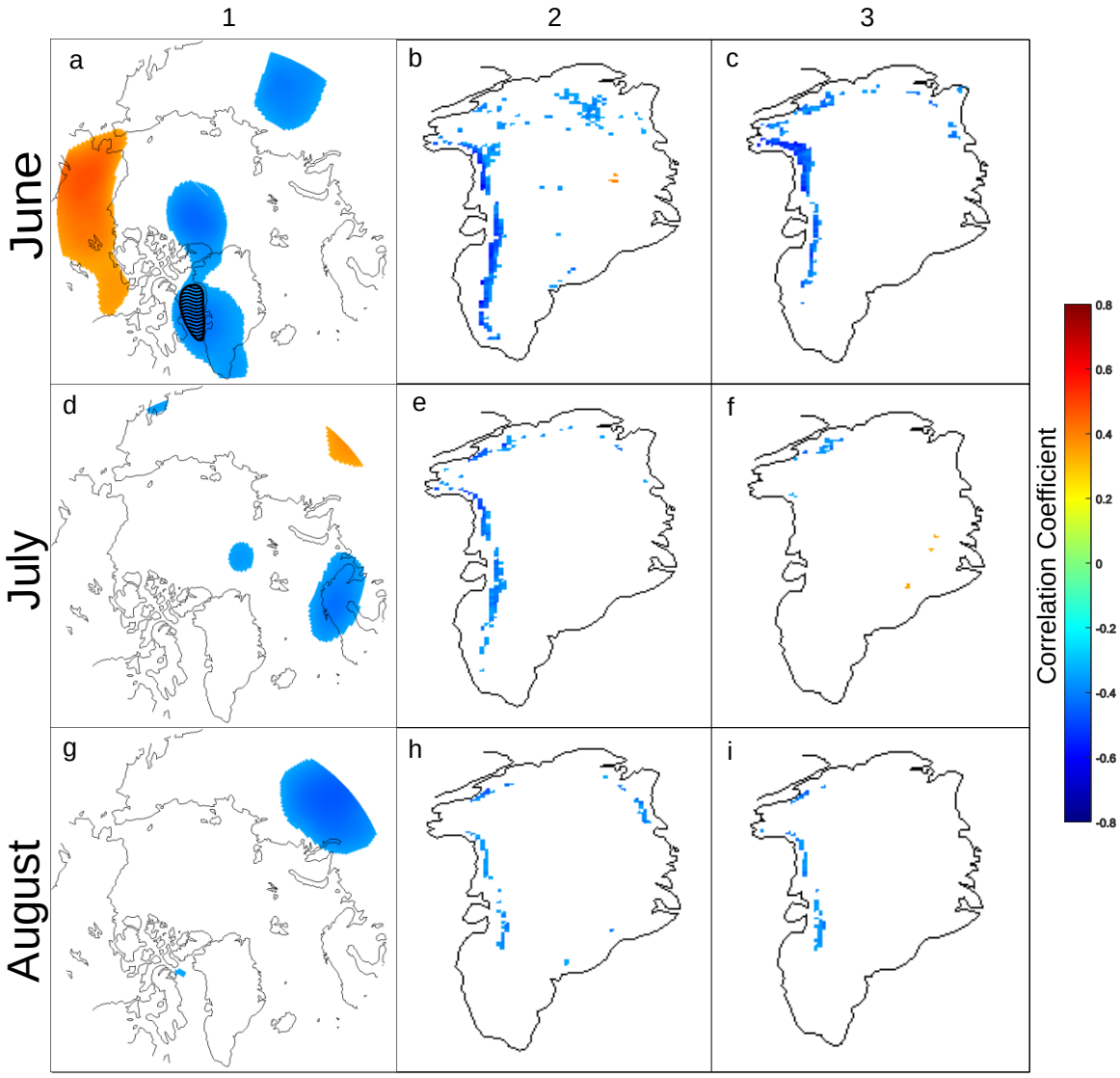

Fig. 4.10) As in Fig. 4.9, but using a spatially-averaged vector of SIC in Baffin Bay.

In the Beaufort Sea, both 500 hPa heights and SIC closely covary particularly in June and July (Fig. 4.11a,d), in concert with high SIC covariance in this region with EC_{Gris} in the HC maps (Fig. 4.7). Here, the positive correlations between SIC and GrIS meltwater production are persistent through the summer. However, the strong relationship between Beaufort SIC and GrIS meltwater production is reduced considerably when the influence of the GBI index is removed (Fig. 4.11c,f,i).

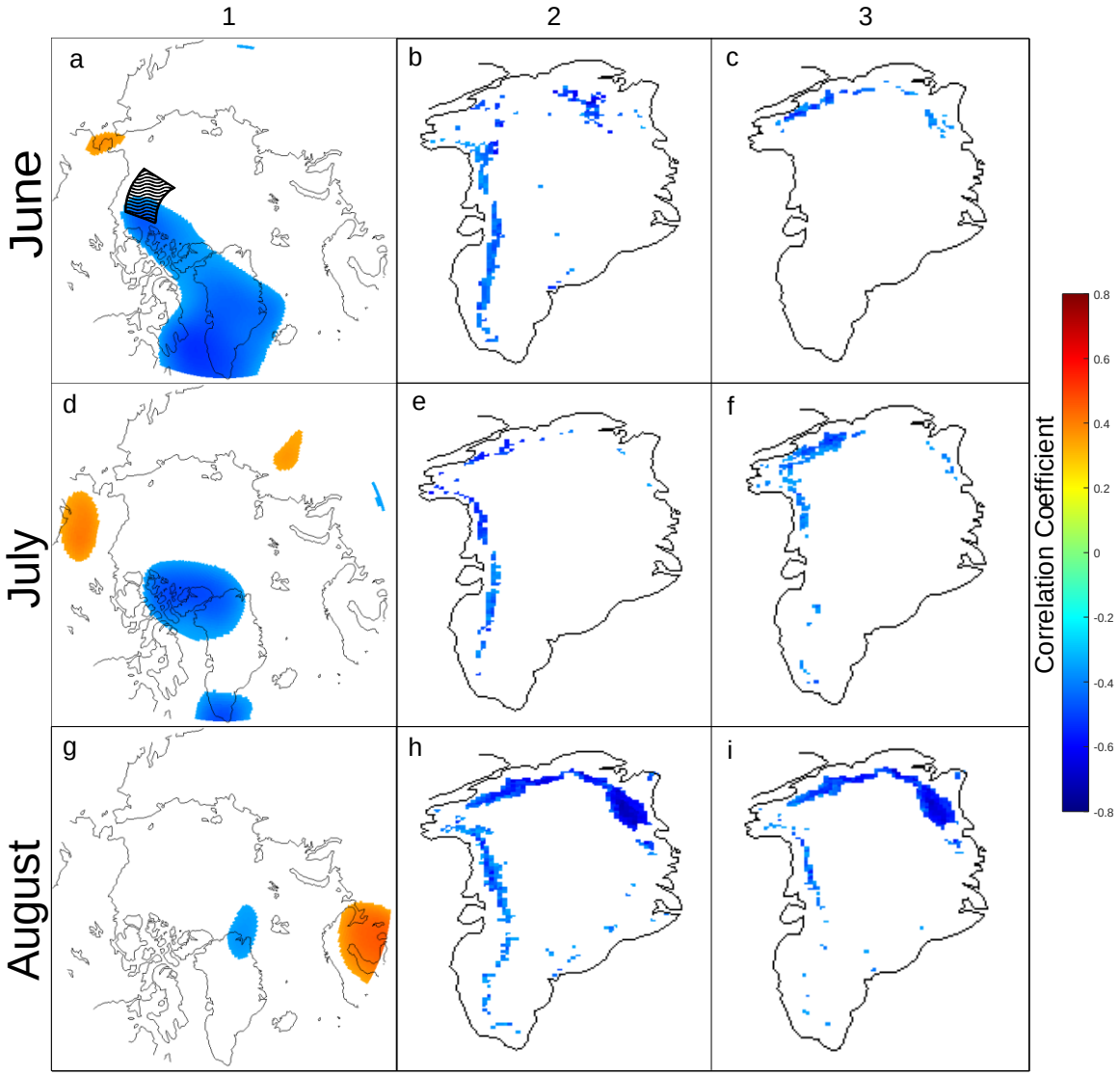

Fig. 4.11) As in Fig. 4.9, but using a spatially-averaged vector of SIC in Beaufort Sea.

The analysis above (Figs. 4.7-4.11) shows that the correlation and covariance patterns get weaker as the summer progresses, with June clearly exhibiting the strongest relationship in all three regions. SIC and meltwater production generally do not correlate well when the GBI is removed, with the exception being primarily Baffin Bay SIC covarying with west GrIS melt in June and Beaufort Sea SIC covarying with northern GrIS melt in August (Figs. 4.11c and 4.11i). This confirms that much of the relationship

between SIC and meltwater production exists due to the atmospheric circulation as an intervening variable.

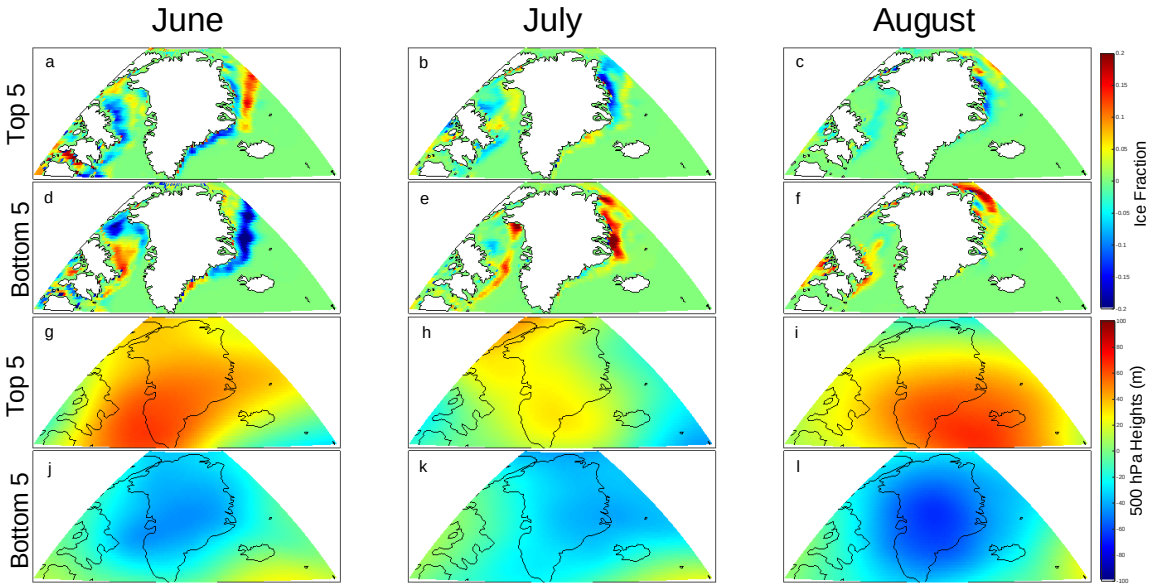

Fig. 4.12) Detrended anomalies of SIC (top) and 500 hPa geopotential heights (bottom) averaged over the 5 highest and lowest melt years in June, July, and August as indicated by detrended meltwater production anomalies in the indicated region of the ice sheet. Units are ice fraction (top) and m (bottom).

Because there is a potential local influence on GrIS melt from Baffin Bay, we next focus on GrIS meltwater production only in west-central Greenland. The highest and lowest melt years (after detrending) here consistently correspond with patterns of anomalous SIC and geopotential heights in these years (Fig. 4.12). These variables show much less variation by month, though a weaker relationship appears particularly in the height field (this follows results from SVD; Fig. 4.12g-l). Additionally, a strong SIC pattern is evident not just in Baffin Bay but consistently on the east side of Greenland and is equally as strong (Fig. 4.12a-f). This indicates that the processes responsible for this signal expression to the west of Greenland probably also exist on a scale large enough to have an effect of similar strength on sea ice in the East Greenland Sea; most likely a

persistent ridge or trough, as suggested by previous analysis. By August, sea ice in Baffin Bay has melted in most years so the relationships are not as strong. However, positive anomalies in Baffin Bay SIC still clearly appear in the lowest melt years (Fig. 4.12f).

4.7 SOM Analysis of 500 hPA Height Patterns

To better understand which atmospheric patterns best support high and low meltwater production, SOM analysis was done on daily anomalies of 500 hPa geopotential heights in JJA (Fig. 4.13). The master SOM divides these fields into a continuum of patterns that occur during the summer months in the Arctic, with the

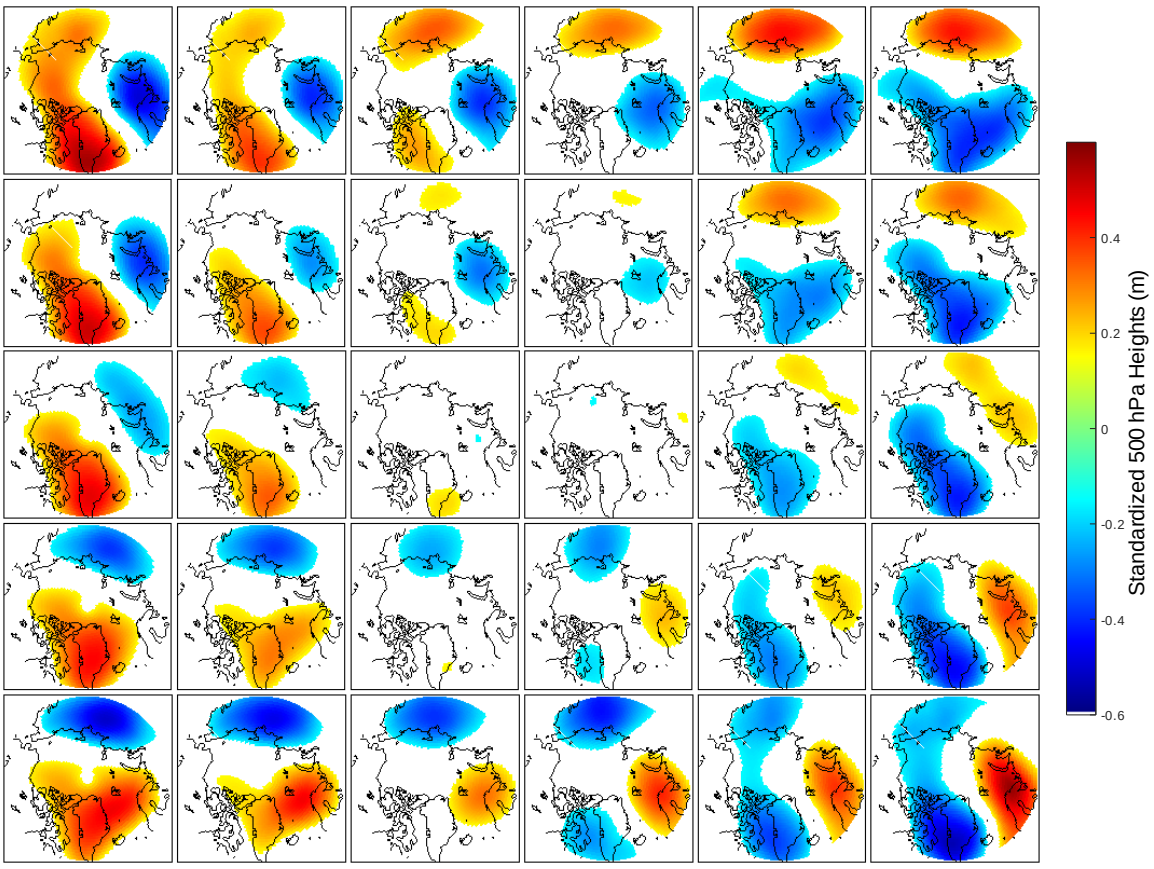

Fig. 4.13) Master SOM of daily 500 hPa geopotential height anomalies (m).

a

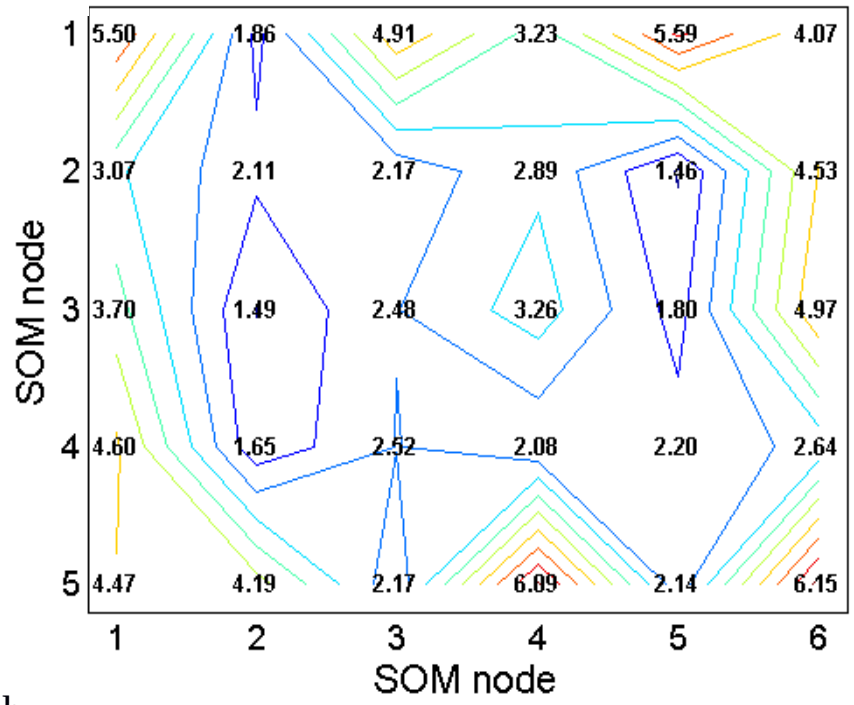

b

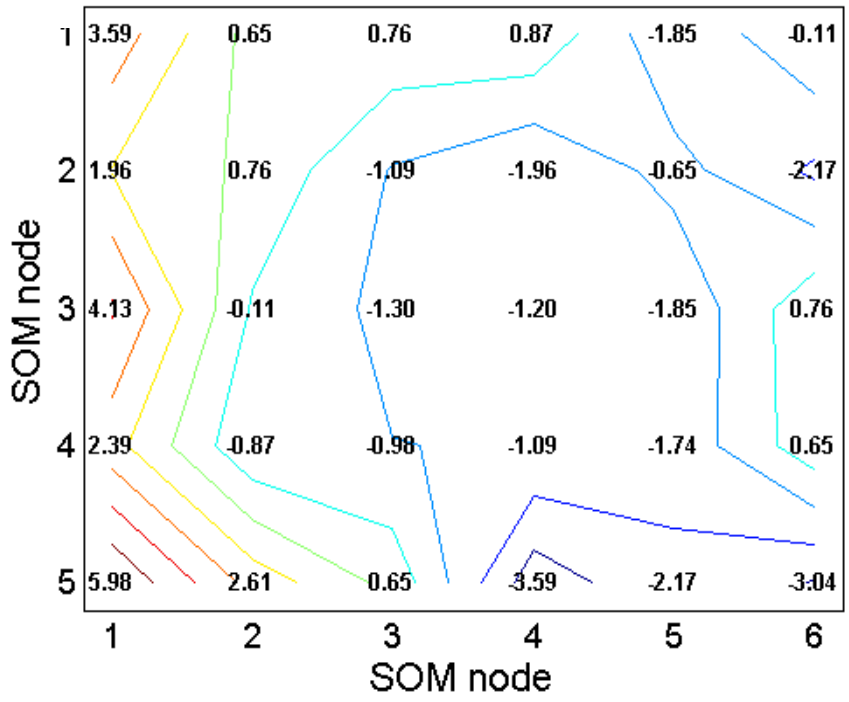

Fig. 4.14) JJA SOM pattern frequencies for a) the 1979-2013 period, b) difference in pattern frequencies between dates in the 10-year periods 2004-2013 and 1979-1988. The position of each number corresponds with the synoptic pattern of the same position in the master SOM in Fig. 4.13.

strongest anomalies generally on the periphery, and particularly in the upper left and lower right corners. The node frequency chart (Fig. 4.14a), a measure of the percentage of total days that match most closely to each node, shows that there is also a higher frequency of data represented in periphery nodes. This is to be expected, as a SOM analysis of circulation patterns typically has a transition area in the middle that is a poor representative of the true pattern.

The first and last ten years of the period (1979-1988 and 2004-2013) were chosen to assess the change in node frequency of the master map. Subtracting the subset of best matching units for each node for these two periods shows the change in frequency of each of these circulation patterns (Fig. 4.14b). There are relatively minor changes in most of the nodes, with a slightly lower pattern frequency of positive height anomalies over northern Europe as well as Siberia and opposing negative anomalies on the opposite side of the hemisphere. But the most notable change is in the patterns in primarily the first column of the master map, which mostly comprises patterns with positive height anomalies over the Greenland side of the Arctic. This suggests that changes in atmospheric circulation have resulted in an increasing frequency in ridging in this part of the Arctic, which has consequences in energy transport and surface conditions in these regions.

Next, SOM analysis was undertaken on the same dataset, but the data were detrended and detrended MAR variables (meltwater production and 2 m temperature) were mapped onto the resulting nodes. The purpose is to show the synoptic patterns that support anomalies in these variables while controlling for the broad observed warming

over this period that has resulted in positive trends in 500 hPa heights, 2 m temperature, and surface melt. The master map of the detrended 500 hPa height field (Fig. 4.15) is slightly different from Fig. 4.13, though the SOM algorithm mapped the nodes in much the same way with positive height anomalies over Greenland in the lefthand columns and negative anomalies in the righthand columns. However, anomalies in Fig. 4.15 are more focused around the pole than at lower latitudes as in Fig. 4.13, which suggests that changes in 500 hPa heights over this time period have been stronger in the lower (60º – 75º N) latitudes of the Arctic.

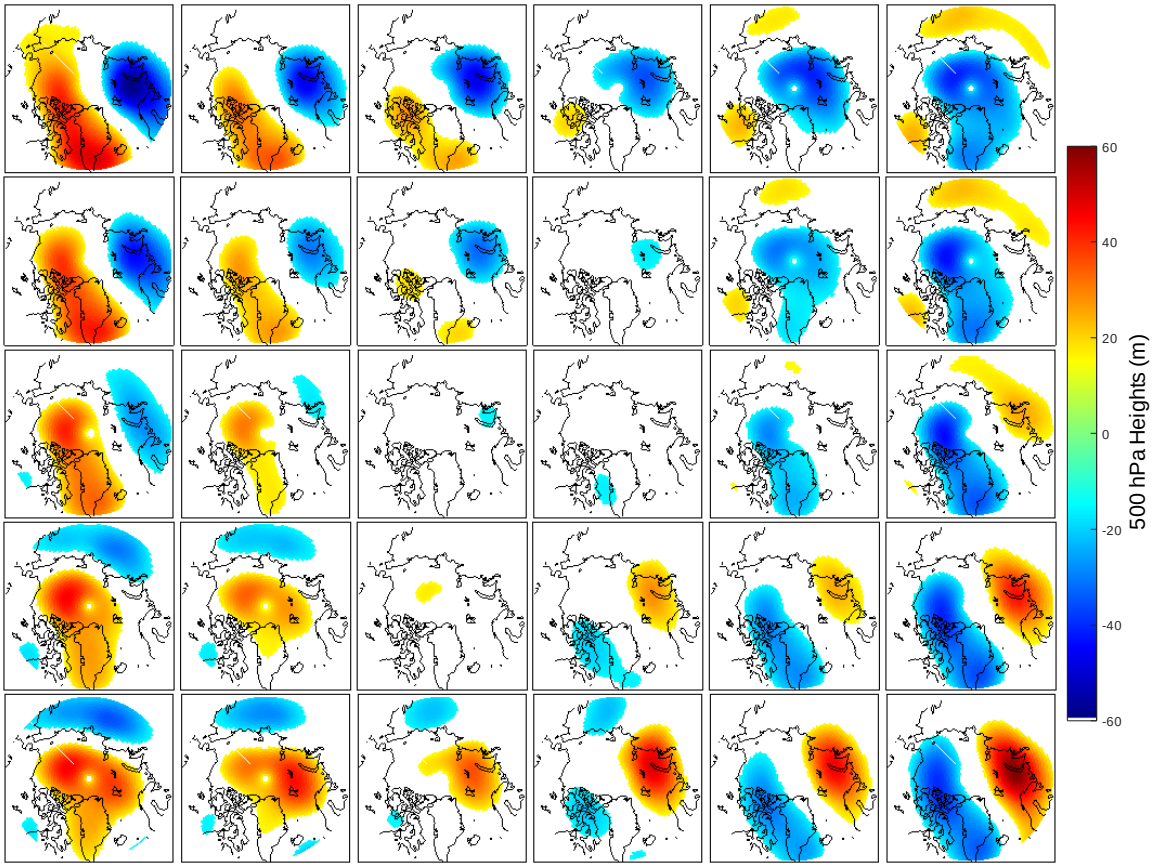

Fig. 4.15) As in Fig. 4.14, but data are detrended.

Temperature anomalies are next mapped onto each node, meaning that the spatial

dataset of temperature anomalies at each date that matches most closely with a given node is averaged together and displayed visually in Fig. 4.16 at the same node position. To first order, temperature anomalies over Greenland follow those in 500 hPa heights, with stronger anomalies in the latter being reflected in the former. There are no apparent patterns that deviate significantly from this such that a certain orientation in the height pattern results in unexpected temperature anomalies.

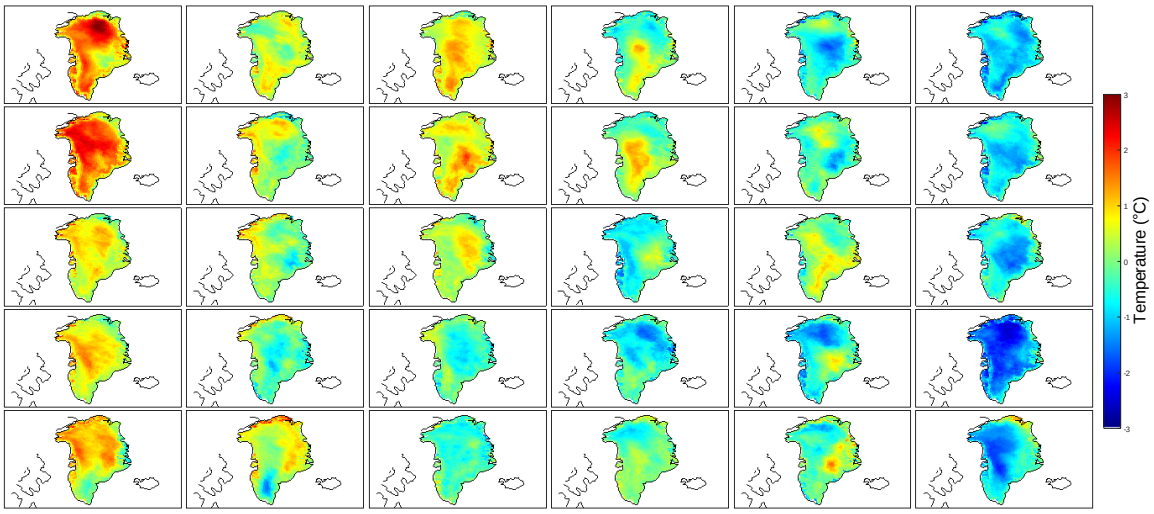

Fig. 4.16) Detrended 2 m temperature anomalies (°C) for JJA associated with each node on the master SOM (Fig. 4.15).

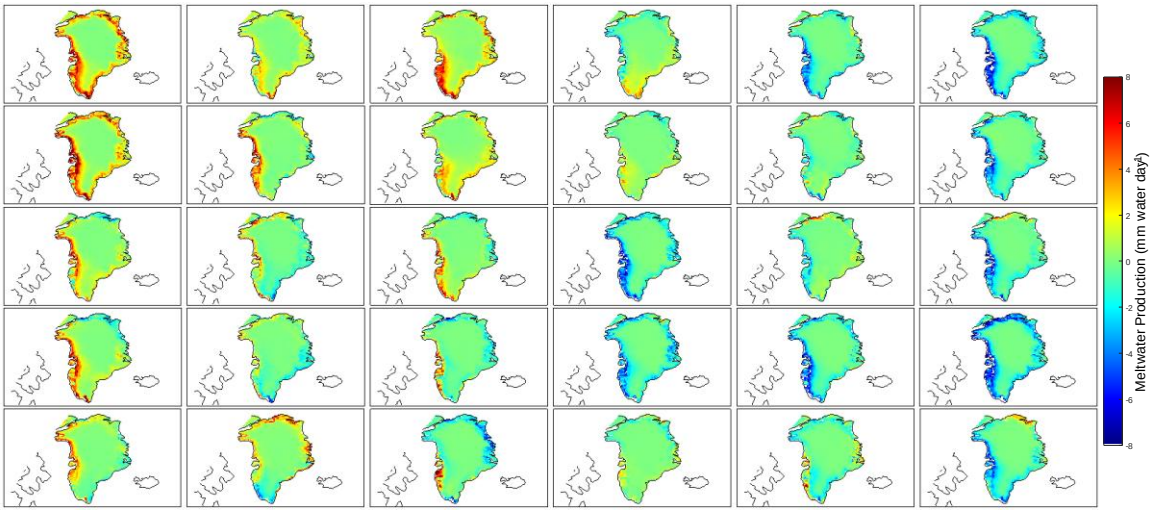

Fig. 4.17) As in Fig. 4.16, but using meltwater production anomalies (mm water day^{-1}).

The same node mapping process was applied to meltwater production (Fig. 4.17). Anomalies again follow 500 hPa height anomalies as well as 2 m temperatures, and typically appear in nodes when there is at least a 1º C temperature anomaly. Meltwater production anomalies are not as high at higher elevations due to the lower overall surface melt that occurs at those colder elevations. However, these anomalies can be seen best in nodes when the temperature anomalies extend or are centered well inland over the ice sheet. Overall, ridging over all of Greenland extending to the Canadian archipelago and Beaufort Sea supports the strongest surface melt anomalies on the ice sheet, while negative height anomalies over the same region are the least conducive to ice sheet melting.

4.8 Discussion and Conclusions

The MOD over sea ice has come several days decade^{-1} sooner since 1979, particularly in the waters adjacent to Greenland. The earlier MOD over Greenland can likely be attributed to a similar atmospheric forcing as the MOD over sea ice, and modes of covariance in a monthly SVD analysis of the 500 hPa geopotential height field confirm that variability in the Greenland MOD is largely explained by regional height anomalies. SIC and GrIS melt demonstrate significant covariability during the summer, particularly June, but this relationship is likely related to the simultaneous forcing of the atmospheric circulation. This relationship is strongest with sea ice in Fram Strait and much of the Beaufort Sea, but can be explained primarily by the positioning of a ridge over and to the

north of Greenland. Analysis over Baffin Bay and the adjacent ice sheet concludes that the covariability can also likely be attributed to circulation anomalies, but there is a compelling signal suggesting a local influence as well. These circulation anomalies are found to have increased in frequency over the study period, and strongly correspond with near-surface temperature and meltwater production anomalies.

Given that all time series are detrended, it is remarkable that the covariance with GrIS surface melt is so strong. If the trend in the data can largely be attributed to greenhouse gas loading and low frequency climate variability, the remaining anomalies likely occur due to synoptic-scale variability or components of the climate system that have remained stationary. By assessing the covariability among these fields while removing the covariability resulting from a warming Arctic, the resulting relationships should either both be responding to atmospheric circulation anomalies, or there is a causal link between SIC and GrIS surface melt.

An analysis of the covariability between the Greenland MOD and the 500 hPa pattern results in consistently significant correlations between EC_{GrIS} and 500 hPa heights over Greenland, very similar to the HC maps in Fig. 4.7 but with slightly weaker correlations. As would be expected, this suggests that the same pattern (i.e. strong ridging over Greenland) is the most conducive to both initiating snow melt and generating atmospheric conditions that result in the most anomalous surface melt events in the summer. The specific positioning of the centers of significant correlation in the second SVD mode are not necessarily physically meaningful, but the observation that correlations in the two HC maps correspond spatially demonstrates that MOD is significantly correlated with regional height anomalies. Although this mode explains

considerably less variance than the leading mode, it provides additional support for this covariance, particularly in May and June when much of the snow in the ablation zone begins to melt.

A significant correlation between Greenland MOD and accumulated meltwater production exists only along the periphery of the ice sheet. The two factors most likely to contribute to this correlation are the persistence of the weather patterns and the albedo feedback. For example, if a pattern can initiate an early MOD and persist into the summer, it will likely generate more accumulated meltwater than in the average year. The early MOD will also theoretically drive the albedo into its lower summer regime at an earlier date, so the albedo feedback may play a greater role in summer melt where this correlation is greater. This is likely to be the case lower in the ablation zone anyway, where the ice surface is typically darker. Analysis of MAR surface albedo (not included here) following the MOD found that the decrease is not always maintained, and relatively often the albedo rises again at some point in the following weeks. This is not surprising because many factors can influence ice sheet albedo, especially early in the season. Variability in albedo is caused by the transition from dry to wet snow and slush formation, snowfall events, refreezing of meltwater, and rainfall (Grenfell and Perovich 2004, Chandler et al. 2015). This provides some explanation for why the significant correlations encompass only a small part of the ice sheet.

The changes in summer SIC are remarkable when plotted on the SOM map and easily juxtaposed with SIC in other years and summer months. It would be very interesting to extend this analysis into the other seasons. Three month periods seem to work well, as incorporating more months would require an increasingly overwhelming

number of nodes to be displayed, and using only one month would in one way defeat the purpose of the SOM analysis (one could simply map the anomalies rather than mathematically approximating them) and it would not be possible to make claims regarding the advancement of one (or even two) months of sea ice loss. Approximately 20% of the monthly data overlap with a different month in another year, representing this one-month advancement in sea ice loss, and this percentage may be greater in other seasons depending on what the primary factors are forcing downward sea ice trends throughout the year.

Comparing these SIC SOM nodes in each month in years earlier in the period to those more recently, it is difficult to determine which regions have exhibited the greatest loss. This type of question is not particularly well suited to SOM analysis but has been addressed using other methodology, finding the greatest trends in the East Siberian Sea, Chukchi Sea, and Beaufort Sea (e.g. Comiso 2008, Stroeve et al. 2012a). However, comparison of individual nodes is possible to determine how the SIC anomaly pattern has shifted throughout the period. For example, SIC anomalies in August have transitioned from a pattern primarily resembling node 22 to node 8. The greatest difference in these nodes is clearly the loss in ice from the Kara Sea east all the way through the Beaufort Sea, consistent with those studies cited above.

Summer ice sheet melt responds to first order to atmospheric circulation anomalies. The Beaufort sea ice correlation with 500 hPA heights suggest that positive sea ice anomalies here are associated with a surface pressure pattern that tends to strengthen the easterlies and circulate sea ice west out of Beaufort Sea, whereas the opposite pattern would push ice into Beaufort Sea and against the Canadian Archipelago.

This mechanism has been identified previously in its ability to transport and melt ice between Beaufort Sea and the East Siberian Sea (Rogers 1978; Maslanik et al. 1999). Additionally, there is no likely mechanism to directly influence GrIS surface melt from such a distance. In Fram Strait, positive correlations between all three fields indicate that this relationship is due to the placement of a ridge circulating sea ice out of Fram Strait while simultaneously bringing positive temperature anomalies to the GrIS. Results from Mills and Walsh (2014) support this, finding that Fram Strait export is significantly correlated with synoptic patterns that feature ridging in this location.

Modeling studies suggest that a reduction in sea ice under scenarios significantly warmer than the current climate would have a large impact on surface temperature and GrIS melt (Lawrence et al. 2008; Koenig et al. 2014), and here we identify western Greenland as the most likely location for a direct influence from sea ice loss. Extreme melt years over this part of the ice sheet are accompanied by strong SIC anomalies that would be expected if this thermodynamic influence were occurring. However, all analysis incorporating 500 hPa height anomalies suggests that the atmospheric circulation is still the first order melt driver in this part of the ice sheet as well. It is not clear why only June in Baffin Bay retains strong correlations after the GBI is removed, but it should not be expected that the correlation would completely disappear given that synoptic variability is not the only driver of surface melt. Western Greenland has previously been identified as the most likely part of the GrIS to be influenced by sea ice loss (Rennermalm et al. 2009), although an analysis of the extreme GrIS melt years from 2007-2012 concluded that sea ice was likely not a factor primarily because Katabatic winds precluded the prerequisite onshore flow (Noël et al. 2014).

Covariance with GrIS surface melt is typically strongest in June. Whereas the atmospheric response to sea ice variability is strongest in autumn and early winter (e.g. Screen and Simmonds 2010; Rinke et al. 2006; Porter et al. 2012) the stronger June response here may be because this is when melt generally begins on the ice sheet, and there is autocorrelation in surface melt throughout the summer largely due to albedo feedbacks. Also, there is less variability in interannual meltwater production over the entire ice sheet in June relative to the rest of the summer, with a standard deviation of 0.84 mm water equivalent day^{-1} compared to 0.95 in August and 1.12 in July. This may also explain why covariance tends to be weakest in July. Among these three variables, it is possible that there is simply more interaction in June.

SOM analysis of daily summer height fields provides an organized way of categorizing and visualizing the summer Arctic atmospheric circulation. This type of analysis has been done previously, particularly in the Arctic, but often uses sea level pressure instead of mid-tropospheric levels (e.g. Cassano et al. 2006; Higgins and Cassano 2009; Schuenemann et al. 2009; Schuenemann and Cassano 2009; Skific et al. 2009; Mills and Walsh 2014). The 500 hPa level was chosen for SOM analysis (and much of the other analysis) because broader patterns are more easily identified in this part of the atmosphere, and surface conditions including temperature, precipitation, wind, and advective processes can be inferred with reasonable accuracy based on the 500 hPa pattern. Additionally, daily data are required for this level of analysis primarily to sufficiently populate each node with a robust sample of dates from which MAR variables can be averaged and mapped. Fitting a given day's 500 hPa map to one of 30 different patterns is not always qualitatively accurate, but averaging over the bin containing all of a

node's dates is sufficient to generate robust results (Hewitson and Crane 2002).

The most interesting results obtained from the undetrended SOM analysis may be the change in node frequency. This may be a result of internal variability which includes low-frequency atmospheric variability, or the effects of climate change that have an uneven impact on Arctic circulation patterns, or both. It also may vary depending on the time periods chosen for subtraction, and the 10-year periods here were only chosen to maximize the difference in time. Furthermore, this specific type of analysis is not possible using more conventional trend analysis, either linear or nonlinear. While it is likely that heat and moisture advection has increased into the Arctic, it is improbable that the response in circulation has been spatially uniform, and the uneven changes identified in Fig. 4.14b may provide evidence for this conclusion.

SOM analysis after detrending shows a similar master map, but the anomalies are focused more around the pole than lower latitudes. The SOM algorithm is designed to capture the range of variability in the dataset, so if the removal of trends in these data results in this type of response, then it is likely that the largest changes in the height field have occurred at the lower latitudes. To my knowledge, latitudinal differences in atmospheric geopotential heights and thicknesses have not been the focus of Arctic amplification studies, but there is no reason to believe that they would be substantial given that this amplification is primarily surface-based (Serreze et al. 2009, Screen and Simmonds 2010, Serreze and Barry 2011). It is also impossible to determine whether this is a significant change in the height field using this type of method, so it is quite possible that this is an observation construed from noise.

Analysis mapping temperature and meltwater production onto the detrended SOM

master map shows that these variables closely follow the synoptic pattern in each node, further strengthening the case for the first order influence of atmospheric forcing. Further analysis with variables such as total column energy convergence and wind direction could be fruitful in identifying the fingerprint of a causal linkage between adjacent open water and ice sheet melt events.

Some of these SOM nodes with ridging over Greenland (in both of the SOM analyses) that map strong anomalies in temperature and meltwater production would be considered to be the negative phase of the Arctic Dipole (AD) pattern and/or negative North Atlantic Oscillation, which have been linked to recent records in sea ice loss (Overland and Wang 2010) and GrIS surface melt (van Angelen et al. 2013), respectively. Going forward, continued Arctic amplification will theoretically produce high amplitude weather patterns and enhanced ridging resulting from the decreased latitudinal temperature gradient (Francis and Vavrus 2012, 2015). Given these recent and projected trends in the Arctic atmospheric circulation, we would expect to see continued enhancement of warming in the vicinity of Greenland, including the potential for more persistent patterns such as the anomalous ridging which contributed to the record July 2012 GrIS surface melt (Nghiem et al. 2012).

Recent trends in multiple components of the Arctic climate system, including increased poleward heat advection, enhanced ice-albedo feedback, warmer upper ocean temperatures, and warm boundary layer temperatures have converged to generate accelerated trends in Arctic sea ice loss and GrIS surface melt (Box et al. 2012; Polyakov et al. 2012; Stroeve et al. 2012a; Fettweis et al. 2011b). Results here have shown that atmospheric circulation anomalies are responsible for the majority of variability in GrIS

surface melt throughout the summer months, as well as much of the covariability with sea ice concentration, but this does not preclude some thermodynamic influence from sea ice loss. While there is a large spread in future sea ice projections (Overland and Wang 2013; Stroeve et al. 2012b), continued decline in the vicinity of Greenland, particularly Baffin Bay, should present further opportunities for local enhancement of summer ice sheet melt. The rate of future sea ice and ice sheet melt will likely depend most on the evolution of Arctic circulation patterns, but the increasingly ice-free ocean should be observed for a potentially increased role in GrIS surface melt.

References

Alexander, P. M., M. Tedesco, X. Fettweis, R. S. W. van de Wal, C. J. P. P. Smeets, and M. R. van den Broeke, 2014: Assessing spatio-temporal variability and trends in modelled and measured Greenland Ice Sheet albedo (2000–2013). *Cryosph.*, **8**, 2293–2312, doi:10.5194/tc-8-2293-2014.

van Angelen, J. H., M. R. van den Broeke, B. Wouters, and J. T. M. Lenaerts, 2013: Contemporary (1960–2012) Evolution of the Climate and Surface Mass Balance of the Greenland Ice Sheet. *Surv. Geophys.*, **35**, 1155–1174, doi:10.1007/s10712-013-9261-z.

Appenzeller, C., J. Schwander, S. Sommer, and T. F. Stocker, 1998: The North Atlantic Oscillation and its imprint on precipitation and ice accumulation in Greenland. *Geophys. Res. Lett.*, **25**, 1939–1942.

Belchansky, G., D. Douglas, and N. Platonov, 2004: Duration of the Arctic sea ice melt season: Regional and interannual variability, 1979-2001. *J. Clim.*, **67**, 67–80.

Bitz, C. M., and W. H. Lipscomb, 1999: An energy-conserving thermodynamic model of sea ice. *J. Geophys. Res.*, **104**, 15669, doi:10.1029/1999JC900100.

Björnsson, H., and S. Benegas, 1997: *Analyses of Climatic Data A Manual for EOF and SVD Analyses of Climatic Data*. CCGCR Report No. 97-1. McGill University, Montreal.

Bosilovich, M. G., F. R. Robertson, and J. Chen, 2011: Global Energy and Water Budgets in MERRA. *J. Clim.*, **24**, 5721–5739, doi:10.1175/2011JCLI4175.1.

Box, J. E., X. Fettweis, J. C. Stroeve, M. Tedesco, D. K. Hall, and K. Steffen, 2012: Greenland ice sheet albedo feedback: thermodynamics and atmospheric drivers. *Cryosph.*, **6**, 821–839, doi:10.5194/tc-6-821-2012.

Bretherton, Christophers; Smith, Catherine; Wallace, J. M., 1992: An intercomparison of methods for finding coupled patterns in climate data. *J. Clim.*, **5**, 541–560.

van den Broeke, M., and Coauthors, 2009: Partitioning recent Greenland mass loss. *Science*, **326**, 984–986, doi:10.1126/science.1178176.

Brun, E., David, P., Sudul, M., and G. Brunot, 1992: A numerical model to simulate snow-cover stratigraphy for operational avalanche forecasting. *J. Glaciol.*, **38**, 13–22.

Cassano, E. N., J. J. Cassano, M. E. Higgins, and M. C. Serreze, 2014: Atmospheric impacts of an Arctic sea ice minimum as seen in the Community Atmosphere Model. *Int. J. Climatol.*, **34**, 766–779, doi:10.1002/joc.3723.

Cassano, J. J., P. Uotila, and A. Lynch, 2006: Changes in synoptic weather patterns in the polar regions in the twentieth and twenty-first centuries, part 1: Arctic. *Int. J. Clim.*, **1049**, 1027–1049, doi:10.1002/joc.1306.

Chapman McGrew, J., Lembo, A. J. and C.B. Monroe, 2014: An Introduction to Statistical Problem Solving in Geography, 3rd ed., Waveland Press, Inc.

Chandler, D. M., J. D. Alcock, J. L. Wadham, S. L. Mackie, and J. Telling, 2015: Seasonal changes of ice surface characteristics and productivity in the ablation zone of the Greenland Ice Sheet. *Cryosph.*, **9**, 487–504, doi:10.5194/tc-9-487-2015.

Cavalieri, D., C. Parkinson, P. Gloersen, and H. J. Zwally, 1996, updated 2008: Sea Ice Concentrations from Nimbus-7 SMMR and DMSP SSM/I Passive Microwave Data, [1979-2013]. Boulder, Colorado USA: National Snow and Ice Data Center. Digital media.

Cavalieri, D. J., and C. L. Parkinson, 2012: Arctic sea ice variability and trends, 1979–2010. *Cryosph.*, **6**, 881–889, doi:10.5194/tc-6-881-2012.

Comiso, J. C., 2012: Large Decadal Decline of the Arctic Multiyear Ice Cover. *J. Clim.*, **25**, 1176–1193, doi:10.1175/JCLI-D-11-00113.1.

Cullather, R. I., and M. G. Bosilovich, 2011a: The Energy Budget of the Polar Atmosphere in MERRA. *J. Clim.*, **25**, 5–24, doi:10.1175/2011JCLI4138.1.

——, and ——, 2011b: The Moisture Budget of the Polar Atmosphere in MERRA. *J. Clim.*, **24**, 2861–2879, doi:10.1175/2010JCLI4090.1.

Day, J. J., J. L. Bamber, and P. J. Valdes, 2013: The Greenland Ice Sheet's surface mass balance in a seasonally sea ice-free Arctic. *J. Geophys. Res. Earth Surf.*, **118**, 1533–1544, doi:10.1002/jgrf.20112.

De Ridder, K., and H. Gallée, 1998: Land surface-induced regional climate change in southern Israel. *J. Appl. Meteorol.*, **37**, 1470-1485.

Deser, C., J. E. Walsh, and M. S. Timlin, 2000: Arctic Sea Ice Variability in the Context of Recent Atmospheric Circulation Trends. *J. Clim.*, **13**, 617–633.

Fang Z-F, 2004: Statistical relationship between the northern hemisphere sea ice and atmospheric circulation during wintertime. In Observation, Theory and Modeling of Atmospheric Variability. Zhu X (ed.). World Scientific Series on Meteorology of East Asia. World Scientific Publishing Company: Singapore, 131–141.

Fettweis, X., Gallée, H., Lefebre, F., and J.-P. van Ypersele, 2005: Greenland surface mass balance simulated by a regional climate model and comparison with satellite-derived data in 1990-1991. *Clim. Dyn.*, **24**, 623-640. doi:10.1007/s00382-005-0010-y.

——, M. Tedesco, M. van den Broeke, and J. Ettema, 2011a: Melting trends over theGreenland ice sheet (1958–2009) from spaceborne microwave data and regional climate models, *Cryosph.*., 5, 359-375.

——, Mabille, G., Erpicum, M., Nicolay, S., and M. van den Broeke, 2011b: The 1958–2009 Greenland ice sheet surface melt and the mid-tropospheric atmospheric circulation. *Clim. Dyn.* **36**, 139-159. doi:10.1007/s00382-010-0772-8.

Fettweis, X., E. Hanna, C. Lang, a. Belleflamme, M. Erpicum, and H. Gallée, 2013: *Brief communication* "Important role of the mid-tropospheric atmospheric circulation in the recent surface melt increase over the Greenland ice sheet." *Cryosph.*, **7**, 241–248, doi:10.5194/tc-7-241-2013.

Francis, J. A, and S. J. Vavrus, 2015: Evidence for a wavier jet stream in response to rapid Arctic warming. *Environ. Res. Lett.*, **10**, 014005, doi:10.1088/1748-9326/10/1/014005.

——, W. Chan, D. J. Leathers, J. R. Miller, and D. E. Veron, 2009: Winter Northern Hemisphere weather patterns remember summer Arctic sea-ice extent. *Geophys. Res. Lett.*, **36**, L07503, doi:10.1029/2009GL037274.

Gallée, H., and G. Schayes, 1994: Development of a three-dimensional meso-γ primitive equation model – katabatic winds simulation in the area of Terra-Nova Bay, Antarctica. *Mon. Wea. Rev.*, **122**, 671-685.

Gallée H., Peyaud V., and I. Goodwin, 2005: Simulation of the net snow accumulation along the Wilkes Land transect, Antarctica, with a regional climate model. *Ann. Glac.*, **41**,17-22.

Ghatak, D., A. Frei, G. Gong, J. Stroeve, and D. Robinson, 2010: On the emergence of an Arctic amplification signal in terrestrial Arctic snow extent. *J. Geophys. Res.*, **115**, D24105, doi:10.1029/2010JD014007.

Grenfell, T. C., and D. K. Perovich, 2004: Seasonal and spatial evolution of albedo in a snow-ice-land-ocean environment. *J. Geophys. Res.*, **109**, C01001, doi:10.1029/2003JC001866.

Hanna, E., and Coauthors, 2008: Increased Runoff from Melt from the Greenland Ice Sheet: A Response to Global Warming. *J. Clim.*, **21**, 331–341, doi:10.1175/2007JCLI1964.1.

——, Jones JM, Cappelen J, Mernild SH, Wood L, Steffen K, and P. Huybrechts, 2012: The influence of North Atlantic atmospheric and oceanic forcing effects on 1900–2010 Greenland summer climate and ice melt/runoff. *Int. J. Climatol.* **33**, 862-880. doi:10.1002/joc.3475.

——, J. M. Jones, J. Cappelen, S. H. Mernild, L. Wood, K. Steffen, and P. Huybrechts, 2013: The influence of North Atlantic atmospheric and oceanic forcing effects on 1900-2010 Greenland summer climate and ice melt/runoff. *Int. J. Climatol.*, **33**, 862–880, doi:10.1002/joc.3475.

——, and Coauthors, 2014: Atmospheric and oceanic climate forcing of the exceptional Greenland ice sheet surface melt in summer 2012. *Int. J. Climatol.*, **34**, 1022–1037, doi:10.1002/joc.3743.

Hewitson, B., and R. Crane, 2002: Self-organizing maps: applications to synoptic climatology. *Clim. Res.*, **22**, 13–26.

Higgins, M. E., and J. J. Cassano, 2009: Impacts of reduced sea ice on winter Arctic atmospheric circulation, precipitation, and temperature. *J. Geophys. Res.*, **114**, D16107, doi:10.1029/2009JD011884.

Kay, J. E., K. Raeder, a. Gettelman, and J. Anderson, 2011: The Boundary Layer Response to Recent Arctic Sea Ice Loss and Implications for High-Latitude Climate Feedbacks. *J. Clim.*, **24**, 428–447, doi:10.1175/2010JCLI3651.1.

Kennedy, A. D., X. Dong, B. Xi, S. Xie, Y. Zhang, and J. Chen, 2011: A Comparison of MERRA and NARR Reanalyses with the DOE ARM SGP Data. *J. Clim.*, **24**, 4541–4557, doi:10.1175/2011JCLI3978.1.

Kohonen, T., 2001: Self-organizing maps, Springer, Berlin.

Koenig, S. J., R. M. Deconto, and D. Pollard, 2014: Impact of reduced Arctic sea ice on Greenland ice sheet. *Geophys. Res. Lett.*, **41**, 3934–3943, doi:10.1002/2014GL059770.A.

Lawrence, D. M., A. G. Slater, R. a. Tomas, M. M. Holland, and C. Deser, 2008: Accelerated Arctic land warming and permafrost degradation during rapid sea ice loss. *Geophys. Res. Lett.*, **35**, L11506, doi:10.1029/2008GL033985.

Laxon, S. W., and Coauthors, 2013: CryoSat-2 estimates of Arctic sea ice thickness and volume. *Geophys. Res. Lett.*, **40**, 732–737, doi:10.1002/grl.50193.

Lefebre, F., Gallée, H., van Ypersele, J.P., and W. Greuell, 2003: Modeling of snow and ice melt at ETH-Camp (West Greenland): A study of surface albedo. *J. Geophys. Res.*, **108**, doi:10.1029/2001JD001160.

Lefebre, F., Fettweis, X., Galée, H., van Ypersele, J.-P., Marbaix, P., Greuell, W., and P. Calanca, 2005: Evaluation of a high-resolution regional climate simulation over Greenland. *Clim. Dyn.*, **25**, 99-116. doi:10.1007/s00382-005-0005-8.

Lindsay, R., M. Wensnahan, a. Schweiger, and J. Zhang, 2014: Evaluation of Seven Different Atmospheric Reanalysis Products in the Arctic*. *J. Clim.*, **27**, 2588–2606, doi:10.1175/JCLI-D-13-00014.1.

Markus, T., and D. J. Cavalieri, 2000: An Enhancement of the NASA Team Sea Ice Algorithm. *IEEE Trans. Geosci. Remote Sens.*, **38**, 1387–1398.

——, J. C. Stroeve, and J. Miller, 2009: Recent changes in Arctic sea ice melt onset, freezeup, and melt season length. *J. Geophys. Res.*, **114**, C12024, doi:10.1029/2009JC005436.

Maslanik, J. a., M. C. Serreze, and T. Agnew, 1999: On the record reduction in 1998 western Arctic Sea-ice cover. *Geophys. Res. Lett.*, **26**, 1905–1908, doi:10.1029/1999GL900426.

Meier, W., 2005: Comparison of passive microwave ice concentration algorithm retrievals with AVHRR imagery in Arctic peripheral seas. *IEEE Trans. Geosci. Remote Sens.*, **43**, 1324–1337.

——, and J. Stroeve, 2008: Comparison of sea-ice extent and ice-edge location estimates from passive microwave and enhanced-resolution scatterometer data. *Ann. Glaciol.*, **48**, 65–70.

Mernild, S. H., T. L. Mote, and G. E. Liston, 2011: Greenland ice sheet surface melt extent and trends: 1960–2010. *J. Glaciol.*, **57**, 621–628, doi:10.3189/002214311797409712.

Mills, C. M., and J. E. Walsh, 2014: Synoptic Activity Associated with Sea Ice Variability in the Arctic. *J. Geophys. Res. Atmos.*, **119**, 12,117–12,131,

doi:10.1002/2014JD021604.

Mosley-Thompson, E., C. R. Readinger, P. Craigmile, L. G. Thompson, and C. A. Calder, 2005: Regional sensitivity of Greenland precipitation to NAO variability. *Geophys. Res. Lett.*, **3**, doi:10.1029/2005GL024776.

Mote, T. L., 2007: Greenland surface melt trends 1973-2007: Evidence of a large increase in 2007. *Geophys. Res. Lett.*, **34**, doi:10.1029/2007GL031976.

Nghiem, S. V., and Coauthors, 2012: The extreme melt across the Greenland ice sheet in 2012. *Geophys. Res. Lett.*, **39**, n/a–n/a, doi:10.1029/2012GL053611.

Noël, B., X. Fettweis, W. J. van de Berg, M. R. van den Broeke, and M. Erpicum, 2014: Small impact of surrounding oceanic conditions on 2007–2012 Greenland Ice Sheet surface mass balance. *Cryosph.*, **8**, 1453–1477, doi:10.5194/tcd-8-1453-2014.

Overland, J. E., and M. Wang, 2010: Large-scale atmospheric circulation changes are associated with the recent loss of Arctic sea ice. *Tellus A*, **62**, 1–9, doi:10.1111/j.1600-0870.2009.00421.x.

——, and ——, 2013: When will the summer Arctic be nearly sea ice free? *Geophys. Res. Lett.*, **40**, 2097–2101, doi:10.1002/grl.50316.

Polyakov, I. V., J. E. Walsh, and R. Kwok, 2012: Recent Changes of Arctic Multiyear Sea Ice Coverage and the Likely Causes. *Bull. Am. Meteorol. Soc.*, **93**, 145–151, doi:10.1175/BAMS-D-11-00070.1.

Porter, D. F., J. J. Cassano, and M. C. Serreze, 2012: Local and large-scale atmospheric responses to reduced Arctic sea ice and ocean warming in the WRF model. *J. Geophys. Res.*, **117**, 1–21, doi:10.1029/2011JD016969.

Reichle, R. H., R. D. Koster, G. J. M. De Lannoy, B. a. Forman, Q. Liu, S. P. P. Mahanama, and A. Touré, 2011: Assessment and Enhancement of MERRA Land Surface Hydrology Estimates. *J. Clim.*, **24**, 6322–6338, doi:10.1175/JCLI-D-10-05033.1.

Rennermalm, A. K., L. C. Smith, J. C. Stroeve, and V. W. Chu, 2009: Does sea ice influence Greenland ice sheet surface-melt? *Environ. Res. Lett.*, **4**, 024011, doi:10.1088/1748-9326/4/2/024011.

Reusch, D. B., and R. B. Alley, 2007: Antarctic sea ice: a self-organizing map-based perspective. *Ann. Glaciol.*, **46**, 391–396, doi:10.3189/172756407782871549.

Rienecker, M. M., and Coauthors, 2011: MERRA - NASA's Modern-Era Retrospective Analysis for Research and Applications. *J. Clim.*, **24**, 3624–3648, doi:10.1175/JCLI-D-11-00015.1.

Rignot, E., I. Velicogna, M. R. van den Broeke, a. Monaghan, and J. Lenaerts, 2011: Acceleration of the contribution of the Greenland and Antarctic ice sheets to sea level rise. *Geophys. Res. Lett.*, **38**, 1–5, doi:10.1029/2011GL046583.

Rigor, I. G., J. M. Wallace, and R. L. Colony, 2002: Response of Sea Ice to the Arctic Oscillation. *J. Clim.*, **15**, 2648-2663.

Rinke, A., W. Maslowski, K. Dethloff, and J. Clement, 2006: Influence of sea ice on the atmosphere: A study with an Arctic atmospheric regional climate model. *J. Geophys. Res.*, **111**, D16103, doi:10.1029/2005JD006957.

Robertson, F. R., M. G. Bosilovich, J. Chen, and T. L. Miller, 2011: The Effect of Satellite Observing System Changes on MERRA Water and Energy Fluxes. *J. Clim.*, **24**, 5197–5217, doi:10.1175/2011JCLI4227.1.

Robinson, David A., Mark R. Anderson, Thomas W. Estilow, Dorothy K. Hall, and Thomas L. Mote, 2014: MEaSUREs Northern Hemisphere State of Cryosphere Daily 25km EASE-Grid 2.0, [Greenland Melt Onset]. Boulder, Colorado USA: NASA DAAC at the National Snow and Ice Data Center.doi: http://dx.doi.org/10.5067/MEASURES/CRYOSPHERE/nsidc-0534.001.

Rogers. J.C. (1978), Meteorological factors affecting interannual variability of summertime ice extent in the Beaufort Sea. *Mon. Wea. Rev.*, **106**, 890-897.

Schröder, D., D. L. Feltham, D. Flocco, and M. Tsamados, 2014: September Arctic sea-ice minimum predicted by spring melt-pond fraction. *Nat. Clim. Chang.*, **4**, 353–357, doi:10.1038/nclimate2203.

Schuenemann, K. C., and J. Cassano, 2009: Changes in synoptic weather patterns and Greenland precipitation in the 20th and 21st centuries: 1. Evaluation of late 20th century simulations from IPCC models. *J. Geophys. Res.*, **114**, doi:10.1029/2009JD011705.

Schuenemann, K. C., J. J. Cassano, and J. Finnis, 2009: Synoptic Forcing of Precipitation over Greenland: Climatology for 1961–99. *J. Hydrometeorol.*, **10**, 60–78, doi:10.1175/2008JHM1014.1.

Screen, J. a, and I. Simmonds, 2010: The central role of diminishing sea ice in recent Arctic temperature amplification. *Nature*, **464**, 1334–1337, doi:10.1038/nature09051.

Serreze, M. C., and R. G. Barry, 2011: Processes and impacts of Arctic amplification: A research synthesis. *Glob. Planet. Change*, **77**, 85–96, doi:10.1016/j.gloplacha.2011.03.004.

Serreze, M. C., A. P. Barrett, J. C. Stroeve, D. N. Kindig, and M. M. Holland, 2009: The emergence of surface-based Arctic amplification. *Cryosph.*, **3**, 11–19.

Skific, N., J. a. Francis, and J. J. Cassano, 2009: Attribution of Projected Changes in Atmospheric Moisture Transport in the Arctic: A Self-Organizing Map Perspective. *J. Clim.*, **22**, 4135–4153, doi:10.1175/2009JCLI2645.1.

Smith, D., 1998: Recent increase in the length of the melt season of perennial Arctic sea ice. *Geophys. Res. Lett.*, **25**, 655–658.

Stammerjohn, S., R. Massom, D. Rind, and D. Martinson, 2012: Regions of rapid sea ice change: An inter-hemispheric seasonal comparison. *Geophys. Res. Lett.*, **39**, L06501, doi:10.1029/2012GL050874.

Stroeve, J., T. Markus, W. Meier, and J. Miller, 2006: Recent changes in the Arctic melt season. *Ann. Glaciol.*, **44**, 367-374.

——, A. Frei, J. Mccreight, and D. Ghatak, 2008: Arctic sea-ice variability revisited. *Ann. Glaciol.*, **48**, 71–81.

——, M. C. Serreze, A. Barrett, and D. N. Kindig, 2011: Attribution of recent changes in autumn cyclone associated precipitation in the Arctic. *Tellus A*, **63**, 653–663, doi:10.1111/j.1600-0870.2011.00515.x.

——, M. C. Serreze, M. M. Holland, J. E. Kay, J. Malanik, and A. P. Barrett (2012a), The Arctic's rapidly shrinking sea ice cover: a research synthesis, *Clim. Change*, *110*(3-4), 1005–1027, doi:10.1007/s10584-011-0101-1.

——, V. Kattsov, A. Barrett, M. Serreze, T. Pavlova, M. Holland, and W. N. Meier, 2012b: Trends in Arctic sea ice extent from CMIP5, CMIP3 and observations. *Geophys. Res. Lett.*, **39**, n/a–n/a, doi:10.1029/2012GL052676.

Tedesco, M., M. Serreze, and X. Fettweis, 2008: Diagnosing the extreme surface melt event over southwestern Greenland in 2007. *Cryos. Dis.* **2**, 383–397.

——, M. Brodzik, R. Armstrong, M. Savoie, and J. Ramage, 2009: Pan arctic terrestrial snowmelt trends (1979–2008) from spaceborne passive microwave data and correlation with the Arctic Oscillation. *Geophys. Res. Lett.*, **36**, 1–6, doi:10.1029/2009GL039672.

——, X. Fettweis, M. R. van den Broeke, R. S. W. van de Wal, C. J. P. P. Smeets, W. J. van de Berg, M. C. Serreze, and J. E. Box, 2011: The role of albedo and accumulation in the 2010 melting record in Greenland. *Environ. Res. Lett.*, **6**, 014005, doi:10.1088/1748-9326/6/1/014005.

——, X. Fettweis, T. Mote, J. Wahr, P. Alexander, J. E. Box, and B. Wouters, 2013: Evidence and analysis of 2012 Greenland records from spaceborne observations, a regional climate model and reanalysis data. *Cryosph.*, **7**, 615–630, doi:10.5194/tc-7-615-2013.

Zib, B. J., X. Dong, B. Xi, and A. Kennedy, 2012: Evaluation and Intercomparison of Cloud Fraction and Radiative Fluxes in Recent Reanalyses over the Arctic Using BSRN Surface Observations. *J. Clim.*, **25**, 2291–2305, doi:10.1175/JCLI-D-11-00147.1.

Chapter 5: Conclusions and Future Work

5.1 Summary and General Conclusions

The date of snow melt onset (MOD) across the high latitudes of the terrestrial Northern Hemisphere has advanced by 1-2 weeks since 1979, and appears to be controlled by relatively different processes regionally. This attribution can be broadly split into regions where the MOD occurs earlier (March and April) and later (May and June). In the former, the primary melt driver is energy advection due to weaker radiative fluxes, and this results in greater interannual variability in this date. Where melt begins later in the season, there is less variability in the MOD date due to a stronger insolation control with less energy available to be transported from the south (due to a smaller hemispheric energy gradient by May and June). Similarly, this pattern is also found in trends in the observed energy balance terms: as MOD comes sooner, there is less energy available within the atmosphere and more advected from elsewhere. A major implication of these results is that as snow melt occurs earlier in the spring, the dominant melt drivers may shift more toward advective mechanisms depending on corresponding regional changes in atmospheric circulation.

Across a more focused study region in northern Canada, analysis of the energy balance around the MOD provides similar findings. Where melt begins later, there is more energy in the system further northeast by May and June with a greater proportion coming from shortwave radiation than energy advection. Across the southwestern part of the region in the boreal forest, the lower overall energy earlier in the season requires

synoptic events and associated energy transport to provide the energy to initiate the melt season. Melt onset also requires a greater increase in surface temperature to reach freezing in the boreal forest, as the mean temperature is lower just prior to the MOD.

This research on terrestrial snow melt onset attribution has added to the literature and understanding of what is behind the earlier snowmelt while better elucidating regional differences (including why we find these differences). This has gone beyond simply attributing earlier melt to a warming boundary layer by identifying the most important factors in initiating this process as well the warmer temperatures that are associated with it. However, the uncertainty that remains in the observed and future variability of snow melt from onset to disappearance requires further study, particularly considering this study has only focused on the melt onset date.

The MOD over sea ice has come several days decade^{-1} sooner since 1979, particularly in the waters adjacent to Greenland. The earlier MOD over Greenland can likely be attributed to a similar atmospheric forcing as the MOD over sea ice. SIC and GrIS melt demonstrate significant covariability during the summer, particularly June, and this relationship is likely related to the simultaneous forcing of the atmospheric circulation. This relationship is strongest with sea ice in Fram Strait and much of the Beaufort Sea, but can be explained primarily by the positioning of a ridge over and to the north of Greenland. Analysis over Baffin Bay and the adjacent ice sheet concludes that the covariability can also likely be attributed to circulation anomalies, but there is a compelling signal suggesting a local influence as well. Synoptic patterns featuring a ridge over Greenland and north and west to the Beaufort Sea are found to have increased in frequency over the study period, and strongly correspond with near-surface temperature

and meltwater production anomalies over Greenland.

In the same way that the atmosphere is responsible for variability in melt onset over land, there are similar processes at work driving the melt onset of snow over sea ice and the GrIS. Attribution of melt onset over these surfaces is much less the focus of the remainder of this project than a more large-scale analysis of the interactions of these different cryospheric and climate components that generate melt in the spring and the summer. These interactions are particularly a consideration in the vicinity of Greenland, where trends appear the strongest. While there is likely not a large influence of sea ice loss on Greenland melt in the current climate, this research has shown that there is covariance in ways such that some of these fields (i.e. Greenland melt and regional sea ice variability) are responding to the same forcing. This is significant because these regions have not previously been identified within the context of their relationship with the Greenland surface climate. Furthermore, both sea ice and the GrIS have undergone significant changes over the study period, and the analysis with detrended data has worked to identify causal relationships that operate outside the context of a warming Arctic. An improved understanding of these relationships can then be incorporated into our knowledge of how the Arctic system is interacting and evolving to potentially improve future climate and GrIS mass balance projections.

5.2 Specific Findings

An energy balance analysis of snow melt onset across much of the northern hemisphere revealed the following:

1) The melt onset date of terrestrial snow cover has advanced by 1-2 weeks in the 1979-2012 time period across much of the Northern Hemisphere, with the strongest trends in northern and western Eurasia. In these regions, an increasing amount of advective energy is replacing decreasing levels of many other forcing variables associated with an earlier MOD.

2) Large differences in forcing variables at MOD generally follow the spatial pattern of melt timing, with weaker radiative fluxes and colder mean 2 m temperatures where MOD occurs earlier, though a greater magnitude of energy convergence (EC). This pattern is also found in trends: as MOD comes sooner, there is less energy in the system and more advected from elsewhere.

3) The MOD is less variable farther north and relies less on EC and more on radiative fluxes (insolation as well as LW radiation generated from higher atmospheric thicknesses and water vapor). Conversely, inter-annual MOD variability is larger farther south in regions that receive more outside energy.

4) Linear regression and PCA analysis show that the strongest predictors of early (late) MOD anomalies are positive (negative) anomalies of atmospheric thicknesses, water vapor, and consequently downward LW radiation and 2 m temperature. Secondary to this, positive (negative) anomalies of EC are associated with early (late) MOD anomalies in many regions and regression coefficients are of similar magnitude to those of the first principal component across southern Eurasia in particular.

5) Regional differences in EC are substantial. Compared to other regions, southern and western Eurasia and southern North America stand out. Here, EC increases more to a higher peak prior to MOD, is more of an anomaly relative to DOY, and is more variable

from day to day. This suggests that EC is a much more important melt driver in these regions than in northern Eurasia and northern North America.

6) There is little difference regionally in cloud cover at MOD from MERRA variables and slightly less in earlier melting regions. There is also no significant change over the study period in cloud cover and a decrease in some regions in water vapor, and often a decrease in cloud cover just prior to MOD.

Across a study region in northern Canada west of Hudson Bay, results were similar:

1) There is more energy in the system further northeast to initiate melt by May and June. This is from a greater proportion of SW radiation (closer to the solstice) rather than energy being advected into the atmosphere. This contrasts with less overall energy and lower temperatures to the southwest, requiring synoptic events and associated energy transport to provide the energy to initiate the primary melt season as well as the more frequent early melt events observed here.

2) Sources of melt energy vary within the study region, with more energy typically being transported into Regions 1 and 2, a larger proportion from insolation in Region 2 and more from longwave radiation derived from cloud cover and moisture in Region 3.

3) There is a greater increase in temperature to reach the freezing point in Region 1 prior to MOD, but temperature anomalies do not serve as a reliable predictor for MOD anomalies across the region.

Finally, studying the melt onset over sea ice, Greenland, and connections and covariability between summer SIC and GrIS meltwater production, the following

conclusions can be made:

1) Regions of covariability between sea ice and GrIS surface melt are likely mostly due to a simultaneous atmospheric forcing. The Beaufort Sea correlation with 500 hPA heights suggest that negative sea ice anomalies here are associated with a surface pressure pattern that tends to strengthen the easterlies and circulate sea ice west out of Beaufort Sea, whereas the opposite pattern would generate positive ice anomalies here. In Fram Strait, results indicate that the observed relationship is due to the placement of a ridge circulating sea ice out of Fram Strait while simultaneously bringing positive temperature anomalies to the GrIS.

2) Western Greenland is the most likely location to experience a direct influence from sea ice loss, though analysis incorporating synoptic variability still points to a first-order atmospheric influence.

3) Covariance between SIC and GrIS surface melt is typically strongest in June, though it is unclear why this covariance weakens as the summer progresses.

4) A significant correlation exists between Greenland MOD and the summer's accumulated meltwater production along the periphery of the ice sheet. MOD over Greenland is likely not a good predictor of the summer's surface melt on most parts of the ice sheet, however, due to complexity involving the ensuing surface albedo and persistence of circulation patterns.

5) There are consistently significant correlations between the Greenland MOD and

the 500 hPa pattern which look very similar to those between GrIS meltwater production and the same pattern. This suggests that anomalous ridging over Greenland is the most conducive to both initiating snow melt and generating atmospheric conditions that result in the most anomalous surface melt events in the summer.

6) Summer SIC has changed in the last 35 years to the extent that there are multiple instances when the seasonal loss of sea ice has advanced an entire month relative to earlier in the study period. The locations of greatest loss can be observed by comparing nodes on the SOM map, and are found from the Kara Sea east all the way through the Beaufort Sea.

7) Results obtained from SOM analysis using undetrended data show that 500 hPa height patterns featuring strongly positive height anomalies near Greenland have increased between the first and last 10-year period of record, with little change in any other synoptic pattern. Using this analysis, however, it is difficult to determine whether the strength of these height anomalies has increased as well.

8) Analysis mapping temperature and meltwater production anomalies onto the detrended SOM master map shows that these variables closely follow the synoptic pattern in each node, further strengthening the case for the first order influence of atmospheric forcing.

5.3 Future Work - Overview

It is still possible to improve and expand on the research in this dissertation, some of which can be done with the same resources and some that require better observation networks and data processing power. Here, I detail parts of this research where there is

room for improvement, the logical extension of some of the research done, and two specific research projects that would further understanding in these fields.

The most obvious improvements that could be made in this field using the type of data and methods I have are increases in data resolution, particularly spatial. Reanalysis products and remote sensing observations are constrained to their current resolutions by computing limitations, data storage and distribution, past sensor specifications, and the inherent risks in interpolating already-sparse surface and upper air observation. MERRA is run at a relatively high resolution for a global reanalysis product, but this resolution for reanalysis products in general is not improving quickly for the above reasons; MERRA 2 has currently just been released as a significant update to MERRA but is run at the same resolution, 7 years after MERRA's release.

On the user end, improved spatial resolution is accompanied by the same issues: data acquisition, storage, and analysis requires exponentially more computing resources. The primary benefit of improved spatial resolution is that it would allow more analysis near the coast and in mountainous regions, which were left out of some of these analyses for this reason. For a proposed study of similar nature as undertaken here, but more comprehensive in area or at higher resolution, a computing cluster becomes increasingly necessary. This should be no obstacle in undertaking a project, but it should be a consideration when proposing it.

Temporal resolution is another area of improvement, and this is primarily on the user end because reanalysis data is typically computed at time steps as low as 30 minutes. The data for these analyses were obtained at hourly resolution but were immediately aggregated to daily, and sometimes even monthly. Daily averages are suitable for many

types of analyses done, and in fact these analyses were chosen with the understanding that daily data were being used. However, some energy balance terms, particularly during the sensitive time when snow begins melting, would benefit from analysis at sub-daily resolution. For example, sensible heat flux varies from positive to negative throughout the diurnal cycle, so taking a daily average may be a poor proxy for its role in the energy balance and its contribution to snow melt. Also, diurnal temperature range has some utility that goes beyond that of mean daily temperature when diagnosing changes near the surface during this time. It was calculated for some of the analysis in Chapters 2 and 3, and did provide additional insight into regional differences in MOD.

With a better understanding of how the MOD over land is changing regionally and how the melt drivers vary regionally and inter-annually, a few things can be done to move further. First, snow cover loss influences the energy balance and even the larger scale atmospheric circulation (e.g. Ellis and Leathers 1999). For example, Aizen et al. (2000) provided estimates of the amount of heat used to melt snow during the melt season, and the volume of air cooled an arbitrary level (5º C) as a result of this process. Given that changes in MOD and disappearance are occurring in some places faster than others, the timing of this energy uptake at the surface is then changing spatially as well. Potentially, this could lead to atmospheric perturbations on the scale of those identified by Cohen and Entekhabi (1999), where autumn Eurasian snow cover anomalies strengthen the Siberian High and propagate into the stratosphere, thereafter impacting Northern Hemisphere circulation via the Arctic Oscillation (Cohen et al. 2014). There may be a similar mechanism in the spring that develops in the future as differential changes in the system continue to evolve. Currently, this type of linkage exists, for

example, between winter and spring snow depth and melt with the timing and strength of the Indian monsoon (Dey and Kumar 1982; Vernekar et al. 1995; Zhang et al. 2004).

In addition, spring snow cover is changing concurrently with other components of the atmospheric, hydrologic, and ecological system at high latitudes. It would be interesting to integrate this improved knowledge of spring MOD into broader climate research to predict how all of these changes may affect one another. For example, if more than half of Arctic vegetation shifts to a different physiognomic class by 2050 simply due to changes in temperature and precipitation (Pearson et al. 2013), this will potentially have profound influences on spring snow depth and disappearance (with likely a more minor influence on MOD). Increasing shrub cover has been shown to inhibit snow redistribution and delays snow disappearance (Sturm et al. 2001). Therefore, incorporating a more regional understanding of MOD trends into an interdisciplinary study of future Arctic system changes could benefit both future projections of snow cover in all seasons as well as the evolution of the entire Arctic environment as it continues to warm.

Finally, attribution studies are well suited to sensitivity studies with climate models. Whereas point-scale studies of the energy balance around MOD have been done, the same study done along with perturbed energy balance inputs in a sensitivity study have not been done to the author's knowledge and would provide considerably more insight into this type of research question. A study of this nature had been previously planned but is still recommended for future work, and seeks to answer the question: How does the melt onset date vary at a given location with variations in atmospheric forcings? The methodology is outlined below.

5.4 Snow MOD Sensitivity Study

A sensitivity study of snow melt using an energy balance approach ideally requires a hydrologic model developed specifically for snow thermodynamics, and a single column atmospheric model (SCM) to allow for the atmospheric column to reach equilibrium after perturbed inputs provide a forcing for the surface. Hourly data supplied by the SCM forcings (typically standard reanalysis output) is run through the SCM at each of its time steps after the model source code is adjusted. These adjustments are what provide the range of conditions to which the surface energy balance is subjected.

The most appropriate perturbations to be coded into the SCM include modifications to water vapor (specific humidity) throughout the column, advective energy, and insolation. A change in specific humidity would primarily affect downwelling longwave radiation, and therefore would influence the surface most directly through this radiative change. Changes in advective energy are part of the model dynamical core that is forced at the grid boundaries at every time step, and are computed as increased or decreased flux convergence at each sigma level. This affects diabatic heating of the surface. Finally, changes in insolation are easily made using a run-time parameter to artificially adjust the latitude. This simulates the change in initial date by a given number of days to isolate the effect of insolation. All of these variables would be perturbed an equal amount on either side of zero to develop a simple, linear statistical model predicting the change in MOD based on variation in these variables. For example, the change in MOD resulting from a 10% increase or decrease in specific humidity should allow for a linear response that can be predicted across a range of input values.

SnowModel, a spatially distributed snow-evolution model (Liston and Elder

2006), is well suited to this type of study. Surface meteorological variables, including temperature, relative humidity, precipitation, incoming longwave and shortwave radiation, wind direction, and wind speed are then input into SnowModel, which models the snowpack and any melt processes that occur within it. Relevant output from SnowModel includes energy balance terms, snow melt energy, and runoff. The time series of the latter variables can be used to derive a melt onset date, thus allowing for a simplified metric by which to test sensitivity to initial perturbations.

Ideally this model is run on a grid space containing a suitable weather station, though meteorological stations in the Arctic that measure both shortwave and longwave fluxes are extremely sparse. The control run output of both SnowModel and especially the SCM can be compared to station observations for validation. This provides an excellent way to choose a study location, since little else in a location choice matters. The only other considerations have to do with the model grid: the landcover and topography should be relatively homogeneous with little or no water or coastline within the grid cell.

5.5 Extension of GrIS Surface Melt and Sea Ice Research

Future work pertaining to melt onset dates on sea ice and Greenland and the linkages between sea ice, GrIS surface melt, and the atmosphere should be planned with the understanding that this has been a popular topic in the last few years and there is current research underway to address some of these questions. Unsurprisingly, this has been approached in many different ways from modeling studies (Porter et al. 2012; Day et al. 2013; Koenig et al. 2014) to sensitivity studies (e.g. Noël et al. 2014), statistical analysis using surface observations (Hanna et al. 2013), synoptic analysis (Hanna et al.

2014), and some of the same methodology as employed in Chapter 4 such as SOM analysis (Higgins and Cassano 2009; Schuenemann et al. 2009).

My proposed future work on this topic is a continuation and expansion of Chapter 4 to the GrIS surface mass balance in all seasons. This would use much of the same analysis initially, but expanded beyond the summer season and expanded to some additional surface and atmospheric variables such as precipitation, radiative fluxes, and energy flux convergence (i.e. mapping some of these onto newly produced SOM nodes) to obtain a better understanding of the energy balance associated with different nodes. Further analysis with SOMs will identify preferred circulation patterns in high and low accumulation and melt years based on seasonal SOM nodes. Finally, given the relatively long time period of record, trends and variability in each SOM node, including the fields which are mapped onto them, can be readily obtained using basic outputs of the SOM analysis as shown in Chapter 4.

Similar to snow melt onset, climate models are one of the more useful tools to address this type of research question, specifically a sensitivity analysis, which can simulate the range of atmospheric conditions that have a direct role in GrIS surface melt. As discussed, modeling studies have been undertaken on this subject in many forms, but here a sensitivity study is proposed that would use a regional model to simulate different spring and summer scenarios over the ice sheet. This sensitivity study would simulate different sea ice concentrations in adjacent waters and also varying ice sheet albedo at the beginning of the melt season, with diagnostic output given as the change in surface melt in the following weeks.

After it is better understood to what extent sea ice loss is responsible for

anomalous energy fluxes over Greenland and environs, it will be possible to explore the influence of these fluxes on both precipitation and summer surface melt. The most appropriate method here is SVD to assess the covariance among anomalous energy fluxes and precipitation and surface melt. This will not only determine the strength of this relationship over various time periods and time lags, but it will spatially isolate those parts of the GrIS where the response is strongest. Given that there is a delay in the response of the energy balance over Greenland to anomalous fluxes at the atmosphere-ocean interface, different time lags will be tested in the SVD to determine when the covariance is strongest. This is an extension of some of the SVD analysis in Chapter 4 to more variables and as well as testing time lags.

The final component of this extension of Chapter 4 will incorporate albedo into a study of Greenland melt onset, as there is a relatively strong correlation between melt onset, albedo, and subsequent melt on the ice sheet. The relationship between these variables is important because of the potentially strong albedo feedback that operates over this time period and the possibility of persistence in the atmospheric circulation patterns that initiate melt onset to then generate anomalously high or low levels of surface melt in the summer. This is further confounded by any snowfall events, particularly shortly after the MOD, that raise the albedo as it is decreasing to its darker summer regime.

To explore the connection between these snowfall events and the synoptic patterns that generate them, these events will be identified and tabulated based on daily Moderate Resolution Imaging Spectroradiometer (MODIS) data from 2003 to present and mapped onto the SOM nodes generated in the previous analysis. Next, the effect of this

change in albedo will be determined through an analysis of surface energy balance terms in the following two weeks, and compared with the remainder of the summer when these events do not occur. By mapping each of these time periods onto the corresponding SOM nodes of the dominant synoptic pattern during each period, the results of this comparison can be assessed while qualitatively (visual assessment on the master SOM maps) controlling for the synoptic pattern. Finally, the occurrence of melt events in the two weeks following snowfall will be tabulated and evaluated in a similar manner as the energy balance, given the close connection between the two.

Both the terrestrial snow melt sensitivity study and the project seeking to further understand sea ice and GrIS mass balance linkage should represent an advancement in these two areas of cryospheric changes. The latter study is particularly well suited as an initial building block for further work, given the large scope and more exploratory nature of analysis that can identify previously unseen relationships among large datasets. Further insight into both of these questions is an increasingly necessary step toward predicting the future climate system as many of the Northern Hemisphere's cryospheric components continue to experience accelerated change.

References

Aizen, E. M., V. B. Aizen, J. M. Melack, and A. N. Krenke, 2000: Heat exchange during snow ablation in plains and mountains of Eurasia. *J. Geophys. Res.*, **105**, 27,013–27,022.

Cohen, J., J. C. Furtado, J. Jones, M. Barlow, D. Whittleston, and D. Entekhabi, 2014: Linking Siberian Snow Cover to Precursors of Stratospheric Variability. *J. Clim.*, **27**, 5422–5432, doi:10.1175/JCLI-D-13-00779.1.

Cohen, J., J. C. Furtado, J. Jones, M. Barlow, D. Whittleston, and D. Entekhabi, 2014: Linking Siberian Snow Cover to Precursors of Stratospheric Variability. *J. Clim.*, **27**, 5422–5432, doi:10.1175/JCLI-D-13-00779.1.

Day, J. J., J. L. Bamber, and P. J. Valdes, 2013: The Greenland Ice Sheet's surface mass balance in a seasonally sea ice-free Arctic. *J. Geophys. Res. Earth Surf.*, **118**, 1533–1544, doi:10.1002/jgrf.20112.

Dey, B., and O. B. Kumar, 1982: An apparent relationship between Eurasian spring snow cover and the advance period of the Indian summer monsoon. *J. Appl. Meteorol.*, **21**, 1929–1932.

Ellis, A. W., and D. J. Leathers, 1999: Analysis of Cold Airmass Temperature Modification across the U.S. Great Plains as a Consequence of Snow Depth and Albedo. *J. Appl. Meteorol.*, **38**, 696–711, doi:10.1175/1520-0450.

Hanna, E., J. M. Jones, J. Cappelen, S. H. Mernild, L. Wood, K. Steffen, and P. Huybrechts, 2013: The influence of North Atlantic atmospheric and oceanic forcing effects on 1900-2010 Greenland summer climate and ice melt/runoff. *Int. J. Climatol.*, **33**, 862–880, doi:10.1002/joc.3475.

——, and Coauthors, 2014: Atmospheric and oceanic climate forcing of the exceptional Greenland ice sheet surface melt in summer 2012. *Int. J. Climatol.*, **34**, 1022–1037, doi:10.1002/joc.3743.

Higgins, M. E., and J. J. Cassano, 2009: Impacts of reduced sea ice on winter Arctic atmospheric circulation, precipitation, and temperature. *J. Geophys. Res.*, **114**, D16107, doi:10.1029/2009JD011884.

Koenig, S. J., R. M. Deconto, and D. Pollard, 2014: Impact of reduced Arctic sea ice on Greenland ice sheet. *Geophys. Res. Lett.*, **41**, 3934–3943, doi:10.1002/2014GL059770.A.

Noël, B., X. Fettweis, W. J. van de Berg, M. R. van den Broeke, and M. Erpicum, 2014: Small impact of surrounding oceanic conditions on 2007–2012 Greenland Ice Sheet surface mass balance. *Cryosph.*, **8**, 1453–1477, doi:10.5194/tcd-8-1453-2014.

Pearson, R. G., S. J. Phillips, M. M. Loranty, P. S. a. Beck, T. Damoulas, S. J. Knight, and S. J. Goetz, 2013: Shifts in Arctic vegetation and associated feedbacks under

climate change. *Nat. Clim. Chang.*, **3**, 673–677, doi:10.1038/nclimate1858.

Porter, D. F., J. J. Cassano, and M. C. Serreze, 2012: Local and large-scale atmospheric responses to reduced Arctic sea ice and ocean warming in the WRF model. *J. Geophys. Res.*, **117**, 1–21, doi:10.1029/2011JD016969.

Schuenemann, K. C., J. J. Cassano, and J. Finnis, 2009: Synoptic Forcing of Precipitation over Greenland: Climatology for 1961–99. *J. Hydrometeorol.*, **10**, 60–78, doi:10.1175/2008JHM1014.1.

Sturm, M., J. P. McFadden, G. E. Liston, F. S. Chapin III, C. H. Racine, and J. Holmgren, 2001: Snow – Shrub Interactions in Arctic Tundra : A Hypothesis with Climatic Implications. *J. Clim.*, **14**, 336–344.

Vernekar, A., J. Zhou, and J. Shukla, 1995: The effect of Eurasian snow cover on the Indian monsoon. *J. Clim.*, **8**, 248.

Zhang, Y., T. Li, and B. Wang, 2004: Decadal change of the spring snow depth over the Tibetan Plateau: the associated circulation and influence on the east Asian summer monsoon*. *J. Clim.*, **17**, 2780–2793.

Acknowledgement of Prior Publications

Some parts of this dissertation were previously published by the American Meteorological Society (AMS) in the Journal of Climate under the title “Controls on Spatial and Temporal Variability in Northern Hemisphere Terrestrial Snow Melt Timing, 1979–2012” and the American Geophysical Union in the Journal of Geophysical Research – Atmospheres under the title “Attribution of snowmelt onset in Northern Canada”. The majority of the writing in these paper is my own, done with helpful advice from coauthors and reviewers. The AMS and the AGU hold the copyright to that work.